SIMULATION OF THE DEFORMATION OF NON-NEWTONIAN DROPS IN A VISCOUS FLOW

PROEFSCHRIFT

ter verkrijging van
de graad van doctor aan de Universiteit Twente,
op gezag van de rector magnificus,
prof. dr. F.A. van Vught,
volgens besluit van het College voor Promoties
in het openbaar te verdedigen
op vrijdag 31 oktober 1997 te 15.00 uur

door

Edgar Matthijs Toose

geboren op 24 april 1969
te Rotterdam

Dit proefschrift is goedgekeurd door
de promotoren

prof. dr. J. Mellema
en
prof. dr. ir. P.J. Zandbergen

en de assistent-promotor

dr. H.T.M. van den Ende

to *Ae Ran*

Toose, Edgar Matthijs

Simulation of the deformation of non-Newtonian drops in a viscous flow
Thesis Universiteit Twente, Enschede.
- With ref. - With summary in Dutch.
ISBN 9036510376

The work described in this thesis is part of the research program of the J.M. Burgerscentre.

Contents

Chapter 1

Introduction

Rheology, the description of the deformation and flow of materials in relation to the applied stress, is one of the broadest subjects in fluid dynamics. Processing of food, cosmetics, domestic products, coatings and lubricants are some examples of processes where the rheology of materials plays an important role. (Sherman [1]). Moreover, the understanding of several biological processes relies on a proper description of the rheological properties, e.g. flow of blood through small vessels. Materials of interest to rheology are complex fluids, including fluids that are composed of complex molecules, fluids that consist of several components, and the combination of both. Dispersions form an important class of the latter type of complex fluids and as such they have been the subject of intensive and worldwide study (Barnes [2]). A dispersion is a fluid consisting of particles which are more or less uniformly suspended in a suspending liquid. The rheological behavior of a dispersion is influenced by many factors related to the type of particles (e.g. solid or deformable) and the forces between these particles (Brenner [3] and Russel et al. [4]).

The central theme of this thesis is the prediction of the rheological behavior of a dispersion containing deformable particles, such as gas bubbles, liquid drops and biological cells. Because the deformability of these particles strongly influences the rheological properties of the material it composes, much emphasis has been put on the observation, description and understanding of the deformation processes of deformable drops (see e.g. Rallison [5] and Stone [6] for a survey). Several approaches to the study of dispersions of deformable particles are possible: physical experiment, analytical theory, and numerical simulation. The first steps towards understanding the deformation processes of deformable drops were made by Rayleigh [7] who more than a century ago studied the breakup of a fluid jet. In the mid thirties, Taylor [8, 9] studied

the deformation of a single drop under the influence of a well defined external flow field, both analytically and experimentally. The basic principles of Taylor's analytical work were later refined (Cox [10] and Barthès-Biesel [11]) and extended to viscous drops surrounded by a viscoelastic shell (Brunn [12]) and double concentric viscous drops (Stone and Leal [13]). However, the inability to fully include particle-particle interactions severely restricts the analytical approach. To study a single drop in an elongational or shear flow experimentally, Taylor devised two instruments: a parallel band and a four roller apparatus (see figure 1-1). Today the deformation of single particles is studied

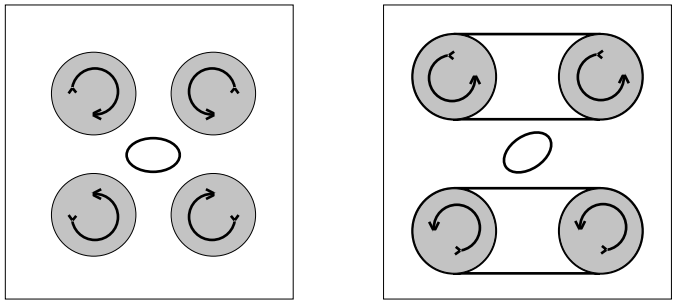

Figure 1-1: Four roller and parallel band apparatus as designed by Taylor

experimentally using devices similar to, but more sophisticated than Taylor's. A counter rotating Couette device designed by De Haas [14] and a computer-controlled four-roll mill designed by Bentley [15]. By distorting a dispersion in such devices and quenching it at a certain time, one essentially freezes the current state of the material, and this gives the opportunity to directly investigate the deformation of the drops with a microscope at different stages of the flow (Delaby et al. [16], Gramespacher and Meissner [17]). In some devices (Gramespacher and Meissner [17]) it is possible to measure bulk properties of a dispersion, such as viscosity and normal stresses during the distortion process. With these studies, it is possible to relate the morphology and rheology of a dispersion to some degree.

The numerical approach, which is the topic of this thesis, is complementary to the theoretical and experimental approaches. With this approach, the simultaneous investigation of the deformation processes and the bulk properties is possible. However, the uncertainty in the quality of the constitutive equations describing the dynamics of the fluids inside and outside the drop, and the sometimes crude modelling of the evolution of the interfaces between them restricts our ability to simulate realistic dispersions of deformable par-

ticles. Moreover, in view of the still rather limited capability of computers, a restriction to relatively simple flows, e.g. to 2D or axisymmetric flows, is presently required. However, in view of the rapid increase of computer power in recent years, it is expected that numerical simulations will develop towards more realistic applications in the near future.

The deformability of a particle depends, in a complicated manner, on the properties of the inner and outer fluid, and the mechanical properties of the interface between the particle and the suspending fluid. A study on dispersions of deformable particles can be split into three problems. The first problem is the determination of a set of constitutive equations describing the hydrodynamical and mechanical behavior of the fluids and interfaces respectively. Secondly, the hydrodynamic problem of the motion and deformation of a single particle in an external flow has to be solved. The solution to this problem yields an approximation of the rheological behavior of sufficiently dilute dispersions. Finally, interactions between different particles have to be included in the hydrodynamic problem in order to describe the rheological behavior of more concentrated dispersions. The main purpose of this thesis is the development and application of numerical methods to tackle the second and, in part, also the third problem mentioned above.

The first section of this chapter gives an overview of the approaches and basic steps in the numerical simulation of dispersions of deformable particles. In section 1.2 the general setting of the problem of a dispersion of deformable particles is discussed. After this introduction, we formulate the basic aims and give an outline of the thesis in section 1.3.

1.1 Numerical simulation of dispersions

The starting point for the numerical simulation of a general fluid flow problem are the Navier-Stokes equations, which represent the conservation of mass, momentum and energy. With the Navier-Stokes equations one can describe orderly laminar flows as well as complex turbulent flows. In a turbulent flow there exists a hierarchy of eddies from small to large scales, in which large eddies transfer energy to smaller eddies, whereas the smallest eddies are dissipated due to the viscosity. The amount of relevant scales in a turbulent flow increases with the Reynolds number which is defined as (Reynolds [18]):

$$Re = \frac{\rho_R u_R L_R}{\eta_R},$$

where ρ_R, u_R, L_R and η_R represent a reference density, velocity, length and viscosity respectively. This number can be interpreted as the ratio between the inertial and viscous forces. If the Reynolds number is high the viscous forces are small compared to the inertial forces, leading to a large amount of relevant spatial and temporal scales. Direct Numerical Simulation of high-Reynolds-number flow hence requires massive computational power as all the relevant scales must be captured (see e.g. Rogallo and Moin [19] and Kleiser and Zang [20]). Conversely, if the Reynolds number is very small, viscous effects dominate and a smooth, ordered flow results that can accurately be resolved with present-day computers.

In case of a dispersion of deformable particles, one can distinguish between a macroscopic and a microscopic scale. The macroscopic length scale corresponds to the geometry of the flow problem, whereas the microscopic length is in the order of the particle size. A typical example found in industry is a stirring vessel where the macroscopic length scale is related to the stirring blades, which are of the order of decimeters, and the particle size is of the order of micrometers. Due to the tremendous ratio between these two length scales an equally large ratio of the relevant Reynolds numbers arises, which implies that the flow on the large scale may already be turbulent whereas the microscopic flow problem may still be dominated by viscosity and hence be laminar. Thus, typically, direct simulation of the complete flow problem is virtually impossible with today's computational power. To deal with this problem, we may first consider the problem at the microscopic scale, i.e. the simulation of single particle or a few interacting particles. By assuming that the flow at the particle size is governed by viscous stresses, i.e. the smallest turbulent length scale is larger than the particle size, the microscopic flow problem can be resolved with present-day computers.

It should be noted that there are also situations where the whirls in the flow are of the same size as the particles, implying that we deal with a convectively dominated flow. This falls outside the scope of the approach adopted in this thesis, and a direct numerical simulation might be required in these cases (Sheth and Pozrikidis [21]). With single-particle simulations at low Reynolds numbers, it is possible to study properties of the particles such as the deformation process and breakup. Simulations of multiple interacting particles enable us to find an approximate viscosity and normal stress by averaging over all the relevant particles. Based on these results a model describing the macroscopic rheological behavior of the dispersion can be formulated. This may subsequently be used in a simulation of the macroscopic flow problem. In this thesis, we are mainly concerned with the numerical simulations of single

and multiple interacting deformable particles.

The reference length in the numerical simulations is on the order of the particle size, which can range from several tens of nanometers to about one hundred micrometers in a typical application. A red blood cell for example has an average diameter of about eight micrometers. Assuming that the flow at particle scale is smooth, we can write the reference velocity as a typical velocity gradient G_R times the reference length (i.e. $u_R = G_R L_R$). Taking the density and viscosity equal to that of water, and G_R equal to $10s^{-1}$, we find a Reynolds number ranging between 10^{-9} and 10^{-1} for a particle of size between $10nm$ and $100\mu m$ respectively. These examples correspond to typical circumstances addressed in this thesis for which it is appropriate to assume that the Reynolds number based on particle scale is sufficiently small. Together with the assumption that the fluids involved in the flow problem are incompressible, we can describe the hydrodynamics with the equations for Stokes flow. For some specific flow problems, it is possible to find analytic solutions to these equations (Lamb [22]). The solution of the flow equations in terms of spherical harmonics, was used by Taylor [8] to derive an approximate expression for the deformation of a single viscous drop placed in this flow field. Besides the shape of the drop, Taylor also obtained an approximate expression for the viscosity of a dilute suspension of drops.

Although Direct Numerical Simulation of a drop at low Reynolds number is possible, there is still a large amount of computational power needed if one uses conventional methods such as finite differences (Sheth and Pozrikidis [21]). An additional problem is the deformation of the flexible surface of the drop, which is hard to capture with these methods. A more appropriate method arises from the reformulation of the Stokes equations in terms of boundary integral expressions, and the subsequent numerical solution of the integral equations. The numerical approach to solve the integral equations is usually called the Boundary Element Method (BEM). The mathematical basis for this approach can be found in the pioneering work of H.A. Lorentz [23]. The diversity of the many subsequent developments which, to some extent, can be seen as originating from this work, would probably have surprised Lorentz whose interest in applied physics took more definite forms only late in his life in relation to the construction of the 'Zuiderzeewerken' [24].

The deformation of neutrally-buoyant Newtonian drops in viscous extensional flows at low Reynolds number was first studied numerically by Youngren [25] who used a boundary element method. Due to the reformulation of the problem in terms of boundary integrals the BEM is particularly suited for free surface problems. Another advantage of the method is the reduction of the

dimension of the computational problem for Newtonian fluids, which significantly reduces the computational cost. The BEM has extensively been used by others in order to simulate the behavior of viscous drops in simple flow fields. Recent studies have tackled more complicated flow problems (e.g. breakup of drops, Tjahjadi [26]) and incorporated additional physical phenonema (e.g. the effects due to surfactants, Stone [27] and Li and Pozrikidis [28] and the elasticity of the membrane, Li [29]). Recently the boundary-element method was used to simulate concentrated dispersions of viscous drops in shear flow (Li et al. [30] and Loewenberg and Hinch [31]) and double concentric viscous drops (Stone and Leal [13]).

In many applications, the drop consists of a non-Newtonian fluid. Examples include polymer blends, (polymer drops suspended in a highly viscous (polymeric) fluid), suspensions of vesicles and biological fluids such as blood. The development of the boundary integral method in these cases is much more complicated due to the domain integral which arises from the non-Newtonian contributions. Bush [32, 33] was the first to adopt the boundary element method to analyze extrusion experiments with non-Newtonian fluids. In this thesis, the boundary integral approach is extended to dispersions of non-Newtonian drops immersed in a Newtonian fluid.

The incorporation of non-Newtonian fluids in the description requires the introduction of a grid covering the layers of the drop containing non-Newtonian fluids, next to the definition of discrete points on the interfaces, and adds considerably to the numerical cost of simulations of non-Newtonian drops and vesicles. However, compared to a more direct (finite difference) discretization of the Stokes equations, which would also require a grid covering the much larger Newtonian region exterior to the drop, the boundary integral method has a number of important advantages. The incompressibility of the fluids is fully incorporated into the expression for the velocity field and does not require some sort of 'pressure-correction' as occurs in many direct numerical methods for simulating unsteady incompressible flows. The boundary integral method is more flexible and accurate with respect to modelling the boundary geometries and boundary conditions. In particular, the conditions on the solution at infinity are implicitly taken care of in the boundary integral method whereas a suitable, but approximate condition at a finite distance needs to be introduced in a finite-difference or finite-element method. Moreover, in several applications the region containing a non-Newtonian fluid forms only a small portion of the flow-problem, e.g. a vesicle in which the Newtonian drop is encapsulated by a thin non-Newtonian lipid bilayer, and the boundary integral method can be used effectively.

1.2 Modelling of drops and vesicles

As mentioned in the previous section, a deformable particle can consist of a simple Newtonian fluid, but also of a complex non-Newtonian fluid. The mechanical properties of this non-Newtonian fluid can be described by a certain rheological model (see Bird et al. [34] for an overview of different models). The choice of a particular model depends on the non-Newtonian fluid involved. In the case of a polymer blend for example, we may model the polymer solution inside the drop as a so-called Oldroyd-B fluid. Besides the mechanical properties of the internal fluid, we also have to take into account the mechanical properties of the interface between a deformable particle and the suspending fluid. We discuss this important subject in this section.

The interface between a deformable particle and the suspending fluid can be a gas-fluid or fluid-fluid interface (e.g. capsules or liquid drops) or a membrane with complex mechanical properties (e.g. vesicles or red blood cells). An important model system belonging to the latter category is formed by so-called lipid-bilayer-vesicles. A lipid-bilayer-vesicle is a liquid drop, which is enclosed by one or more lipid bilayers (see figure 1-2). The lipids in the bilayer of a vesicle are amphiphilic molecules with an apolar tail, which consists of one or two hydrocarbon chains and a polar head (De Haas [14]). Due to the apolar tail, these lipids are insoluble in water. In contact with water, several aggregate forms are possible, with the lipid bilayer being one of the stable forms: the lipid tails are grouped together, and the lipid heads are in contact with water (see figure 1-2). The bilayer thickness is about 5 nm. The vesicle is called uni-lamellar when the interface between inner fluid and suspending fluid consists of one such bilayer, and multi-lamellar when it consists of more than one bilayer. The size of a lipid bilayer vesicle can range from ten nanometers

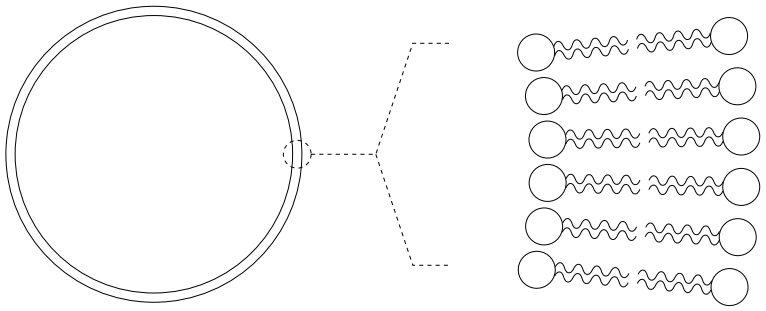

Figure 1-2: Schematic representation of a uni-lamellar lipid bilayer vesicle

up to about one hundred micrometers. As such, these vesicles are expected to share several properties with biological cells and play a role in technological applications.

The mechanical properties of the interface between an immiscible liquid drop and the suspending fluid is described, within good approximation, by Laplace's law (see e.g. Scriven [35] and Barthès-Biesel [36] for an overview). This law states that a certain constant interfacial tension σ acts along the interface resisting deformation due to external forces. In particular, this tension results in spherical drops if external forces are absent. In many practical situations, however, the interface between an immiscible liquid drop and the suspending fluid is covered with a surfactant. The presence of this surfactant leads to variations in the interfacial tension and/or interfacial viscosity and elasticity, which have a considerable effect on the dynamic behavior of the liquid drops (Levich and Krylov [37]). In this work, we focus on constant interfacial tension, although variations in the interfacial tension can be introduced in the method (see also Stone and Leal [27] or Li and Pozrikidis [28]).

In general the modelling of the mechanical properties of the membrane of a vesicle or red blood cell is done by regarding the lipid bilayer as an infinitely thin (visco-)elastic sheet (Barthès-Biesel [36]). By considering sufficiently small deformations, the stress in the plane of the membrane can be related to the shear and extensional deformations (Landau and Lifshitz [38]). Using the relation between the stress and the deformation of the membrane, the deformation of a liquid drop enclosed by an elastic membrane due to an external flow field can be calculated analytically (Barthès-Biesel and Rallison [39]) or numerically (Li et al. [29] and Pozrikidis [40]). The bending of the membrane can be incorporated by relating the stored bending energy to the local curvature of the membrane relative to an spontaneous curvature. This latter curvature was introduced by Helfrich [41] in order to be able to incorporate asymmetries in the membrane.

A disadvantage of this approach, i.e. considering the lipid bilayer as an infinitely thin elastic sheet, is that the stress distribution within the lipid bilayer cannot be studied. Knowledge of this stress distribution is in particular useful if one wants to predict the breakup of a vesicle or red blood cell due to a critical stress level in the membrane (Lacell et al. [42]). As an alternative we follow an approach suggested by Brunn [12] to model a vesicle as a liquid drop enclosed by one (or more) thin layers all containing a certain non-Newtonian material thus enabling the study of the interface layer. The different layers are separated by simple fluid-fluid interfaces with a constant interfacial tension. In the remainder of the thesis, a drop consisting of one single layer or of

multiple layers of a (non-)Newtonian material is called, respectively, a simple or compound non-Newtonian drop.

1.3 Purpose and outline

In this section, we formulate our research aims more specifically and give a global overview of the contents of the following chapters. The primary aim of this thesis is the development of a boundary-integral method for the simulation of the deformation of a single non-Newtonian drop or vesicle in a slow viscous flow. The second aim is to study the influence of the non-Newtonian material inside the drop on the deformation processes. In order to test and illustrate the method, we selected a situation where an axisymmetrical non-Newtonian drop or vesicle is placed in an elongational flow. This situation has the benefit of incorporating all the effects of a fully three dimensional flow problem, whereas the numerical problem can be reduced to two dimensions. Finally our third aim is to incorporate particle-particle interactions in the method in order to extend the approach to a macroscopic dispersion of drops or vesicles.

Having formulated our research aims, we summarize the contents of this thesis. The problem description and governing equations are formulated in chapter 2. This chapter also includes a description of several macroscopic properties which are used to analyze the deformation process of single and multiple drops. In chapter 3, several rheological models are presented to describe the non-Newtonian character of the drops. The general boundary-integral formulation for non-Newtonian drops in a viscous flow is discussed in chapter 4. In chapter 5, we present the numerical methods used to simulate the deformation of a single drop in a three-dimensional elongational flow or of multiple drops in a two-dimensional shear flow. Results of the boundary integral method are presented in chapters 6 to 8. In chapters 6 and 7, simulation results for simple and compound non-Newtonian drops subjected to an elongational flow are presented. In order to test the method, an extensive numerical validation and physical verification is performed. In chapter 8 we consider the applicability of the method to a dispersion of multiple drops, and present simulation results for a dispersion of Newtonian drops. Finally, conclusions and recommendations for future research are presented in chapter 9.

Chapter 2

Governing equations

In section 2.1 we present the general setting of the problems considered. The basic equations governing Stokes flow are presented in section 2.2. Finally some configurational and rheological properties of single drops and dispersions are defined in section 2.3.

2.1 Problem description

In this section, we describe the basic problems of flow inside and around single axisymmetric compound non-Newtonian drops, and multiple viscous drops placed in an unbounded incompressible Newtonian fluid. The surrounding suspending fluid has a viscosity η and is subjected to a linear flow field which is described by:

$$u_1^\infty = G(\alpha x_1 + (1-\alpha)x_2), \quad u_2^\infty = -\frac{1}{2}G\alpha x_2, \quad u_3^\infty = -\frac{1}{2}G\alpha x_3, \qquad (2\text{-}1)$$

with u_j^∞ the $j-$th component of the velocity field in a Cartesian coordinate frame $\{\boldsymbol{e}_1, \boldsymbol{e}_2, \boldsymbol{e}_3\}$. The parameters G and α determine the magnitude and type of flow.

In this study we concentrate on two special flow types: elongational flow for single drops ($\alpha = 1$) and shear flow for multiple drops ($\alpha = 0$). For a single compound drop the axis of symmetry of the drop coincides with the axis of rotational symmetry of the elongational flow. All fluids are assumed to be incompressible and isotropic; buoyancy is considered to be absent, i.e. we assume that the densities of all fluids are equal. In the following two subsections we describe the two main applications in more detail.

2.1.1 Non-Newtonian compound drop

A compound drop consists of K concentric layers, each containing a certain generally non-Newtonian material. The volumes occupied by the unbounded Newtonian fluid outside the drop and by the different layers, counted from the outside to the inside, are denoted by $V^{(0)}$, and $V^{(1)}, V^{(2)}, \ldots, V^{(K)}$ (see figure 2-1). The interface $S^{(l)}$ between the domains $V^{(l-1)}$ and $V^{(l)}$, $l = 1, \ldots, K$ is subjected to a constant interfacial tension $\sigma^{(l)}$. The interface $S^{(1)}$ corresponds to the outer drop interface; for convenience, we let $S^{(0)}$ denote the surface corresponding to $\boldsymbol{x} \to \infty$. The initial configuration of the drop is taken to

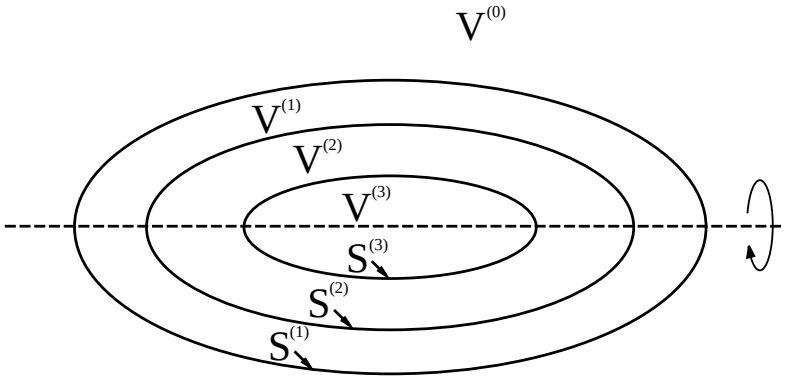

Figure 2-1: Schematic representation of a three-layer compound drop

be a set of concentric spheres with radii $R^{(l)}, l = 1, \ldots, K$. Throughout the analysis we will work with dimensionless variables: All lengths are scaled with the initial outer drop-radius $R^{(1)} = a$, velocities by aG, and viscosities by η (Li et al. [29]). In changing to dimensionless variables it is natural to introduce the following dimensionless parameters:

$$C^{(l)} = \frac{\eta G a}{\sigma^{(l)}} \text{ and } \lambda^{(l)} = \frac{\eta^{(l)}}{\eta} \text{ and } \kappa^{(l)} = \frac{R^{(l)} - R^{(l+1)}}{a} \; ; \quad l = 1, \ldots, K, \tag{2-2}$$

which play an important role in the dynamics of the deformation. Here $C^{(l)}$ is the capillary number of the l-th interface, which is a measure of the ratio between the viscous stresses and interfacial tension. The parameter $\lambda^{(l)}$ is the ratio between the viscosity $\eta^{(l)}$ in the l-th domain and the exterior viscosity η

(in particular $\lambda^{(0)} = 1$). Moreover, it is convenient to introduce:

$$\kappa^{(l)} = \frac{R^{(l)} - R^{(l+1)}}{a}, \tag{2-3}$$

where $\kappa^{(l)}$ denotes the ratio of the thickness of the undeformed spherical layer $V^{(l)}$ and the outer radius of the drop, where for convenience we introduced $R^{(K+1)} = 0$.

2.1.2 Two-dimensional dispersion

A mono-disperse dispersion of two-dimensional (non-)Newtonian drops, suspended into an incompressible Newtonian fluid with viscosity η forms the second main application of this thesis. The dispersion of drops is subjected to a linear shear flow as described by equation (2-1). Inertia forces on the drops are assumed to be negligible and buoyancy is absent. The initial configuration of the dispersion consists of a finite number of randomly placed drops with outer radii a. The volume fraction ϕ of the dispersed phase is given by $\phi = n\pi a^2$, with n the number of drops per unit volume (i.e. area in two dimensions). The left-hand side of figure 2-2 shows an example of a small part of the initial configuration of a dispersion. The domains occupied by the

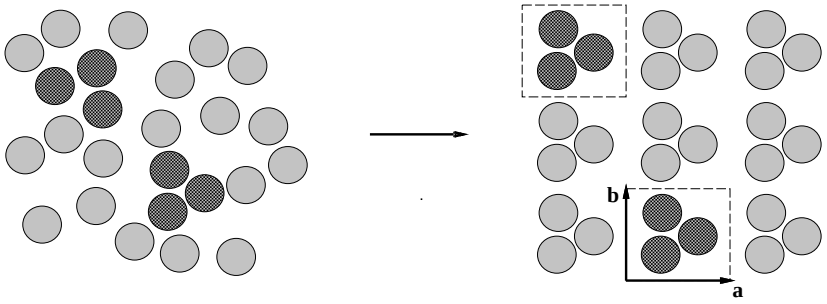

Figure 2-2: Schematic representation of a dispersion and its periodic counterpart.

suspending Newtonian fluid and dispersed drops are denoted by $V^{(0)}$ and $V_k^{(1)}$ respectively where k counts all drops. The interface $S_k^{(1)}$ between the domains $V^{(0)}$ and $V_k^{(1)}$, $k = 1, \ldots, N$, exhibits a constant interfacial tension $\sigma_k^{(1)}$.

As discussed in the introduction of this thesis, a real dispersion of drops contains a very large number of drops per unit volume. Direct simulation of such a system is presently impossible due to the immense amount of computational time needed. To circumvent this problem, we model a dispersion as periodic: instead of taking one box filled with millions of randomly placed drops, we consider a finite number of drops in a smaller domain and copy this cluster in the direction of the lattice vectors defining the periodicity of the system (Brady [43]). In this way, we can both model the macroscopic domain of a real dispersion and take into account all drop interactions, all within a reasonable amount of computational time. To illustrate the concept of periodicity, we took a cluster of three drops, and copied it in two directions as shown in the right hand side of figure 2-2. This figure also shows that the geometry of the periodic suspension is defined by two base vectors, $\boldsymbol{a}$ and $\boldsymbol{b}$, which evolve under a shear flow $\boldsymbol{u}^{\infty}$ according to:

$$\boldsymbol{a}(t) = \boldsymbol{a}(0); \quad \boldsymbol{b}(t) = \boldsymbol{b}(0) + b_2(0)\, t\, \boldsymbol{e}_1, \tag{2-4}$$

where t denotes the dimensionless time. It is noted that the vector $\boldsymbol{a}$ remains constant in time, whereas $\boldsymbol{b}$ gets more and more tilted as shown in figure 2-3. However, when the time has evolved up to $t = a_1(0)/b_2(0)$, the x_1 components

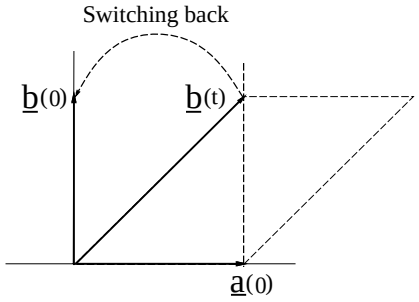

Figure 2-3: Schematic representation lattice vectors $\boldsymbol{a}$ and $\boldsymbol{b}$ and the switching back of the vector $\boldsymbol{b}$.

of $\boldsymbol{a}(t)$ and $\boldsymbol{b}(t)$ have the same magnitude. At that time the periodicity of the system is described by the original vectors $\boldsymbol{a}(0)$ and $\boldsymbol{b}(0)$ (Li and Pozrikidis [30] and Loewenberg and Hinch [31]). This property of the periodicity of the system is used to switch the vector $\boldsymbol{b}(t)$ back to its original form whenever this condition holds (see also figure 2-3).

It should be noted that the periodic dispersion considered, only consists of a finite number of drops. This implies that the periodic dispersion is only an approximation of a real dispersion which would contain an unlimited number of drops. The effect of this approximation can be investigated by increasing the number of drops in the periodic box while keeping the volume fraction constant. However, as the dynamics of the drops is mostly governed by close range hydrodynamic interactions between the drops, it is expected that only a limited number of drops will be needed in order to yield reliable results (Brady [43]). This issue will reappear in chapter 8.

2.2 The Stokes flow equations

The flow in and around a (compound) non-Newtonian drop introduced in the previous section is governed by the Stokes equations since the Reynolds number $Re = (\rho a^2 G)/\eta$ (with ρ the density) at the length scale of the drop is sufficiently small (Pozrikidis [44]). In particular, the basic equations read:

$$\partial_j u_j = 0 \; ; \quad \partial_j \pi_{ij} = 0 \tag{2-5}$$

with π_{ij} the total stress tensor and $\partial_j = \partial/\partial x_j$. In equation (2-5), as in the rest of this thesis, the Einstein summation convention is adopted which implies summation over repeated indices. The Stokes flow equations given above are further supplemented with suitable matching conditions at the interfaces $S^{(l)}$ and asymptotic conditions as $|\boldsymbol{x}| \to \infty$. As the different layers of the drop can consist of different types of non-Newtonian material, we distinguish between a set of local stress tensors $\pi_{ij}^{(l)}, l = 1, \ldots, K$, corresponding to the total stress tensor in the domain $V^{(l)}$, i.e. $\pi_{ij}^{(l)} = \pi_{ij}$ if $\boldsymbol{x} \in V^{(l)}$. The superscript (l) will also be used to indicate the domain of definition for other flow quantities.

In the domain $V^{(l)}$, the total stress tensor π_{ij} is decomposed as:

$$\pi_{ij}^{(l)} = \tau_{ij}^{(l)} + \tilde{\tau}_{ij}^{(l)} = -\delta_{ij} P^{(l)} + \lambda^{(l)} \dot{\gamma}_{ij}^{(l)} + \tilde{\tau}_{ij}^{(l)} \; , \quad i, j = 1, \ldots, 3, \tag{2-6}$$

where $P^{(l)}$ is the isotropic pressure field, δ_{ij} the Kronecker tensor, $\tau_{ij}^{(l)}$ the Newtonian part of the total stress tensor, and $\dot{\gamma}_{ij}^{(l)}$ is twice the rate-of-strain tensor:

$$\dot{\gamma}_{ij}^{(l)} = \partial_i u_j^{(l)} + \partial_j u_i^{(l)}.$$

The non-Newtonian part of the total stress tensor $\tilde{\tau}_{ij}^{(l)}$ in (2-6) obeys a certain constitutive equation which describes the specific rheological character

of the fluid. As an example, and to illustrate the basic approach, we focus on one of the non-Newtonian models considered in this thesis: the Oldroyd-B model. This model finds its origin in polymer rheology and contains, besides solvent viscosity $\lambda^{(l)}\eta$, two parameters: a relaxation time $t_p^{(l)}$ and the polymer contribution to the zero-shear-rate viscosity $\eta_p^{(l)}$ (Bird [34]). The constitutive equation for this model is given by:

$$De^{(l)}\mathcal{D}_t\tilde{\tau}_{ij}^{(l)} + \tilde{\tau}_{ij}^{(l)} = \lambda_p^{(l)}\dot{\gamma}_{ij}^{(l)} \tag{2-7}$$

where $\mathcal{D}_t$ is the upper-convected time derivative, $De^{(l)} = Gt_p^{(l)}$ is the Deborah or Weissenberg number and $\lambda_p^{(l)} = \eta_p^{(l)}/\eta$. The upper-convected time derivative is defined as (Bird [34]):

$$\mathcal{D}_t\tilde{\tau}_{ij} = d_t\tilde{\tau}_{ij} - \tilde{\tau}_{ik}\partial_k u_j - \tilde{\tau}_{kj}\partial_k u_i, \tag{2-8}$$

where $d_t\tilde{\tau_{ij}}$ is the material time derivative

$$d_t\tilde{\tau}_{ij} = \partial_t\tilde{\tau}_{ij} + u_k\partial_k\tilde{\tau}_{ij}, \tag{2-9}$$

with $\partial_t = \partial/\partial t$. In section 5.4, we discuss the implications of the differences between d_t and ∂_t on the numerical scheme resulting from, i.e. taking a Lagrangian or Eulerian description. In the next chapter we present further non-Newtonian models and discuss their microscopic basis.

To simplify the subsequent formulation, we incorporate a part of the Newtonian stress tensor into the non-Newtonian stress by redefining the non-Newtonian stress tensor as:

$$\tilde{\tau}_{ij}^{(l)} \rightarrow \tilde{\tau}_{ij}^{(l)} + (\lambda^{(l)} - 1)\dot{\gamma}_{ij}^{(l)}. \tag{2-10}$$

We can then use $\lambda^{(l)} = 1$ in (2-6) without loss of generality (Toose et al. [45, 46]). In the remainder of the thesis, the redefined non-Newtonian stress tensor will be referred to as the extra stress tensor.

Substitution of the stress tensor in (2-5) leads to:

$$\begin{cases} \partial_{jj}u_i^{(l)} - \partial_i P^{(l)} = -\partial_j\tilde{\tau}_{ij}^{(l)} \\ \partial_j u_j^{(l)} = 0. \end{cases} \tag{2-11}$$

Observe that (2-10) has been used here which implies an alteration in the source term on the right hand side depending on the viscosity ratio λ. This has specific consequences for the integral formulation of the solution to which

we return in chapter 4. In the remainder of this thesis, we will always indicate which non-Newtonian stress we use in case it is not clear from the context.

The velocity and the total stress tensor satisfy the following matching and asymptotic conditions:

$$[u_i]_{S^{(l)}} = 0 \tag{2-12}$$

$$[\pi_{ij} n_j]_{S^{(l)}} = q_i^{(l)} \tag{2-13}$$

$$u_i \rightarrow u_i^{\infty}, \quad \text{as} \quad |\boldsymbol{x}| \rightarrow \infty, \tag{2-14}$$

where $\boldsymbol{n}^{(l)}$ is the outward unit normal on $S^{(l)}$, $q_i^{(l)}$ is the viscous force exerted by the flow of the two liquids on the surface, and $[\ \cdot\ ]_{S^{(l)}}$ denotes the jump of the quantity between the brackets over the interface $S^{(l)}$, counted in the direction of $n^{(l)}$:

$$[f]_{S^{(l)}} = f^{(l-1)}(\boldsymbol{x}) - f^{(l)}(\boldsymbol{x}), \quad \boldsymbol{x} \rightarrow S^{(l)}. \tag{2-15}$$

In order to close the formulation of the problem, the viscous force $q_i^{(l)}$ needs to be related to the interface deformation This can be achieved by introducing a proper constitutive equation describing the behavior of the interface. As discussed in the introduction the behavior of a liquid-liquid interface is described, within a good approximation, by Laplace's law (Scriven [35] and Barthès-Biesel [36]):

$$q_i^{(l)} = \frac{1}{C^{(l)}} n_i^{(l)} \partial_j n_j^{(l)}, \tag{2-16}$$

where $\partial_j n_j^{(l)}$ is twice the local mean curvature of the interface.

As time-dependence does not appear explicitly in (2-11), we adopt a kinematic constraint to describe the fluid motion in the different domains. The motion of the domain $V^{(l)}$ (and its boundaries) is modelled by considering the domain as a set of material points. The trajectories of these points can be followed using a Lagrangian representation of the velocity:

$$d_t x_i = u_i^{(l)}(\boldsymbol{x}) \,, \quad \forall \boldsymbol{x} \in V^{(l)}(t), \tag{2-17}$$

where d_t is the material time derivative. This equation describes that the interfaces move with the local fluid velocity. For the evolution equations of the non-Newtonian stress tensor and these material points, initial conditions need to be specified. For the material points, we use the initial configuration of the specific problem as described in the subsections 2.1.1 and 2.1.2, whereas

for the non-Newtonian contribution to the stress tensor we assume an isotropic stress distribution:

$$\tilde{\tau}_{ij}(0) = Q\delta_{ij}, \tag{2-18}$$

with Q constant.

2.3 Macroscopic properties

In this section, we discuss some important properties that characterize the state of a single drop or a dispersion of drops. In the first part, we describe some important configurational properties of the drops; the corresponding rheological properties are discussed afterwards.

2.3.1 Configurational properties

In order to characterize the distortion of the interfaces of a compound drop due to the external velocity field, one commonly defines a deformation parameter $D^{(l)}$ as (Taylor [9]):

$$D^{(l)} = \frac{r^{(l)}_{max} - r^{(l)}_{min}}{r^{(l)}_{max} + r^{(l)}_{min}}, \quad l = 1, \ldots, K, \tag{2-19}$$

where $r^{(l)}_{max}$ and $r^{(l)}_{min}$ denote the longest and shortest principal axes of the l-th deformed interface. In case the drop is strongly distorted and does not resemble a near ellipsoidal shape, it is more convenient to use the deformation parameter $L^{(l)}$ (Li and Pozrikidis [30]):

$$L^{(l)} = r^{(l)}_{max}/R^{(l)} - 1 \tag{2-20}$$

to characterize the distortion.

For a dispersion of drops subjected to a shear flow, it is customary to characterize the orientation of the drops by introducing the orientation parameter θ. This parameter is defined as the angle between the direction along which the elongation of the drop is maximal (i.e. $r^{(1)}_{max}$) and the direction of the shear flow. The angle θ_k is computed from the moment of inertia tensor of the k-th drop (Goldstein [47] and Kennedy [48]):

$$I_{ij} = \int_{V_k} (\hat{x}_l \hat{x}_l \delta_{ij} - \hat{x}_i \hat{x}_j)\, d\boldsymbol{x}, \tag{2-21}$$

where V_k is the total volume of the k-th drop in the dispersion, $\hat{x}_i = x_i^c - x_i$ and x_i^c is the center of mass of the drop considered. By noting that in two dimensions (Kennedy [48] and Van der Klis and Toose [49]):

$$\hat{x}_l\hat{x}_l\delta_{ij} - \hat{x}_i\hat{x}_j = \frac{1}{4}\partial_l\left(\hat{x}_k\hat{x}_k\hat{x}_l\delta_{ij} - \hat{x}_i\hat{x}_j\hat{x}_l\right),$$

and using Gauss' theorem, expression (2-21) can be transformed into a boundary integral:

$$I_{ij} = \frac{1}{4}\int_{S_k^{(1)}}\left(\hat{x}_k\hat{x}_k\hat{x}_l\delta_{ij} - \hat{x}_i\hat{x}_j\hat{x}_l\right)n_l dS. \tag{2-22}$$

The eigenvector corresponding to the largest positive eigenvalue of I_{ij} defines the direction of maximum drop elongation and is used to compute θ_k (Kennedy [48]).

With the parameters $D^{(l)}$, $L^{(l)}$ and θ_k we have described the configuration of a single drop in an unbounded Newtonian fluid. To describe the configuration of a dispersion of drops, we simply compute the mean values of these parameters over all drops in the dispersion, i.e. over the drops in the periodic cell.

2.3.2 Rheological properties

The rheological properties of a single drop, or a dispersion of drops in a linear flow field are related to the effective stress tensor of a dispersion (Batchelor [50]). This effective stress tensor is defined as:

$$\Sigma_{ij} = \langle\pi_{ij}\rangle \equiv \frac{1}{V}\int_V \pi_{ij}d\boldsymbol{y},$$

where V is the total volume occupied by the dispersion. As the suspending fluid is Newtonian, we can rewrite this expression as:

$$\Sigma_{ij} = \frac{1}{V}\int_{V^{(0)}}\left\{-P\delta_{ij} + \dot{\gamma}_{ij}\right\}d\boldsymbol{y} + \frac{1}{V}\int_{V\backslash V^{(0)}}\pi_{ij}d\boldsymbol{y}, \tag{2-23}$$

where $V\backslash V^{(0)}$ is the volume of all drops in the dispersion. In the evaluation of the second integral in the expression (2-23), one must keep in mind that the surface tension acting along the different interfaces must be regarded as a singularity in the stress distribution with certain integral properties (Batchelor [50]). As such, the volume integral over the region $V\backslash V^{(0)}$ is improper and

must be treated appropriately. Following Batchelor [50] expression (2-23) can be rewritten as:

$$\Sigma_{ij} = \frac{1}{V}\int_{V^{(0)}} \{-P\delta_{ij} + \dot{\gamma}_{ij}\}\, d\boldsymbol{y} + \frac{1}{V}\sum_{k=1}^{N}\sum_{l=1}^{K}\int_{V_k^{(l)}} \pi_{ij}^{(l)} d\boldsymbol{y} + \frac{1}{V}\sum_{k=1}^{N}\sum_{l=1}^{K}\int_{S_k^{(l)}} x_j q_i^{(l)} dS, \tag{2-24}$$

where the summation is over all (N) drops in the system and over all (K) layers. It should be noted that the interfaces, along which a certain interfacial tension acts, are excluded in the domain integrals, i.e. $V_k^{(l)}$ is an open set. Using the explicit expressions for the total stress tensor $\pi_{ij}^{(l)}$ we obtain:

$$\Sigma_{ij} = \frac{1}{V}\int_{V} \{-P\delta_{ij} + \dot{\gamma}_{ij}\}\, d\boldsymbol{y} + \frac{1}{V}\sum_{k=1}^{N}\sum_{l=1}^{K}\int_{S_k^{(l)}} x_j q_i^{(l)} dS + \frac{1}{V}\sum_{k=1}^{N}\sum_{l=1}^{K}\int_{V_k^{(l)}} \left\{(\lambda^{(l)}-1)\dot{\gamma}_{ij}\right\} d\boldsymbol{y} + \frac{1}{V}\sum_{k=1}^{N}\sum_{l=1}^{K}\int_{V_k^{(l)}} \tilde{\tau}_{ij}^{(l)} d\boldsymbol{y}, \tag{2-25}$$

where we have rearranged (2-24) such that the integration in the first domain integral is performed over the total volume V instead of $V^{(0)}$. Observe that we did not use the redefined non-Newtonian stress tensor in the expression above. The advantage of this approach is that the viscosity ratio appears explicitly in (2-25) which makes it more applicable to a dispersion of Newtonian drops. Using Gauss' theorem, the second domain integral in (2-25) can be rewritten as

$$\int_{V_k^{(l)}} \left\{(\lambda^{(l)}-1)\dot{\gamma}_{ij}\right\} d\boldsymbol{y} = \int_{S_k^{(l)}} (\lambda^{(l)}-1)(u_i n_j + u_j n_i) dS - \int_{S_k^{(l+1)}} (\lambda^{(l)}-1)(u_i n_j + u_j n_i) dS.$$

In case $l = K$, the integral over the surface $S^{(K+1)}$ is not present. Substituting this expression into (2-25) we finally obtain:

$$\Sigma_{ij} = -\langle P\rangle \delta_{ij} + \langle\dot{\gamma}_{ij}\rangle + \frac{1}{V}\sum_{k=1}^{N}\sum_{l=1}^{K}\int_{V_k^{(l)}} \tilde{\tau}_{ij}^{(l)} d\boldsymbol{y} + \frac{1}{V}\sum_{k=1}^{N}\sum_{l=1}^{K}\int_{S_k^{(l)}} \left\{x_j q_i^{(l)} + (\lambda^{(l)} - \lambda^{(l-1)})(u_i n_j + u_j n_i)\right\} dS. \tag{2-26}$$

With (2-26) we have constructed an expression for the effective stress in terms of the non-Newtonian stress tensor, the surface force $\boldsymbol{q}$ and the viscosity ratios $\lambda^{(l)}$. For $K = 1$ and $\tilde{\tau}_{ij}^{(l)} = 0$ expression (2-26) reduces to the expression which was also obtained by Batchelor for simple viscous drops.

Based on this effective stress tensor several rheological properties can be defined. For a periodic dispersion of two-dimensional drops we introduce the following variables (Bird et al. [34]):

$$\eta_{\text{eff}} = \frac{\Sigma_{12}}{\langle\dot{\gamma}_{12}\rangle}, \qquad N_{\text{eff}}^1 = \frac{\Sigma_{11} - \Sigma_{22}}{\langle\dot{\gamma}_{12}\rangle^2}, \tag{2-27}$$

where η_{eff} is the effective shear viscosity, and N_{eff}^1 the effective normal stress difference. The domain V is chosen equal to the basic periodic cell.

In case the dispersion is sufficiently dilute, the interactions between the drops may be neglected. The flow of each drop then behaves as if it were dispersed in an infinite fluid. In this case the contribution of each drop is the same and (2-26) can be approximated by:

$$\Sigma_{ij} = -\langle P\rangle\,\delta_{ij} + \langle\dot{\gamma}_{ij}\rangle + \frac{N}{V}\sum_{l=1}^{K}\int_{V^{(l)}}\tilde{\tau}_{ij}^{(l)}\,d\boldsymbol{y} + \frac{N}{V}\sum_{l=1}^{K}\int_{S^{(l)}}\left\{x_j q_i^{(l)} + (\lambda^{(l)} - \lambda^{(l-1)})(u_i n_j + u_j n_i)\right\}dS, \tag{2-28}$$

where N/V is the number concentration. The integration in (2-28) is performed over a single compound drop in an infinite fluid. For an axisymmetric compound drop placed in an elongational flow field, we introduce an elongational viscosity η_{eff}^E (Bird et al. [34]):

$$\eta_{\text{eff}}^E = 2\frac{\Sigma_{11} - \Sigma_{22}}{\langle\dot{\gamma}_{11}\rangle}, \tag{2-29}$$

where Σ_{11} and Σ_{22} are defined according to (2-28).

Chapter 3

Rheological models

As mentioned in the introduction, polymer blends and vesicle dispersions are typical examples of non-Newtonian (compound) drop systems. In order to describe the morphology and rheology in these applications, one has to assume an appropriate constitutive equation for the non-Newtonian material of which the drop is composed. In the first section of this chapter, we discuss several constitutive equations for polymer solutions. In section 3.2, we introduce a number of network models, which are used to model the behavior of a vesicle membrane. Finally, in section 3.3 we discuss the viscometric properties (idealized rheological properties) of the different rheological models introduced in this chapter.

3.1 Elastic dumbbell models

A commonly adopted way to describe a polymer solution is to idealize a polymer molecule in this solution as an elastic dumbbell consisting of two beads of mass m each, joined by a non-bendable spring (Bird et al. [51]). The beads of the elastic dumbbell are labeled "1" and "2" and their instantaneous locations in space are denoted by $\boldsymbol{r}^1$ and $\boldsymbol{r}^2$ respectively (see figure 3-1). The connector $\boldsymbol{R} = \boldsymbol{r}^2 - \boldsymbol{r}^1$ describes the overall orientation and internal configuration of the polymer molecule. We may thus describe the configuration by either specifying $\boldsymbol{r}^1$, $\boldsymbol{r}^2$ or $\boldsymbol{R}$, and the center of mass of the dumbbell. The aim of the following derivation is to arrive at an expression for the stress tensor corresponding to this idealized model. In the derivation, we closely follow Bird et al. [51].

The distorting effect of the imposed flow is incorporated by calculating the viscous drag forces on the macromolecule. Using the Stokes drag law, the

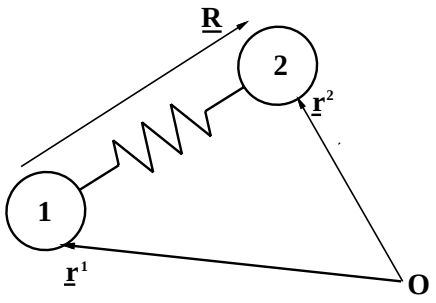

Figure 3-1: Schematic representation of an elastic dumbbell

force $\boldsymbol{f}^{H\,\alpha}$ acting on the α-th bead is given by (Bird et al. [51]):

$$f_i^{H\,\alpha} = \frac{\zeta}{\eta a}(r_j^\alpha \partial_j u_i - \partial_t r_i^\alpha), \quad \alpha = 1, 2,$$

with ζ the friction coefficient of the beads. Note that the force has been made dimensionless with $\eta G a^2$. Due to thermal fluctuations in the fluid, the end to end vector $\boldsymbol{R}$ of the polymer chain tends to have an isotropic spherical distribution, whereas the total molecule experiences an average force. The first property is represented by the spring in the model, which tries to reduce the distortion of $\boldsymbol{R}$. The spring force $\boldsymbol{f}^c$ is defined as:

$$f_i^c = f_i^{c\,1} = -f_i^{c\,2} = \frac{H}{\eta G a} f(|\boldsymbol{R}|) R_i, \tag{3-1}$$

with H being the spring constant and $f(|\boldsymbol{R}|)$ a function representing the non-linear character of the spring. The average force on the dumbbell due to the thermal fluctuations is commonly denoted by the Brownian force $\boldsymbol{f}^B$. In the derivation here, we use a smoothened Brownian motion force (Bird et al. [51]):

$$f_i^{B\,\alpha} = \frac{kT}{\eta G a^3} \frac{\partial}{\partial r_i^\alpha} \log \Psi(\boldsymbol{r}^1, \boldsymbol{r}^2, t), \tag{3-2}$$

with k the Boltzmann constant and T the temperature. In the expression above, $\Psi(\boldsymbol{r}^1, \boldsymbol{r}^2, t)$ is the configuration distribution function which represents the chance of finding a dumbbell at the position $\{\boldsymbol{r}^1, \boldsymbol{r}^2\}$ at time t. Assuming that the distribution is independent of position in space, we can rewrite $\Psi(\boldsymbol{r}^1, \boldsymbol{r}^2, t)$ as:

$$\Psi(\boldsymbol{r}^1, \boldsymbol{r}^2, t) = \psi(\boldsymbol{R}, t),$$

where $\psi(\boldsymbol{R},t)$ denotes the number of dumbbells within a range $d\boldsymbol{R}$ around $\boldsymbol{R}$ at time t. As the function $\psi(\boldsymbol{R},t)$ contains the distribution of all possible configurations within an ensemble of dumbbells, one can use this function to calculate ensemble averages of any function $g(\boldsymbol{R})$ by:

$$\langle\!\langle g \rangle\!\rangle \equiv \int g(\boldsymbol{R})\psi(\boldsymbol{R},t)\, d\boldsymbol{R}, \tag{3-3}$$

where the integration is over all possible configurations and $\langle\!\langle \cdot \rangle\!\rangle$ denotes the average.

The evolution of ψ in time is described by the equation of continuity in configuration space (Bird et al. [51]):

$$\partial_t \psi(\boldsymbol{R},t) + \frac{\partial}{\partial R_i}\left(\psi(\boldsymbol{R},t)\partial_t R_i\right) = 0. \tag{3-4}$$

It is seen that this expression relates the evolution of the distribution function to the time derivative of the configuration vector R_i. The latter quantity follows from the force balances for the beads in the dumbbell model:

$$\boldsymbol{f}^{H\,\alpha} + \boldsymbol{f}^{c\,\alpha} + \boldsymbol{f}^{B\,\alpha} = 0, \quad \alpha = 1,2. \tag{3-5}$$

By subtracting (3-5) for $\alpha = 1$ and $\alpha = 2$ we arrive at the following equation of motion for $\boldsymbol{R}$:

$$\partial_t R_i = R_j \partial_j u_i - \frac{2kT}{Ga^2\zeta}\frac{\partial}{\partial R_i}\log\psi(\boldsymbol{R},t) - \frac{2}{G\zeta}Hf(|\boldsymbol{R}|)R_i. \tag{3-6}$$

Substituting this expression into the equation of continuity for the distribution function (3-4) one finally obtains the diffusion equation (Bird et al. [51]):

$$\frac{\partial\psi(\boldsymbol{R},t)}{\partial t} = -\frac{\partial}{\partial R_i}\left\{(\partial_j u_i)R_j\psi - \frac{2kT}{Ga^2\zeta}\frac{\partial\psi}{\partial R_i} - \frac{2H}{G\zeta}f(|\boldsymbol{R}|)R_i\psi\right\}. \tag{3-7}$$

This expression describes the way in which the distribution of configurations changes with time. Multiplying (3-7) with R_iR_j and integrating over the total configuration space we obtain:

$$d_t\langle\!\langle R_iR_j \rangle\!\rangle - \langle\!\langle R_iR_k \rangle\!\rangle\partial_k u_j - \langle\!\langle R_kR_j \rangle\!\rangle\partial_k u_i = \frac{4kT}{Ga^2\zeta}\delta_{ij} - \frac{4H}{G\zeta}\langle\!\langle f(|\boldsymbol{R}|)R_iR_j \rangle\!\rangle, \tag{3-8}$$

which describes the evolution of the second moment $\langle\!\langle R_iR_j \rangle\!\rangle$ of a dumbbell in a flow field $\boldsymbol{u}$.

Scaling the size R of the molecule such that $\langle\!\langle R_i R_j \rangle\!\rangle = \delta_{ij}$ in the absence of a velocity field and using the upper-convected time derivative as defined in equation (2-8) we find the following expression (Chilcott and Rallison [56]):

$$\mathcal{D}_t \langle\!\langle R_i R_j \rangle\!\rangle = \frac{1}{De} \left\{ \delta_{ij} - \langle\!\langle f(|\boldsymbol{R}|) R_i R_j \rangle\!\rangle \right\}, \tag{3-9}$$

with $De = G\zeta/4H$ the Deborah number. In the sequel of this thesis $\langle\!\langle R_i R_j \rangle\!\rangle = \delta_{ij}$ is also used as the initial condition for the evolution equation (3-9). To complete the description of the elastic dumbbell model, we introduce the relation between the stress and the deformed dumbbells (Kramers [52]):

$$\tilde{\tau}_{ij} = \frac{\lambda c}{De} \left\{ \langle\!\langle f(|\boldsymbol{R}|) R_i R_j \rangle\!\rangle - \delta_{ij} \right\}, \tag{3-10}$$

where c is a measure for the concentration of the polymer molecules in the suspending fluid (Chilcott and Rallison [56]). Substituting (3-9) into (3-10) we obtain the Giesekus expression for the stress (Giesekus [53]):

$$\tilde{\tau}_{ij} = -\lambda c \mathcal{D}_t \langle\!\langle R_i R_j \rangle\!\rangle. \tag{3-11}$$

With (3-9), (3-10) and (3-11) we have introduced the governing equations describing the rheological behavior of a dilute system of elastic dumbbells. For the spring function $f(|\boldsymbol{R}|)$ several choices can be made which are discussed next.

The simplest choice is to take $f(|\boldsymbol{R}|) = 1$, which corresponds to a linear spring. By combining the different expressions for the stress tensor we find the following equation governing the non-Newtonian stress tensor:

$$De \mathcal{D}_t \tilde{\tau}_{ij} + \tilde{\tau}_{ij} = \lambda c \dot{\gamma}_{ij}. \tag{3-12}$$

This expression was already introduced in equation (2-7) of the previous chapter. By substituting the expression for the total stress tensor (2-6) into this equation, we obtain the more familiar form of the Oldroyd-B fluid (Bird et al. [34]):

$$De \mathcal{D}_t \tilde{\pi}_{ij} + \tilde{\pi}_{ij} = \lambda(1+c) \left\{ \dot{\gamma}_{ij} + \frac{De}{1+c} \mathcal{D}_t \dot{\gamma}_{ij} \right\}, \tag{3-13}$$

where $\tilde{\pi}_{ij}$ differs from π_{ij} by an isotropic pressure. In this expression, De is a relaxation time, $De/(1+c)$ a retardation time and $\lambda(1+c)$ the zero shear rate viscosity. In our numerical simulations, however, we use equation (3-12) for the non-Newtonian stress tensor directly.

The linear spring law is appropriate for small distortions of the macromolecule. The "correct" nonlinear force, at least for a linear chain with freely hinged bonds, which is also valid for large distortions is the inverse Langevin force (Bird et al. [51]). Given the simplicity of the dumbbell model, it is more convenient to adopt a simpler Finitely Extensible Nonlinear Elastic (FENE) spring force law (Bird et al. [51]):

$$f_i^c = Hf(|\boldsymbol{R}|)R_i = \frac{HR_i}{1 - |\boldsymbol{R}|^2/L^2}. \tag{3-14}$$

where L is the maximum extension of the spring in the dumbbell. A problem with this nonlinear law is that we cannot evaluate the right-hand side of expression (3-9), since the distribution function is unknown. A common way to circumvent this problem is by approximating $\langle\!\langle f(|\boldsymbol{R}|)R_iR_j \rangle\!\rangle$ as (Peterlin [54]):

$$\langle\!\langle f(|\boldsymbol{R}|)R_iR_j \rangle\!\rangle \approx f(\langle\!\langle |\boldsymbol{R}| \rangle\!\rangle)\langle\!\langle R_iR_j \rangle\!\rangle,$$

where $f(\langle\!\langle |\boldsymbol{R}| \rangle\!\rangle)$ is the "pre-averaged" spring force:

$$f(\langle\!\langle |\boldsymbol{R}| \rangle\!\rangle) = \frac{1}{1 - R^2/L^2}, \quad \text{with } R^2 = \mathrm{tr}(\langle\!\langle R_iR_j \rangle\!\rangle).$$

Observe that the evolution of $\langle\!\langle R_iR_j \rangle\!\rangle$ can be calculated with (3-9) without knowing the distribution function ψ.

The implications of this "pre-averaging" technique are extensively discussed by Keunings [55]. The relation for the non-Newtonian stress tensor now becomes:

$$\tilde{\tau}_{ij} = \frac{\lambda c}{De}\left\{f(\langle\!\langle |\boldsymbol{R}| \rangle\!\rangle)\langle\!\langle R_iR_j \rangle\!\rangle - \delta_{ij}\right\}, \tag{3-15}$$

whereas the evolution equation (3-9) reduces to:

$$\mathcal{D}_t\langle\!\langle R_iR_j \rangle\!\rangle = \frac{1}{De}\left\{\delta_{ij} - f(\langle\!\langle |\boldsymbol{R}| \rangle\!\rangle)\langle\!\langle R_iR_j \rangle\!\rangle\right\}. \tag{3-16}$$

The expression above and (3-15) are referred to as the FENE-P model in the sequel of this thesis. A slightly different approach was followed by Cillcott and Rallison [56] leading to:

$$\mathcal{D}_t\langle\!\langle R_iR_j \rangle\!\rangle = \frac{f(\langle\!\langle |\boldsymbol{R}| \rangle\!\rangle)}{De}\left\{\delta_{ij} - \langle\!\langle R_iR_j \rangle\!\rangle\right\}, \tag{3-17}$$

which will be denoted as the CR model.

3.2 Network models

In the previous section we introduced several models describing the rheological behavior of dilute polymer solutions. When the concentration of polymer is increased, these models are no longer valid. One of the main reasons for the limited validity of these theories is the occurrence of polymer-polymer interactions in a concentrated polymer solution. In order to model these interactions a common approach followed in literature is to introduce a molecular network (Bird et al. [51]). In this network approach one introduces so-called junctions,

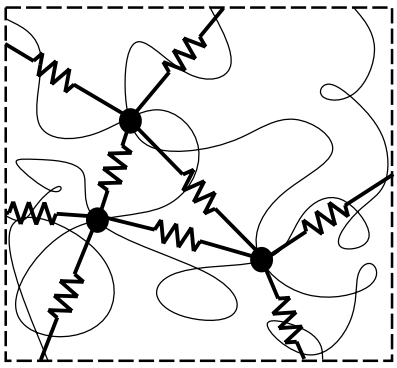

Figure 3-2: Schematic representation of a concentrated polymer solution and the corresponding network.

which mark the interaction between two polymer chains. These junctions can be chemical crosslinks (e.g. crosslinked rubber) or physical entanglement (e.g. polymer melts), i.e. permanent or temporary. The macromolecular chains between these junctions are modeled using simple linear springs as sketched in figure 3-2. In the description of the network models presented in this section we closely follow Bird et al. [51].

Using a similar approach as sketched in the previous section, the constitutive equation for a network model with permanent junctions (i.e. crosslinked rubber) is given by:

$$\tilde{\tau}_{ij} = \frac{c_1}{G\eta} B_{ij}, \tag{3-18}$$

where c_1 is a measure for the number of crosslinks per unit volume in the rubber material. In expression (3-18) B_{ij} is the so-called left Cauchy-Green-

strain tensor which is defined as (Bird et al. [34]):

$$B_{ij} = \frac{\partial x_i}{\partial X_k}\frac{\partial x_j}{\partial X_k}, \tag{3-19}$$

where $\boldsymbol{x}$ describes the present and $\boldsymbol{X}$ the initial configuration of the material. The constitutive equation (3-18) is often referred to as the equation of a "neo-Hookean" material. A generalization of this model was proposed by Mooney [57]:

$$\tilde{\tau}_{ij} = \frac{c_1}{G\eta}B_{ij} - \frac{c_2}{G\eta}B_{ij}^{-1}, \tag{3-20}$$

where c_1 and c_2 are arbitrary constants. The inclusion of the term B_{ij}^{-1} gives an improved agreement with experimental results. However, the molecular basis of the term B_{ij}^{-1} is not clear. In literature, the Mooney constitutive equation is often used to describe the elastic behavior of a lipid bilayer membrane (see Barthès-Biesel [36] and chapter 1 of this thesis).

The total stress tensor π_{ij} corresponding to the Mooney constitutive equation will be referred to as the viscoelastic model. In this thesis, we focus on two special cases. In the first case, identified as "viscoelastic I", we set $c_2 = 0$, whereas in the second case $c_1 = 0$ which is referred to as "viscoelastic II". It is noted that the stress tensor for a viscoelastic model is a function of the deformation of the material, rather than a function of the rate of deformation as is the case of the models presented in the previous section. A material which is described by the rubber model can therefore be seen as a viscoelastic solid. For a network model with non-permanent junctions, however, the material should still be regarded as a fluid.

3.3 Viscometric properties

With the Oldroyd-B, FENE-P, CR and Mooney models, we have introduced a set of rheological models capable of approximately describing the non-Newtonian character of dilute as well as concentrated polymer solutions. The essential non-Newtonian properties of the different models are usually studied in a linear flow field in which they can be evaluated analytically or numerically. Rheological properties determined in these simple flows are usually called the viscometric properties of the model (Bird et al. [34]). The viscometric properties of a non-Newtonian model subjected to a simple shear flow (equation (2-1) with $\alpha = 0$) are given by the shear viscosity η_s and the first normal stress

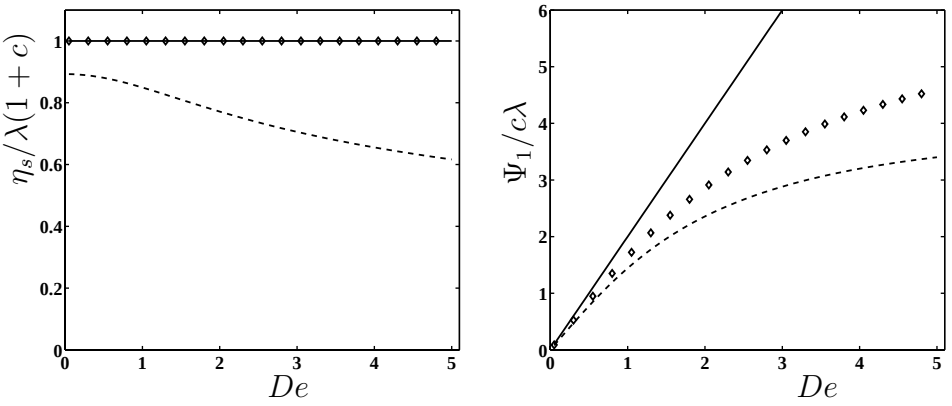

(a) Shear viscosity (b) Normal stress

Figure 3-3: Viscometric properties of the three different dumbbell models subject to a shear flow. The Oldroyd-B and FENE-P model are represented by the solid and dashed line respectively; the CR-model is represented by the symbols.

function Ψ_1 (Bird et al. [34]):

$$\eta_s = \frac{\pi_{12}}{\dot{\gamma}_{12}}, \qquad \Psi_1 = \frac{\pi_{11} - \pi_{22}}{\dot{\gamma}_{12}^2}. \tag{3-21}$$

For an elongational flow (equation (2-1) with $\alpha = 1$) one usually introduces an elongational viscosity η_E:

$$\eta_E = 2\frac{\pi_{11} - \pi_{22}}{\dot{\gamma}_{11}}. \tag{3-22}$$

We first consider the viscometric properties of the dumbbell models; the network models are discussed at the end of this section.

In figure 3-3(a), we plot the steady-state shear viscosity of the different dumbbell models introduced in this chapter. The viscometric properties for the Oldroyd-B model were found by solving (3-12) analytically and substituting the result in (2-6). Due to the nonlinear character of the spring force, the viscometric properties of the CR and FENE-P model cannot be found analytically. In these cases, we either solve (3-16) or (3-17) numerically using a Runge-Kutta time stepping method. The steady-state value of the second moment $\langle\!\langle R_i R_j \rangle\!\rangle$ is subsequently substituted in (3-15) to yield the non-Newtonian

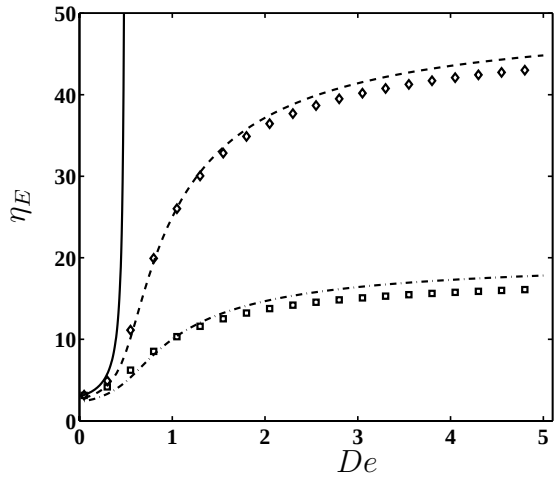

Figure 3-4: Elongational viscosity of the three different dumbbell models. The Oldroyd-B model is represented by the solid line. The dash-dotted and dashed lines indicate the FENE-P model with $L^2 = 10$ and $L^2 = 25$ respectively. The CR-model with $L^2 = 10$ and $L^2 = 25$ is represented by the square and diamond symbols respectively.

stress tensor from which the viscometric properties are calculated. From figure 3-3(a) it follows that the steady-state shear viscosity is constant for the Oldroyd-B and CR-model, whereas the shear viscosity of the FENE-P model is decreasing with increasing Deborah number (i.e. shear thinning occurs). A constant shear rate viscosity is convenient in case we want to compare a Newtonian with a non-Newtonian drop at similar viscosity ratios. The steady state first normal stress for the Oldroyd-B model, as shown in figure 3-3(b), is increasing linearly with the Deborah number. Due to the finite extensibility of the FENE type spring, the FENE-P and CR models have a finite steady-state first normal stress.

In contrast to the shear viscosity, the elongational viscosity is strongly dependent on the type of dumbbell model chosen. In figure 3-4 it is seen that the elongational viscosity of the Oldroyd-B model is infinite for Deborah numbers larger than 0.5. This artifact is caused by the fact that the spring in the dumbbell model is infinitely extended in an elongational flow (Rallison and Hinch [58]). In chapter 4 we discuss the implications of the singular behavior of the Oldroyd-B model on the numerical method. Due to the finite extensibility of the spring in the FENE type dumbbells, the FENE-P and CR model show a bounded elongational viscosity. The maximum value of this

viscosity is strongly dependent on the maximum length of the spring in the dumbbell.

For a rubber-like material defined in (3-20) the viscometric properties are based on the total strain rather than on the rate-of-strain as is the case for dumbbell models. When a rubber is elongated, the relation between the present configuration $\boldsymbol{x}$ and its original configuration $\boldsymbol{X}$ is given by:

$$x_1 = \xi X_1,\ x_2 = \xi^{-1/2} X_2,\ x_3 = \xi^{-1/2} X_3,$$

where ξ is a measure of the total strain. The non-zero components of the total stress tensor are given by:

$$\pi_{11} - \pi_{22} = 2\lambda(1 + \xi^{-3/2})\partial_t \xi + \frac{c_1}{G\eta}(\xi^2 - \xi^{-1}) + \frac{c_2}{G\eta}(\xi^{-2} - \xi). \qquad (3\text{-}23)$$

Note that the first term at the right-hand side of this expression represents the viscous contribution to the total stress tensor. From (3-23), it follows that there will be a stress present as long as the material is deformed (i.e. $\xi \neq 1$). A direct implication of this fact is that we do not need a surface tension acting along the interface of a rubber-like drop to obtain a steady-state solution if this drop is subjected to an elongational flow. A more detailed and thorough discussion of rubber-like particles placed in an elongational flow is given by Roscoe [59].

In this chapter we have discussed several models which can be used to describe the non-Newtonian character of a simple or a compound drop. It was found that dumbbell models like Oldroyd-B, FENE-P and CR can be used for dilute polymer solutions, whereas network models are to be used for concentrated polymer solutions. From the viscometric properties it was found that the CR model is the most appropriate model since it has a constant shear viscosity and bounded normal stresses in all flow types.

Chapter 4

Integral formulation

In this chapter we formulate the solution to the Stokes equations in terms of boundary integral expressions assuming that the non-Newtonian stress tensor is known. In the first section we give a short introduction to the boundary integral method. In section 4.2 we present the boundary integral formulation for a single compound drop. The special case of axisymmetric flow is discussed in section 4.3. Finally, the extension of the boundary integral formulation to a periodic suspension of drops is given in section 4.4.

4.1 Boundary-integral formulation for Stokes flow

In this section, we present the basic ingredients of the boundary integral formulation for Stokes flow. We consider a simply-connected open domain V bounded by a surface S. For reasons of convenience we assume that S is continuously differentiable. The governing equations for Stokes flow within Ω are given by:

$$\begin{cases} \lambda \partial_{jj} u_i - \partial_i P = f_i \\ \partial_j u_j = 0, \end{cases} \tag{4-1}$$

where f_i is a certain force density, i.e. $f_i = -\partial_j \tilde{\tau}_{ij}$ in chapter 2. The Stokes-flow equations given above are further supplemented with suitable boundary conditions at the boundary S. In general one either specifies velocity $\boldsymbol{u}$ or the traction $\tau_{ij} n_j$, with τ_{ij} the viscous stress tensor which is defined as:

$$\tau_{ij} = -P\delta_{ij} + \lambda(\partial_i u_j + \partial_j u_i). \tag{4-2}$$

To reformulate (4-1) in terms of boundary integrals we consider the Lorentz reciprocal theorem (Lorentz [23]):

$$\int_V \left\{ (\lambda \partial_{jj} u_i - \partial_i P)\, u_i' - \left(\lambda \partial_{jj} u_i' + \partial_i P'\right) u_i \right\} d\,\boldsymbol{y} = \int_S \left(u_i' \tau_{ij} - u_i \tau_{ij}' \right) n_j d\,S, \tag{4-3}$$

where $\boldsymbol{u}'$ and P' are arbitrary velocity and pressure fields satisfying the Stokes equations and $\boldsymbol{n}$ is the outward unit normal on S. The viscous stress tensor τ_{ij}' in (4-3) is defined as:

$$\tau_{ij}' = P' \delta_{ij} + \lambda(\partial_i u_j' + \partial_j u_i').$$

Although (4-3) is actually an integral formulation of the Stokes equations we still need to specify $\boldsymbol{u}'$ and P'. In the boundary-integral method, these functions are chosen to satisfy the singular Stokes problem:

$$\begin{cases} \lambda \partial_{jj} u_{ik}'(\boldsymbol{x}, \boldsymbol{y}) - \partial_i P_k'(\boldsymbol{x}, \boldsymbol{y}) = \delta(\boldsymbol{x} - \boldsymbol{y}) \delta_{ik} \\ \partial_j u_{jk}'(\boldsymbol{x}, \boldsymbol{y}) = 0, \end{cases} \tag{4-4}$$

where $\delta(\boldsymbol{x} - \boldsymbol{y})$ is the Dirac delta function and the derivatives are carried out with respect to the variable $\boldsymbol{x}$. Solving (4-4) using Fourier transforms we find the Green's functions for the Stokes problem in three dimensions (Lorentz [23] and Ladyzhenskaya [60]):

$$u_{ik}'(\boldsymbol{x}, \boldsymbol{y}) = -\frac{1}{8\pi\lambda} \left\{ \frac{\delta_{ik}}{|\boldsymbol{r}|} + \frac{r_i r_k}{|\boldsymbol{r}|^3} \right\} \tag{4-5}$$

$$P_k'(\boldsymbol{x}, \boldsymbol{y}) = -\frac{1}{4\pi} \frac{r_k}{|\boldsymbol{r}|^3}, \tag{4-6}$$

with $\boldsymbol{r} = \boldsymbol{x} - \boldsymbol{y}$. The reason for taking the solutions of the singular Stokes problem as a choice for $\boldsymbol{u}'$ and P' becomes apparent when we recall that in the argument $\boldsymbol{y}$ the functions $u_{ik}'(\boldsymbol{x}, \boldsymbol{y})$ and $P_k'(\boldsymbol{x}, \boldsymbol{y})$ satisfy the adjoint system:

$$\lambda \partial_{jj}^y u_{ik}'(\boldsymbol{x}, \boldsymbol{y}) + \partial_i^y P_k'(\boldsymbol{x}, \boldsymbol{y}) = \delta(\boldsymbol{x} - \boldsymbol{y}) \delta_{ik}, \quad \partial_j^y u_{jk}'(\boldsymbol{x}, \boldsymbol{y}) = 0,$$

with $\partial_j^y = \partial / \partial y_j$. Substituting $u_{ik}'(\boldsymbol{x}, \boldsymbol{y})$ and $P_k'(\boldsymbol{x}, \boldsymbol{y})$ into (4-3) we obtain for any $\boldsymbol{x} \in V$:

$$u_k(\boldsymbol{x}) = \int_V f_i u_{ik}' d\,\boldsymbol{y} + \int_S K_{ijk} u_i n_j d\,S_y - \int_S u_{ik}' \tau_{ij} d\,S_y, \tag{4-7}$$

where for reasons of convenience we defined K_{ijk} as τ'_{ij} calculated with u'_{ik} and P'_k (differentiations with respect to $\boldsymbol{y}$):

$$K_{ijk}(\boldsymbol{x},\boldsymbol{y}) = -\frac{3}{4\pi}\frac{r_i r_j r_k}{|\boldsymbol{r}|^5}. \tag{4-8}$$

In case we wish to formulate the velocity for a point that lies outside V or on S special care has to be taken since the second integral on the right-hand side of (4-7) is discontinuous over S. Following Ladyzhenskaya [60] we arrive at the following integral expression which is valid in the entire domain:

$$\lambda c_{ik} u_i(\boldsymbol{x}) = -\int_V f_i J_{ik} d\,\boldsymbol{y} + \lambda \int_S K_{ijk} u_i n_j d\,S_y + \int_S J_{ik}\tau_{ij} d\,S_y, \tag{4-9}$$

where we have introduced the notation:

$$J_{ik}(\boldsymbol{r}) = -\lambda u'_{ik}(\boldsymbol{x},\boldsymbol{y}) = \frac{1}{8\pi}\left\{\frac{\delta_{ik}}{|\boldsymbol{r}|} + \frac{r_i r_k}{|\boldsymbol{r}|^3}\right\} \tag{4-10}$$

The coefficients c_{ik} are given by:

$$c_{ik} = \begin{cases} \delta_{ik} \text{ if} & \boldsymbol{x} \in V \\ \frac{1}{2}\delta_{ik} \text{ if} & \boldsymbol{x} \in S \\ 0 \quad \text{otherwise,} & \end{cases} \tag{4-11}$$

where S is a continuously differentiable surface.

With (4-9) we have expressed the velocity field in the entire domain in terms of domain and boundary integrals. When the velocity is specified at the boundary we have a so-called Fredholm equation of the first kind, whereas the specification of the normal component of stress tensor at S leads to a Fredholm equation of the second kind. In the next section, we apply the integral equation to describe a compound non-Newtonian drop, which leads to a Fredholm equation of the second kind.

4.2 Single compound drop

In chapter 2 of this thesis, we argued that the flow inside and around a small compound (non-)Newtonian drop is governed by Stokes flow since the typical Reynolds number is small. Assuming that the non-Newtonian stress tensor is known at time t, we can treat the term on the right-hand side of (2-11) as a source term. In this manner we can express the velocity field by means of

boundary integral equations (Lorentz [23] and Ladyzhenskaya [60]). Extending (4-9) to a situation with multiple boundaries, the solution for the velocity field in the entire domain is represented by:

$$c_{ik}^{(l)}\lambda^{(l)}u_i(\boldsymbol{x}) - \lambda^{(l)}\int_{S^{(l)}} K_{ijk}(\boldsymbol{r})u_i(\boldsymbol{y})n_j(\boldsymbol{y})\,dS_y + \lambda^{(l)}\int_{S^{(l+1)}} K_{ijk}(\boldsymbol{r})u_i(\boldsymbol{y})n_j(\boldsymbol{y})\,dS_y = \int_{V^{(l)}} J_{ik}(\boldsymbol{r})\partial_j\tilde{\tau}_{ij}^{(l)}(\boldsymbol{y})\,d\boldsymbol{y} + \int_{S^{(l)}} J_{ik}(\boldsymbol{r})\tau_{ij}^{(l)}(\boldsymbol{y})n_j(\boldsymbol{y})\,dS_y - \int_{S^{(l+1)}} J_{ik}(\boldsymbol{r})\tau_{ij}^{(l)}(\boldsymbol{y})n_j(\boldsymbol{y})\,dS_y \quad (4\text{-}12)$$

with $\boldsymbol{r} = \boldsymbol{x} - \boldsymbol{y}$ and $l = 0, \ldots, K$. When $l = K$, the integrals over the surface $S^{(K+1)}$ are not present. The coefficients $c_{ik}^{(l)}$ are defined similar to (4-11):

$$c_{ik}^{(l)} = \begin{cases} \delta_{ik} \text{ if } & \boldsymbol{x} \in V^{(l)} \\ \frac{1}{2}\delta_{ik} \text{ if } & \boldsymbol{x} \in S^{(l)} \cup S^{(l+1)} \\ 0 \quad \text{otherwise,} & \end{cases} \quad (4\text{-}13)$$

where it is assumed that each $S^{(l)}$ is a continuously differentiable surface. In the outer domain $V^{(0)}$ the integral equation (4-12) takes the following form:

$$c_{ik}^{(0)}u_i(\boldsymbol{x}) + \int_{S^{(1)}} K_{ijk}u_i n_j\,dS_y = u_k^{\infty}(\boldsymbol{x}) - \int_{S^{(1)}} J_{ik}\tau_{ij}^{(1)}n_j\,dS_y, \quad (4\text{-}14)$$

where we have used the boundary condition (2-14) at infinity to perform the integrations over the boundary $S^{(0)}$. The domain integral is not present in (4-14) as the outer fluid is Newtonian. With the equations (4-12) through (4-14) we have represented the flow problem in terms of domain and boundary integrals which can be evaluated explicitly using the matching conditions given in chapter 2. The aim of the derivation presented in the rest of this section is to arrive at an integral expression which is more appropriate for an explicit (numerical) evaluation.

First, we rewrite the domain integral in (4-12) using the Gauss divergence theorem in order to obtain a better connection with the matching conditions (2-13) and (2-14). The resulting expression reads:

$$\lambda^{(l)}c_{ik}^{(l)}u_i(\boldsymbol{x}) - \lambda^{(l)}\int_{S^{(l)}} K_{ijk}u_i n_j\,dS_y + \lambda^{(l)}\int_{S^{(l+1)}} K_{ijk}u_i n_j\,dS_y = -\int_{V^{(l)}} \tilde{\tau}_{ij}^{(l)}\partial_j^y J_{ik}\,d\boldsymbol{y} + \int_{S^{(l)}} J_{ik}\pi_{ij}^{(l)}n_j\,dS_y - \int_{S^{(l+1)}} J_{ik}\pi_{ij}^{(l)}n_j\,dS_y. \quad (4\text{-}15)$$

However, in order to apply the divergence theorem it is necessary that the non-Newtonian stress tensor is continuous and has bounded derivatives. Numerical simulations of a two-dimensional drop indicated that the non-Newtonian stress tensor for an Oldroyd-B fluid satisfies these conditions for sufficiently small capillary numbers (Toose et al. [45]). However, for high capillary and Deborah numbers the non-Newtonian stress tensor for an Oldroyd-B fluid might become singular, as discussed in chapter 3. In these cases (i.e. high capillary and Deborah numbers) it might be necessary to use a FENE-P or a CR model instead.

The next step is the elimination of $\pi_{ij}^{(l)}$ in (4-15) by matching the integral expressions for the domains $V^{(l-1)}$ and $V^{(l)}$ using the boundary conditions (2-13) and (2-14):

$$\begin{aligned}
&\frac{1}{2}(\lambda^{(l-1)}+\lambda^{(l)})u_k(\boldsymbol{x}) - \lambda^{(l-1)}\int_{S^{(l-1)}} K_{ijk}u_i n_j\, dS_y + \\
&\quad (\lambda^{(l-1)}-\lambda^{(l)})\int_{S^{(l)}} K_{ijk}u_i n_j\, dS_y + \lambda^{(l)}\int_{S^{(l+1)}} K_{ijk}u_i n_j\, dS_y = \\
&\quad -\int_{V^{(l-1)}} \tilde{\tau}_{ij}^{(l-1)}\partial_j^y J_{ik}\, d\boldsymbol{y} - \int_{V^{(l)}} \tilde{\tau}_{ij}^{(l)}\partial_j^y J_{ik}\, d\boldsymbol{y} - \\
&\quad \int_{S^{(l)}} J_{ik}q_i^{(l)}\, dS_y + \int_{S^{(l-1)}} J_{ik}\pi_{ij}^{(l-1)}n_j\, dS_y - \int_{S^{(l+1)}} J_{ik}\pi_{ij}^{(l)}n_j\, dS_y \quad (4\text{-}16)
\end{aligned}$$

where $\boldsymbol{x} \in S^{(l)}$. It is seen that this equation still contains the total stress tensor at the interfaces $S^{(l-1)}$ and $S^{(l+1)}$. To remove these integrals we consider the integral expression (4-15) for the velocity in the domain $V^{(l+b)}$, with b an integer. If we apply this integral expression in a point $\boldsymbol{x}$ which does *not* lie in $V^{(l+b)}$ or its boundaries (i.e. $\boldsymbol{x} \notin (S^{b+l} \cup V^{b+l} \cup S^{b+l+1})$, we obtain the following relation:

$$\begin{aligned}
&-\lambda^{(l+b)}\int_{S^{(l+b)}} K_{ijk}u_i n_j\, dS_y + \lambda^{(l+b)}\int_{S^{(l+1+b)}} K_{ijk}u_i n_j\, dS_y = \\
&\quad -\int_{V^{(l+b)}} \tilde{\tau}_{ij}^{(l+b)}\partial_j^y J_{ik}\, d\boldsymbol{y} + \int_{S^{(l+b)}} J_{ik}\pi_{ij}^{(l+b)}n_j\, dS_y - \int_{S^{(l+1+b)}} J_{ik}\pi_{ij}^{(l+b)}n_j\, dS_y.
\end{aligned}$$

By subsequently adding this expression to (4-16) for $b = 1, \ldots, K-l-1$ and $b = -1, \ldots, -l$ we finally obtain:

$$\begin{aligned}
&\frac{1}{2}(\lambda^{(l-1)}+\lambda^{(l)})u_k(\boldsymbol{x}) + \sum_{m=1}^{K}(\lambda^{(m-1)}-\lambda^{(m)})\int_{S^{(m)}} K_{ijk}u_i n_j\, dS_y = \\
&\quad u_k^{\infty}(\boldsymbol{x}) - \sum_{m=1}^{K}\left\{\int_{V^{(m)}} \tilde{\tau}_{ij}^{(m)}\partial_j^y J_{ik}\, d\boldsymbol{y} + \int_{S^{(m)}} J_{ik}q_i^{(m)}\, dS_y\right\}, \quad (4\text{-}17)
\end{aligned}$$

where $\boldsymbol{x} \in S^{(l)}$. Repeating this procedure if $\boldsymbol{x}$ lies within the domain $V^{(l)}$ we find the following expression:

$$\lambda^{(l)} u_k(\boldsymbol{x}) + \sum_{m=1}^{K} (\lambda^{(m-1)} - \lambda^{(m)}) \int_{S^{(m)}} K_{ijk} u_i n_j \, dS_y = u_k^{\infty}(\boldsymbol{x}) - \sum_{m=1}^{K} \left\{ \int_{V^{(m)}} \tilde{\tau}_{ij}^{(m)} \partial_j^y J_{ik} \, d\boldsymbol{y} + \int_{S^{(m)}} J_{ik} q_i^{(m)} \, dS_y \right\}. \quad (4\text{-}18)$$

With the expressions (4-17) and (4-18) we have represented the velocity field in terms of boundary and domain integrals containing the non-Newtonian stress tensor and the shape of the boundaries $S^{(l)}$. By calculating $\boldsymbol{u}$ and subsequently updating the interfaces through the equations (2-17) and the non-Newtonian stress tensor through a certain constitutive equation we simulate the evolution of both $S^{(l)}$ and $\tilde{\tau}_{ij}^{(l)}$.

For small values of $\lambda^{(l)}$, the numerical method sketched above leads to unacceptable numerical volume losses (De Bruijn [61], Manga [62]). The reason of these volume losses lies in the fact (4-17) has an infinite number of solutions for $\lambda = 0$ (Pozrikidis [44]). Besides $\lambda = 0$ the integral equation (4-17) also has an eigenvalue $\lambda = \infty$. To eliminate the volume losses at $\lambda = 0$ we redefine the non-Newtonian stress tensor according to (2-10). In this case, we obtain a simple expression which is valid in all the domains of our fluid problem:

$$u_k(\boldsymbol{x}) + \sum_{m=1}^{K} \int_{V^{(m)}} \tilde{\tau}_{ij}^{(m)} \partial_j^y J_{ik} \, d\boldsymbol{y} = u_k^{\infty}(\boldsymbol{x}) - \sum_{m=1}^{K} \int_{S^{(m)}} J_{ik} q_i^{(m)} \, dS_y, \quad (4\text{-}19)$$

where $\tilde{\tau}_{ij}^{(m)}$ is the extra stress tensor. It can be proven that the integral expressions are equivalent, but (4-19) has the advantage of resulting in smaller numerical volume losses for small viscosity ratios (Kuerten [63]). In some situations, e.g. axisymmetric flow, the numerical evaluation of the term $\partial_j J_{ik}$ can be very costly. A solution to this problem is obtained by repeating the derivation sketched in this section, but, without applying the Gauss divergence theorem to the integral expression (4-12). In this case we obtain:

$$u_k(\boldsymbol{x}) - \sum_{m=1}^{K} \int_{V^{(m)}} J_{ik} \partial_j \tilde{\tau}_{ij}^{(m)} \, d\boldsymbol{y} = u_k^{\infty}(\boldsymbol{x}) - \sum_{m=1}^{K} \int_{S^{(m)}} J_{ik} \tilde{q}_i^{(m)} \, dS_y, \quad (4\text{-}20)$$

with $\tilde{q}_i^{(m)}$ given by:

$$\tilde{q}_i^{(m)} = q_i^{(m)} + [\tilde{\tau}_{ij}]_{S^{(m)}} \, n_j^{(m)}. \quad (4\text{-}21)$$

It is seen that this expression does not contain the term $\partial_j J_{ik}$ which may reduce the computational effort significantly.

If we are considering a Newtonian drop, the formulation presented above is costly due to the presence of a domain integral, i.e. the extra stress tensor contains a viscous part. In this specific situation it is more appropriate to apply Wielandt eigenvalue deflation (Pozrikidis [44]). In this method, the kernel of the integral equation (4-17) is redefined such that the solution is unchanged but the eigenvalues $\lambda = 0$ and $\lambda = \infty$ are removed. Following Pozrikidis [44] and taking $K = 1$ for convenience, we find an integral equation for an ancillary solution $\boldsymbol{U}(\boldsymbol{x})$:

$$\frac{1}{2}(1+\lambda)U_k(\boldsymbol{x}) + (1-\lambda)\int_S K_{ijk}U_i n_j \, dS_y = -\frac{1-\lambda}{S_D} n_k(\boldsymbol{x}) \int_S U_i n_i \, dS_y$$
$$+\frac{1-\lambda}{S_D}\int_S U_k \, dS_y + (1-\lambda)\sum_{n=1}^{3} q_k^n(\boldsymbol{x}) \int_S U_i q_i^n \, dS_y + F_k(\boldsymbol{x}), \quad (4\text{-}22)$$

where $F_k(\boldsymbol{x})$ is a forcing function composed of the right-hand side of (4-17) and S_D is the total area of the drop surface S. The vector $\boldsymbol{q}^n$ is a normalized eigensolution for $\lambda = \infty$ expressing rigid body rotation:

$$\boldsymbol{q}^n(\boldsymbol{x}) = \frac{1}{C_D}\boldsymbol{\omega}_n \times (\boldsymbol{x} - \boldsymbol{x}^c), \quad n = 1, \ldots, 3,$$

where $\times$ denotes the cross product, $\boldsymbol{x}^c$ is the surface centroid of the drop, and C_D the normalization constant:

$$C_D = \left\{ \int_S |\boldsymbol{\omega}_n \times (\boldsymbol{x} - \boldsymbol{x}^c)|^2 \, dS_y \right\}^{1/2}.$$

The unit vectors $\boldsymbol{\omega}_n, \quad n = 1, \ldots, 3$ are chosen such that $\boldsymbol{q}^n$ satisfies:

$$\int_S q_i^n q_i^m \, dS = \delta_{nm}.$$

Note that the first integral on the right-hand side of (4-22) purges the eigensolution for $\lambda = 0$, the second integral removes the rigid body motion of the drop. This implies that for a sphere placed in the origin of an elongational flow, it suffices to deflate with respect to $\lambda = 0$. The velocity may be computed from the auxiliary function $\boldsymbol{U}(\boldsymbol{x})$ using:

$$u_k(\boldsymbol{x}) = U_k(\boldsymbol{x}) - \frac{1}{2}(1-\lambda)\left\{ \frac{1}{S_D}\int_S U_k \, dS_y + \sum_{n=1}^{3} q_k^n(\boldsymbol{x}) \int_S U_i q_i^n \, dS_y \right\}. \quad (4\text{-}23)$$

So instead of solving (4-17), we first solve (4-22) and then compute the velocity using (4-23) thus obtaining accurate values for the velocity for all values of the viscosity ratio λ.

In the next section, we transform the above integral equations to cylindrical coordinates and reduce the dimension of the problem for axisymmetric flow through an explicit integration over the azimuthal direction.

4.3 Axisymmetric compound drop

In this section, we consider an imposed flow $\boldsymbol{u}^\infty$ that is axisymmetric around the x_1 axis with no swirling motion. The initial shapes of all the interfaces are also assumed to be axisymmetric around the x_1 axis. By transforming the integral equations (4-19) or (4-20) to cylindrical coordinates and performing the integration over the azimuthal direction analytically we can reduce the dimension of the problem. As the procedure to transform equation (4-19) or (4-20) is very similar, we focus on (4-19). In subsection 4.3.1, we introduce cylindrical coordinates and perform the transformation of equation (4-19). In subsection 4.3.2, we discuss the analytical integration in the azimuthal direction for the boundary integral term and the volume integral term separately.

4.3.1 Green's functions in cylindrical coordinates

In this subsection the integral representation for an axisymmetric drop placed in an axisymmetric flow is derived. We use cylindrical coordinates defined by:

$$\begin{cases} x_1 &= \bar{x}_1 \\ x_2 &= \bar{x}_2 \cos(\bar{x}_3) \\ x_3 &= \bar{x}_2 \sin(\bar{x}_3), \end{cases} \tag{4-24}$$

where $\bar{x}_1$, $\bar{x}_2$ and $\bar{x}_3$ indicate the axial, radial and azimuthal coordinates respectively. Observe that we use $(\bar{x}_1, \bar{x}_2, \bar{x}_3)$ instead of the more common (x, r, ϕ) to permit the summation convention. In the sequel, we denote corresponding components with respect to cylindrical coordinates with an over-bar. Using these coordinates, we can describe the surface $S^{(l)}$ as the surface of revolution of:

$$\bar{x}_2 = R^{(l)}(\bar{x}_1) \quad \text{for} \quad z_1^{(l)} \leq \bar{x}_1 \leq z_2^{(l)}, \tag{4-25}$$

with $R^{(l)}(z_1^{(l)}) = R^{(l)}(z_2^{(l)}) = 0$, as shown in figure 4-1.

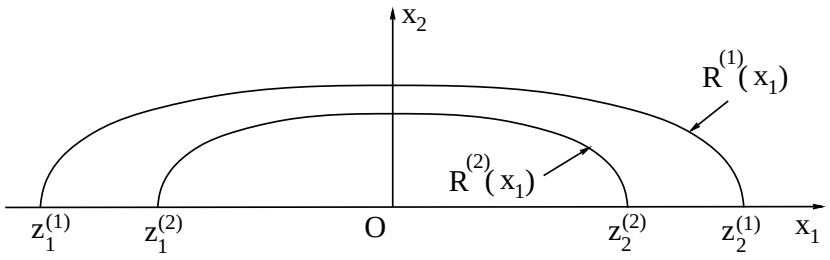

Figure 4-1: Schematic representation of an axisymmetric compound drop consisting of one layer and a core ($K = 2$).

In order to transform (4-19) to cylindrical coordinates, we need to know how a vector and a tensor field are transformed. We proceed with a number of steps closely following Bird et al. [34]. First, we introduce an orthonormal basis $\bar{\boldsymbol{e}}_1, \bar{\boldsymbol{e}}_2, \bar{\boldsymbol{e}}_3$ for cylindrical coordinates which is related to the Cartesian base $\boldsymbol{e}_1, \boldsymbol{e}_2, \boldsymbol{e}_3$ by:

$$\bar{\boldsymbol{e}}_1 = \boldsymbol{e}_1, \quad \bar{\boldsymbol{e}}_2 = \cos(\bar{x}_3)\boldsymbol{e}_2 + \sin(\bar{x}_3)\boldsymbol{e}_3, \quad \bar{\boldsymbol{e}}_3 = -\sin(\bar{x}_3)\boldsymbol{e}_2 + \cos(\bar{x}_3)\boldsymbol{e}_3.$$

Using an orthonormal basis a vector $\boldsymbol{u}$ can be represented as:

$$\boldsymbol{u} = u_k \boldsymbol{e}_k = \bar{u}_k \bar{\boldsymbol{e}}_k,$$

where the components u_k and $\bar{u}_k$ are also called the physical components of the vector $\boldsymbol{u}$ in the respective coordinate systems (Bird et al. [34]). To perform the transformation, it will be convenient to use a natural basis $\{\boldsymbol{g}_1, \boldsymbol{g}_2, \boldsymbol{g}_3\}$ for the coordinates $(\bar{x}_1, \bar{x}_2, \bar{x}_3)$ which is related to the orthonormal basis $\{\bar{\boldsymbol{e}}_1, \bar{\boldsymbol{e}}_2, \bar{\boldsymbol{e}}_3\}$ through:

$$\boldsymbol{g}_1 = \bar{\boldsymbol{e}}_1; \quad \boldsymbol{g}_2 = \bar{\boldsymbol{e}}_2; \quad \boldsymbol{g}_3 = \bar{x}_2 \bar{\boldsymbol{e}}_3. \tag{4-26}$$

Similarly, we can define a set of reciprocal basis vectors:

$$\boldsymbol{g}^1 = \bar{\boldsymbol{e}}_1; \quad \boldsymbol{g}^2 = \bar{\boldsymbol{e}}_2; \quad \boldsymbol{g}^3 = \frac{1}{\bar{x}_2} \bar{\boldsymbol{e}}_3. \tag{4-27}$$

A vector $\boldsymbol{u}$ can then be represented as:

$$\boldsymbol{u} = \bar{u}^\alpha \boldsymbol{g}_\alpha = \bar{u}_\alpha \boldsymbol{g}^\alpha, \tag{4-28}$$

in which $\bar{u}_\alpha$ and $\bar{u}^\alpha$ are the covariant and contravariant components of the vector $\boldsymbol{u}$. It is noted that $\bar{u}_\alpha$ and $\bar{u}^\alpha$ are different from the physical components introduced above. In (4-28) summation is performed over repeated lower and upper indices. In the following, we use the covariant representation for the velocity and stresses. Using (4-24) and (4-28), we find that the desired transformation of a velocity component u_i and a stress component τ_{ij} from cylindrical to Cartesian coordinates is given by:

$$u_i(\boldsymbol{x}) = \frac{\partial \bar{x}^\alpha}{\partial x^i}\bar{u}_\alpha(\bar{\boldsymbol{x}}); \quad \tau_{ij}(\boldsymbol{x}) = \frac{\partial \bar{x}^\alpha}{\partial x^i}\frac{\partial \bar{x}^\beta}{\partial x^j}\bar{\tau}_{\alpha\beta}(\bar{\boldsymbol{x}}), \tag{4-29}$$

respectively. Using these transformation formulas, we can rewrite (4-19) as:

$$\bar{u}_\alpha(\bar{\boldsymbol{x}}) = \bar{u}^\infty_\alpha(\bar{\boldsymbol{x}}) - \sum_{m=1}^{K}\int_{\bar{V}^{(m)}} \bar{U}^{\gamma\beta}{}_\alpha(\bar{\boldsymbol{x}};\bar{\boldsymbol{y}})\bar{\bar{\tau}}^{(m)}_{\beta\gamma}(\bar{\boldsymbol{y}})\,|Q(\bar{\boldsymbol{y}})|\,d\bar{\boldsymbol{y}} - \sum_{m=1}^{K}\int_{\bar{S}^{(m)}} \bar{J}^\beta{}_\alpha(\bar{\boldsymbol{x}};\bar{\boldsymbol{y}})\bar{q}^{(m)}_\beta(\bar{\boldsymbol{y}})\,d\bar{S}_y, \tag{4-30}$$

with $\bar{V}^{(m)}$ the m-th transformed internal domain, $\bar{S}^{(m)}$ the m-th transformed boundary and $|Q(\bar{\boldsymbol{y}})| = \bar{x}_2$ the Jacobian of the transformation. The kernels $\bar{U}^{\gamma\beta}{}_\alpha(\bar{\boldsymbol{x}};\bar{\boldsymbol{y}})$ and $\bar{J}^\beta{}_\alpha(\bar{\boldsymbol{x}};\bar{\boldsymbol{y}})$ are given by:

$$\bar{U}^{\gamma\beta}{}_\alpha(\bar{\boldsymbol{x}};\bar{\boldsymbol{y}}) = \frac{\partial x^k}{\partial \bar{x}^\alpha}\frac{\partial \bar{y}^\beta}{\partial y^i}\frac{\partial \bar{y}^\gamma}{\partial y^j}\partial^y_j J_{ik}(\bar{\boldsymbol{x}} - \bar{\boldsymbol{y}}) \tag{4-31}$$

$$\bar{J}^\beta{}_\alpha(\bar{\boldsymbol{x}};\bar{\boldsymbol{y}}) = \frac{\partial x^k}{\partial \bar{x}^\alpha}\frac{\partial \bar{y}^\beta}{\partial y^i}J_{ik}(\bar{\boldsymbol{x}} - \bar{\boldsymbol{y}}), \tag{4-32}$$

where we have expressed the Green's function J_{ik} in cylindrical coordinates by using the transformation formulas in (4-24). Expression (4-30) is the integral representation for the velocity in cylindrical coordinates and the kernels $\bar{J}^\beta{}_\alpha(\bar{\boldsymbol{x}};\bar{\boldsymbol{y}})$ and $\bar{U}^{\gamma\beta}{}_\alpha(\bar{\boldsymbol{x}};\bar{\boldsymbol{y}})$ are the corresponding Green's functions.

4.3.2 Integral formulation for axisymmetric flow

In this subsection, the integral equation (4-30) is simplified by performing the integration in the azimuthal direction analytically. First, we study the integral equation of a Newtonian drop in an axisymmetric flow. Noting that the azimuthal component of the unit normal vector is zero and the curvature

is independent of the azimuthal coordinate, we can write the velocity as:

$$\bar{u}_\alpha(\bar{\boldsymbol{x}}) = \bar{u}^\infty_\alpha(\bar{\boldsymbol{x}}) - \sum_{m=1}^{K} \int_{L^{(m)}} \bar{q}^{(m)}_\beta(\bar{y}_1) R^{(m)}(\bar{y}_1) \int_0^{2\pi} \bar{J}^\beta{}_\alpha(\bar{\boldsymbol{x}};\bar{\boldsymbol{y}})\, d\bar{y}_3\, dl_y, \quad (4\text{-}33)$$

where $L^{(m)}$ is the intersection of the surface described by $\bar{x}_2 = R^{(m)}(\bar{x}_1)$ and the plane $\bar{x}_3 = 0$, and $R^{(m)}(\bar{y}_1) d\bar{y}_3 dl_y$ is the unit surface area with $dl_y = \{1 + (\partial_{\bar{y}_1} R^{(m)}(\bar{y}_1))^2\}^{1/2}\, d\bar{y}_1$. The integral in the ϕ direction is given by:

$$\bar{M}^\beta{}_\alpha(\bar{\boldsymbol{x}};\bar{y}_1,\bar{y}_2) = \int_0^{2\pi} \bar{J}^\beta{}_\alpha(\bar{\boldsymbol{x}};\bar{\boldsymbol{y}})\, d\bar{y}_3. \quad (4\text{-}34)$$

Using the expression for the Green's function (4-32) and the transformation formulas in (4-24), we can express $\bar{M}^\beta{}_\alpha(\bar{\boldsymbol{x}};\bar{y}_1,\bar{y}_2)$ in terms of complete elliptic integrals of the first and second kind [64] (see Appendix A). These integrals can be computed with an iterative method. Since the constitutive equation for a Newtonian fluid obeys material frame invariance (translational and rotational invariance), the resulting flow is axisymmetric when the drop interfaces $V^{(m)}$ and $\boldsymbol{u}^\infty$ are axisymmetric (Schowalter [65]). Since the external velocity field has no swirling motion $\bar{u}_3(\bar{\boldsymbol{x}})$ is zero. This property also follows directly from equation (4-33), since $\bar{M}^\beta{}_\alpha(\bar{\boldsymbol{x}};\bar{y}_1,\bar{y}_2)$ obeys (Toose [46]):

$$\bar{M}^\beta{}_3 \bar{n}_\beta = \bar{M}^3{}_3 \bar{n}_3 = 0,$$

which implies that the contribution of the boundary integral to the azimuthal component of the velocity is zero. Using this, we can rewrite (4-33) as:

$$\bar{u}_\alpha(\bar{\boldsymbol{x}}) = \bar{u}^\infty_\alpha(\bar{\boldsymbol{x}}) - \sum_{m=1}^{K} \int_{L^{(m)}} \bar{q}^{(m)}_\beta(\bar{y}_1) \bar{M}^\beta{}_\alpha(\bar{\boldsymbol{x}};\bar{y}_1,\bar{y}_2) R^{(m)}(\bar{y}_1)\, dl_y, \quad \alpha = 1,2\ . \quad (4\text{-}35)$$

Hence, for the Newtonian drop the main problem is reduced to the evaluation of a one-dimensional integral.

In the case of a non-Newtonian drop, the contribution of the non-Newtonian stress tensor to the velocity is given by:

$$\begin{aligned} I_\alpha &= \sum_{m=1}^{K} \int_{\bar{V}^{(m)}} \bar{U}^{\gamma\beta}{}_\alpha(\bar{\boldsymbol{x}};\bar{\boldsymbol{y}}) \bar{\bar{\tau}}^{(m)}_{\beta\gamma}(\bar{\boldsymbol{y}})\, |Q(\bar{\boldsymbol{y}})|\, d\bar{\boldsymbol{y}} \\ &= \sum_{m=1}^{K} \int_{\bar{V}^{(m)}} \bar{U}^{\gamma\beta}{}_\alpha(\bar{\boldsymbol{x}};\bar{\boldsymbol{y}}) \bar{\bar{\tau}}^{(m)}_{\beta\gamma}(\bar{\boldsymbol{y}}) \bar{y}_2\, d\bar{y}_3\, d\bar{y}_2\, d\bar{y}_1. \end{aligned} \quad (4\text{-}36)$$

To perform the integration in the azimuthal direction analytically, we assume that the non-Newtonian stress tensor satisfies the following conditions:

$$\begin{aligned} &1.\ \bar{\bar{\tau}}^{(m)}_{\beta\gamma}(\bar{\boldsymbol{y}}) = \bar{\bar{\tau}}^{(m)}_{\gamma\beta}(\bar{\boldsymbol{y}}) \text{ (symmetric)} \\ &2.\ \bar{\bar{\tau}}^{(m)}_{13}(\bar{\boldsymbol{y}}) = \bar{\bar{\tau}}^{(m)}_{23}(\bar{\boldsymbol{y}}) = 0 \\ &3.\ \bar{\bar{\tau}}^{(m)}_{\beta\gamma}(\bar{\boldsymbol{y}}) \text{ is independent of } \bar{x}_3. \end{aligned} \tag{4-37}$$

The physical interpretation of these conditions is as follows. The first condition implies that no electric or magnetic dipoles are present. The second condition states that the constitutive equation for the non-Newtonian stress tensor obeys material frame invariance. From the last condition it follows that the non-Newtonian fluid must be isotropic. These conditions also imply that the non-Newtonian stress tensor has no contribution to the azimuthal velocity component for axisymmetric flow. Analyzing the constitutive equations presented in chapter 3, we find that all models introduced satisfy these conditions. Hence, we can rewrite (4-36) as:

$$I_\alpha = \sum_{m=1}^{K} \int_{\bar{A}^{(m)}} \bar{\bar{\tau}}^{(m)}_{\beta\gamma}(\bar{y}_1, \bar{y}_2) \bar{W}^{\gamma\beta}{}_{\alpha}(\bar{\boldsymbol{x}}; \bar{y}_1, \bar{y}_2) \bar{y}_2 \, d\bar{y}_2 \, d\bar{y}_1, \tag{4-38}$$

where $\bar{A}^{(m)}$ is the part of the plane $\bar{x}_3 = 0$ which is contained in $\bar{V}^{(m)}$, (see figure 4-1). The kernel $\bar{W}^{\gamma\beta}{}_{\alpha}(\bar{\boldsymbol{x}}; \bar{y}_1, \bar{y}_2)$ is given by:

$$\bar{W}^{\gamma\beta}{}_{\alpha}(\bar{\boldsymbol{x}}, \bar{y}_1, \bar{y}_2) = \int_0^{2\pi} \bar{U}^{\gamma\beta}{}_{\alpha}(\bar{\boldsymbol{x}}; \bar{\boldsymbol{y}}) \, d\bar{y}_3, \tag{4-39}$$

which can be expressed in terms of complete elliptic integrals of the first and second kind with the use of the expression for the Green's function (4-31) and the transformation formulas in (4-24) (Toose [46]). Using the expressions for (4-39) as given in the appendix A, we find that $\bar{W}^{\gamma\beta}{}_{\alpha}(\bar{\boldsymbol{x}}, \bar{y}_1, \bar{y}_2)$ obeys:

$$\bar{\bar{\tau}}_{\beta\gamma} \bar{W}^{\gamma\beta}{}_{3} = 0, \tag{4-40}$$

which implies that $I_3 = 0$. This confirms that the non-Newtonian stress tensor gives no contribution to the velocity in the azimuthal direction for axisymmetric flow. Combining (4-35) and (4-40), we obtain the following

expression for the velocity field:

$$\begin{cases} \bar{u}_\alpha(\bar{\boldsymbol{x}}) = \bar{u}^\infty_\alpha(\bar{\boldsymbol{x}}) - \displaystyle\sum_{m=1}^{K} \int_{\bar{A}^{(m)}} \bar{\bar{\tau}}^{(m)}_{\beta\gamma}(\bar{y}_1,\bar{y}_2)\bar{W}^{\gamma\beta}{}_\alpha(\bar{\boldsymbol{x}};\bar{y}_1,\bar{y}_2)\bar{y}_2\, d\bar{y}_2\, d\bar{y}_1 \\ \qquad\qquad - \displaystyle\sum_{m=1}^{K} \int_{L^{(m)}} \bar{q}^{(m)}_\beta(\bar{y}_1)\bar{M}^\beta{}_\alpha(\bar{\boldsymbol{x}};\bar{y}_1,\bar{y}_2)R^m(\bar{y}_1)\, dl_y, \quad \alpha = 1,2 \\ \bar{u}_3(\bar{\boldsymbol{x}}) = 0, \end{cases} \tag{4-41}$$

which involves surface integral. With expression (4-41) we have reduced the three-dimensional problem to a two-dimensional one. Reduction of the problem to one dimension, as for Newtonian drops, requires the transformation of the domain to a set of boundary integrals using a dual reciprocity method (Patridge et al. [66]). In this thesis, however, we choose to evaluate the domain integrals in the integral expression for the velocity directly. This implies that the computational effort required to solve non-Newtonian problems is considerably larger than for the corresponding Newtonian problems.

The numerical evaluation of the transformed Green's function $\bar{W}^{\gamma\beta}{}_\alpha$, requires a large amount of computational effort. By taking the integral expression (4-20) as a starting point and repeating the procedure outlined in the last two subsections, we obtain the following integral equation (Toose et al. [67]):

$$\bar{u}_\alpha(\bar{\boldsymbol{x}}) = \bar{u}^\infty_\alpha(\bar{\boldsymbol{x}}) + \sum_{m=1}^{K} \int_{\bar{A}^{(m)}} M^\beta{}_\alpha(\bar{\boldsymbol{x}};\bar{y}_1,\bar{y}_2)\bar{\partial}_\gamma \bar{\bar{\tau}}^{(m)}_{\beta\gamma}(\bar{\boldsymbol{y}})\bar{y}_2\, d\bar{y}_2 d\bar{y}_1 + \sum_{m=1}^{K} \int_{L^{(m)}} M^\beta{}_\alpha(\bar{\boldsymbol{x}};\bar{y}_1,\bar{y}_2)\bar{\bar{q}}^{(m)}_\beta(\bar{\boldsymbol{y}})R^{(m)}(\bar{y}_1)\, dl_y \tag{4-42}$$

where $\bar{\partial}_\gamma \bar{\bar{\tau}}^{(m)}_{\beta\gamma}(\bar{\boldsymbol{y}})$ denotes the divergence of the extra stress tensor in cylindrical coordinates which is defined as:

$$\bar{\partial}_\beta \bar{\bar{\tau}}^{(m)}_{\beta\gamma}(\bar{\boldsymbol{y}}) = g^{\alpha\beta}\left(\partial_\alpha \bar{\bar{\tau}}^{(m)}_{\beta\gamma} - \left\{ \begin{matrix} \lambda \\ \beta\ \alpha \end{matrix} \right\} \bar{\bar{\tau}}^{(m)}_{\lambda\gamma} - \left\{ \begin{matrix} \lambda \\ \gamma\ \alpha \end{matrix} \right\} \bar{\bar{\tau}}^{(m)}_{\beta\lambda}\right),$$

where the coefficients $\left\{ \begin{matrix} \lambda \\ \beta\ \alpha \end{matrix} \right\}$ are the Christoffel symbols of the first kind and $g^{\alpha\beta}$ is the contravariant metric tensor of the transformation (Bird et al. [34]). The integral expression (4-42) is numerically less costly to evaluate than (4-41).

4.4 Periodic dispersion of drops

In this section, we derive the integral formulation for a two-dimensional periodic suspension of Newtonian drops as was described in section 2.1. Assuming that all drops have the same viscosity and only one interface we, construct the solution for the velocity for the inner domain $V_l^{(1)}$ of the l-th drop through:

$$c_{ik}^{(1)}\lambda_l^{(1)}u_i(\boldsymbol{x}) - \lambda_l^{(1)}\int_{S_l^{(1)}} K_{ijk}(\boldsymbol{r})u_i(\boldsymbol{y})n_j(\boldsymbol{y})\,dS_y = \int_{S_l^{(1)}} J_{ik}(\boldsymbol{r})\tau_{ij}^{(1)}(\boldsymbol{y})n_j(\boldsymbol{y})\,dS_y, \quad l = 1,\dots,N. \tag{4-43}$$

The velocity in the outer domain $V^{(0)}$ is represented by:

$$c_{ik}^{(0)}u_i(\boldsymbol{x}) + \sum_{l=1}^{N}\int_{S_l^{(1)}} K_{ijk}(\boldsymbol{r})u_i(\boldsymbol{y})n_j(\boldsymbol{y})\,dS_y = u_k^{\infty}(\boldsymbol{x}) - \sum_{l=1}^{N}\int_{S_l^{(1)}} J_{ik}\tau_{ij}^{(1)}(\boldsymbol{y})n_j(\boldsymbol{y})\,dS_y, \tag{4-44}$$

where we have used the boundary condition (2-14) at infinity to perform the integrations over $S^{(0)}$. Adding (4-43) to (4-44) and applying the matching conditions we obtain the following expression for the velocity on $S_m^{(1)}$:

$$\frac{1}{2}(1+\lambda_m^{(1)})u_i(\boldsymbol{x}) - (1-\lambda_m^{(1)})\int_{S_l^{(1)}} K_{ijk}(\boldsymbol{r})u_i(\boldsymbol{y})n_j(\boldsymbol{y})\,dS_y + \sum_{\substack{l=1\\ l\neq m}}^{N}\int_{S_l^{(1)}} K_{ijk}u_i n_j\,dS_y = u_k^{\infty}(\boldsymbol{x}) - \int_{S_m^{(1)}} J_{ik}(\boldsymbol{r})q_i - \sum_{\substack{l=1\\ l\neq m}}^{N}\int_{S_l^{(1)}} J_{ik}\tau_{ij}^{(1)}n_j\,dS_y,\,dS_y \tag{4-45}$$

Eliminating the unknown viscous stress tensors at the interfaces of the drops using a similar technique as described in section (4.2), we find the following expression for the velocity on $S_m^{(1)}$:

$$\frac{1}{2}(1+\lambda_m^{(1)})u_k(\boldsymbol{x}) + \sum_{l=1}^{N}(1-\lambda_l^{(1)})\int_{S_l^{(1)}} K_{ijk}(\boldsymbol{r})u_i(\boldsymbol{y})n_j(\boldsymbol{y})\,dS_y = u_k^{\infty}(\boldsymbol{x}) - \sum_{l=1}^{N}\int_{S_l^{(1)}} J_{ik}(\boldsymbol{r})q_i(\boldsymbol{y})\,dS_y, \quad \boldsymbol{x}\in S_m^{(1)}$$

For convenience, we drop the superscripts on all variables in the remainder of this section. The expression above describes the velocity field of a finite set of drops in an infinite fluid domain. To describe the velocity field within a periodic dispersion, we should not only integrate over the interfaces $S_l,\ l = 1,\dots,N$ within one periodic cluster, but also over all other replicas of the interface S_l:

$$\frac{1}{2}(1+\lambda_m)u_k(\boldsymbol{x}) + \sum_{\mathbf{m}}\sum_{l=1}^{N}(1-\lambda_l)\int_{S_l^{[\mathbf{m}]}} K_{ijk}(\boldsymbol{r})u_i(\boldsymbol{y})n_j(\boldsymbol{y})\,dS_y = u_k^{\infty}(\boldsymbol{x}) - \sum_{\mathbf{m}}\sum_{l=1}^{N}\int_{S_l^{[\mathbf{m}]}} J_{ik}q_i\,dS_y, \tag{4-46}$$

where $S_l^{[\mathbf{m}]}$ denotes the interface of the drops in the $\mathbf{m}$-th periodic cluster ($\mathbf{m} = (m_1, m_2)$) and the summation is performed over the interfaces $S_l^{[\mathbf{0}]},\ l = 1,\dots,N$ and all their images. With this expression, we have found the velocity field due to a periodic dispersion of drops. Due to the summation over all the periodic clusters, this expression is not useful in numerical simulations. To overcome this problem we rewrite (4-46) such that the summation concerns the Green's functions only, which makes it relatively easy to perform the summation.

To perform this reformulation, we introduce the following coordinate transformation:

$$\boldsymbol{y} = \boldsymbol{z} + \boldsymbol{Y}^{[\mathbf{m}]}, \tag{4-47}$$

where $\boldsymbol{z}$ denotes a point lying in the original periodic box and $\boldsymbol{Y}^{[\mathbf{m}]}$ is the lattice vector which is given by:

$$\boldsymbol{Y}^{[\mathbf{m}]} = m_1\boldsymbol{a} + m_2\boldsymbol{b}, \quad \text{with } m_1, m_2 \in \mathbb{Z}. \tag{4-48}$$

Using this transformation and noting that the normal vector and curvature of an interface and the surface force $\boldsymbol{q}$ are periodic and hence independent of $\mathbf{m}$

one can rewrite the integral on the right hand side of (4-46) as:

$$\begin{aligned}
&\sum_{\mathbf{m}}\sum_{l=1}^{N}\int_{S_l^{[\mathbf{m}]}} J_{ik}(\boldsymbol{r})q_i(\boldsymbol{y})\,dS_y \\
&\quad=\sum_{\mathbf{m}}\sum_{l=1}^{N}\int_{S_l^{[\mathbf{0}]}} J_{ik}(\boldsymbol{x}-\boldsymbol{z}-\boldsymbol{Y}^{[\mathbf{m}]})q_i(\boldsymbol{z}+\boldsymbol{Y}^{\mathbf{m}})\,dS_z \\
&\quad=\sum_{l=1}^{N}\int_{S_l^{[\mathbf{0}]}}\left\{\sum_{\mathbf{m}} J_{ik}(\boldsymbol{r}^{[\mathbf{m}]})\right\}q_i(\boldsymbol{z})\,dS_z, \qquad (4\text{-}49)
\end{aligned}$$

with $\boldsymbol{r}^{[\mathbf{m}]}=\boldsymbol{x}-\boldsymbol{z}-\boldsymbol{Y}^{[\mathbf{m}]}$. To reformulate the integral on the left hand side of (4-46), we note that since $\boldsymbol{u}^{\infty}$ is a linear flow field, we can rewrite the velocity in the $\mathbf{m}$-th periodic cluster as:

$$\boldsymbol{u}(\boldsymbol{y})=\boldsymbol{u}(\boldsymbol{z}+\boldsymbol{Y}^{[\mathbf{m}]})=\boldsymbol{u}(\boldsymbol{z})+\boldsymbol{u}^{\infty}(\boldsymbol{Y}^{[\mathbf{m}]}),$$

Using this representation of the velocity, we obtain the following integral:

$$\begin{aligned}
&\sum_{\mathbf{m}}\sum_{l=1}^{N}(1-\lambda_l)\int_{S_l^{[\mathbf{m}]}} K_{ijk}(\boldsymbol{r})u_i(\boldsymbol{y})n_j(\boldsymbol{y})\,dS_y \\
&\quad=\sum_{\mathbf{m}}\sum_{l=1}^{N}(1-\lambda_l)\int_{S_l^{[\mathbf{0}]}} K_{ijk}(\boldsymbol{r}^{[\mathbf{m}]})\left\{u_i(\boldsymbol{z})+u_i^{\infty}(\boldsymbol{Y}^{[\mathbf{m}]})\right\}n_j(\boldsymbol{z})\,dS_z \\
&\quad=\sum_{l=1}^{N}(1-\lambda_l)\int_{S_l^{[\mathbf{0}]}}\left\{\sum_{\mathbf{m}} K_{ijk}(\boldsymbol{r}^{[\mathbf{m}]})\right\}u_i(\boldsymbol{z})n_j(\boldsymbol{z})\,dS_z, \qquad (4\text{-}50)
\end{aligned}$$

where we have used the relation:

$$\int_{S^{[\mathbf{0}]}} K_{ijk}(\boldsymbol{r}^{[\mathbf{m}]})n_j(\boldsymbol{z})dS_z=0 \quad \text{if } \mathbf{m}\neq 0 \qquad (4\text{-}51)$$

and the fact that $u^{\infty}(\boldsymbol{Y}^{[0]})=0$. Combining the expressions (4-46), (4-49) and (4-50), we finally find the following expression for the velocity at $S_m^{[0]}$:

$$\begin{aligned}
&\frac{1}{2}(1+\lambda_m)u_k(\boldsymbol{x})+\sum_{l=1}^{N}(1-\lambda_l)\int_{S_l^{[\mathbf{0}]}} K_{ijk}^{P}(\boldsymbol{r})u_i(\boldsymbol{y})n_j(\boldsymbol{y})\,dS_y= \\
&\quad u_k^{\infty}(\boldsymbol{x})-\sum_{l=1}^{N}\int_{S_l^{[\mathbf{0}]}}\left\{J_{ik}^{P}(\boldsymbol{r})\right\}q_i(\boldsymbol{y})\,dS_y, \qquad (4\text{-}52)
\end{aligned}$$

where we have replaced $\boldsymbol{z}$ by $\boldsymbol{y}$ for reasons of convenience. In this expression $J^P_{ik}(\boldsymbol{r})$ and $K^P_{ijk}(\boldsymbol{r})$ are the periodic Green's functions which are given by:

$$J^P_{ik}(\boldsymbol{r}) = \sum_{\mathbf{m}} J_{ik}(\boldsymbol{r}^{[\mathbf{m}]}), \quad K^P_{ijk}(\boldsymbol{r}) = \sum_{\mathbf{m}} K_{ijk}(\boldsymbol{r}^{[\mathbf{m}]}). \tag{4-53}$$

With (4-52) we obtained an expression for the velocity which only requires the integration over the interfaces in one periodic cell using periodic Green's functions. The divergence of the sum in the expression for J^P_{ik} makes numerical computation impossible. To circumvent this problem we first express the periodic Green's functions in terms of Fourier series, which makes the sum applicable for numerical evaluation.

To express the periodic Green's functions in Fourier series we solve a periodic singular Stokes problem (Hasimoto [68]):

$$\partial_{jj} J^P_{ik} - \partial_i p^P_k = -\delta_{ik} \sum_{\mathbf{m}} \delta_2(\boldsymbol{r}^{[\mathbf{m}]}) \ , \quad \partial_j J^P_{jk}(\boldsymbol{x}) = 0, \tag{4-54}$$

where δ_2 is the two-dimensional delta function. Exploiting the periodicity of the flow, the functions J^P_{ik} and p^P_k can be expanded in Fourier series. Substitution of these Fourier series in (4-54) we find an algebraic system of equations for the Fourier coefficients. Solving this system of equations we obtain a formulation of J^P_{ik} in terms of Fourier series:

$$J^P_{ik}(\boldsymbol{r}) = \frac{4\pi}{A} {\sum_{\mathbf{m}}}' \frac{1}{|\boldsymbol{l}^{[\mathbf{m}]}|^2} \left(\delta_{ik} - \frac{l^{[\mathbf{m}]}_i l^{[\mathbf{m}]}_k}{|\boldsymbol{l}^{[\mathbf{m}]}|^2} \right) \exp\left(-I r_j l^{[\mathbf{m}]}_j \right), \tag{4-55}$$

where the prime indicates that $\boldsymbol{m} = \mathbf{0}$ is excluded from the summation, I denotes the imaginary unit, A the area of the periodic cell and $\boldsymbol{l}^{[\mathbf{m}]}$ is a vector in the reciprocal lattice space:

$$\boldsymbol{l}^{[\mathbf{m}]} = m_1 \boldsymbol{a}^* + m_2 \boldsymbol{b}^*, \quad \boldsymbol{m} \in [\mathbb{Z} \times \mathbb{Z}].$$

The vectors $\boldsymbol{a}^*$ and $\boldsymbol{b}^*$ are the basis vectors of the reciprocal lattice cell which are defined as

$$\boldsymbol{b}^* = \frac{2\pi}{A} \boldsymbol{a} \times \boldsymbol{e}_z \ , \quad \boldsymbol{b}^* = \frac{2\pi}{A} \boldsymbol{e}_z \times \boldsymbol{b},$$

where $\times$ denotes the crossproduct. An expression for the stress tensor K^P_{ijk} can be derived in an analogous way. Having expressed the periodic Green's functions in terms of Fourier series, we now turn to the acceleration of the summations.

To accelerate the convergence of the summations, we explore an alternative formulation based on the Ewald summation technique (Hasimoto [68]), which involves the splitting of the slowly converging sums in two faster converging sums: One part is summed in physical space and the other part in reciprocal space. This accelerated summation method leads to the following formulation of the periodic Green's function J_{ik}^P:

$$J_{ik}^P(\boldsymbol{r}) = \sum_{\mathbf{m}} \left\{ \delta_{ik} \frac{1}{2} E_1(\xi^2 |\boldsymbol{r}^{[\mathbf{m}]}|^2) + \left(\frac{r_i^{[m]} r_k^{[\mathbf{m}]}}{|\boldsymbol{r}^{[\mathbf{m}]}|^2} - \delta_{ik} \right) \exp\left(-\xi^2 |\boldsymbol{r}^{[\mathbf{m}]}|^2 \right) \right\} +$$
$$\frac{4\pi}{A} \sum_{\mathbf{m}}{}' \left\{ \left(\frac{1}{|\boldsymbol{l}^{[\mathbf{m}]}|^2} + \frac{1}{4\xi^2} \right) \left(\delta_{ik} - \frac{l_i^{[\mathbf{m}]} l_k^{[\mathbf{m}]}}{|\boldsymbol{l}^{[\mathbf{m}]}|^2} \right) \exp\left(-\frac{|\boldsymbol{l}^{[\mathbf{m}]}|^2}{4\xi^2} \right) \cos\left(\boldsymbol{r} \cdot \boldsymbol{l}^{[\mathbf{m}]} \right) \right\},$$

where $E_1(x)$ is given by:

$$E_1(x) = \int_1^\infty e^{-xt} t^{-1} dt. \tag{4-56}$$

The final result for K_{ijk}^P follows similarly and is given explicitly by Van de Vorst [69]. The parameter ξ can be chosen freely and allows some control over the convergence rate of the two sums: An increasing value of ξ leads to an increase in the convergence rate of the sum in the physical space and a decrease of the convergence rate of the sum in reciprocal space. Ideally, this parameter ξ should be chosen such that both sums converge at equal rates. Following Van de Vorst [69], this is the case for

$$\xi = \sqrt{\frac{\pi}{A}}. \tag{4-57}$$

Computations indicated that the convergence rates of the accelerated summation method is much increased compared with the equation (4-55).

With the integral expressions derived in this and the previous sections, we have expressed the solution for the velocity field in the entire flow domain in terms of boundary and domain integrals, which contain the non-Newtonian stress tensor and the shape of the interface explicitly. In the next chapter we describe a complete method for solving the full time-dependent problem and show how the different integral equations are incorporated in this method.

Chapter 5

Numerical methods

In this chapter the numerical methods used to evaluate the boundary and domain integrals, the non-Newtonian stress tensor and the evolution of all surfaces $S^{(l)},\ l = 1, \ldots, K$ are described in detail. In section 5.1 the complete simulation method for the evolution of a drop consisting of K concentric layers of (non-)Newtonian material, or the evolution of a dispersion of viscous drops is described. The description of the geometry is provided in subsection 5.2. The numerical method used to calculate the velocity field, i.e. the evaluation of the integral equation is provided in section 5.3. In this section, special attention is paid to the evaluation of the periodic Green's functions. Finally, the time integration of the evolution equations for the interfaces and the non-Newtonian stress tensor is presented in section 5.4. For reasons of convenience the notation of the different domains, interfaces and variables is based on the case of an axisymmetric compound drop.

5.1 General simulation method

In this section the general scheme to simulate the time evolution of a single compound drop or a periodic dispersion of drops is given. This general scheme consists of an initialization part, i.e. imposing the initial conditions, and a time stepping part with which the actual evolution in time is generated. The details concerning the initialization are discussed first.

For a compound drop, we center the different layers around the origin of the coordinate system. For a periodic dispersion of two-dimensional drops, we form a periodic cluster by randomly placing N drops within a periodic box, enclosed by the lattice vectors $\boldsymbol{a}$ and $\boldsymbol{b}$. Subsequently a set of discrete collocation points is introduced in the internal domains $\bar{V}^{(l)}$ and on the interfaces

$\bar{S}^{(l)}$. Using these discrete points we introduce boundary elements to describe the shape of the interfaces and internal grid cells covering the internal domains $\bar{V}^{(l)}$. The total number of collocation points in our problem is denoted by N_t; $N_p^{(l)}$ gives the number of collocation points lying on the l-th interface. In order to describe the motion of the drop, both the non-Newtonian stress and the velocity need to be specified at these collocation points. At the start of the simulation, the stress is given by its initial conditions; the velocity corresponding to this initial stress and geometry can consistently be calculated using the boundary integral formulation for the velocity.

The complete time stepping procedure used to simulate the evolution of a compound non-Newtonian drop or a periodic dispersion of drops can be sketched as follows (see also figure 5-1). Using the velocity given at time t and the evolution equation (2-17) we can calculate the new positions of the collocation points, and consequently the shape of the interfaces of the drop at $t + \Delta t$. Moreover, depending on the non-Newtonian model chosen, we either integrate (3-9) in time or evaluate (3-20) explicitly in order to obtain the non-Newtonian stress tensor at the new time level. With this new stress tensor and shape of the interfaces, a new velocity field at time level $t + \Delta t$ can be calculated using the integral formulation for the problem considered. At

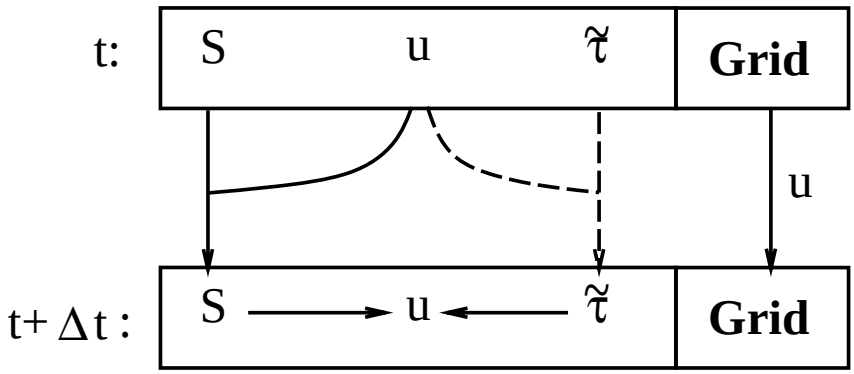

Figure 5-1: Schematic representation of the time stepping procedure used to simulate the evolution of a compound non-Newtonian drop or a periodic dispersion of drops

this point, all the elements which describe the state of the drop or dispersion, i.e. the collocation points describing the shapes of the interfaces, the velocity and the non-Newtonian stress at these points, have advanced one time step.

Repeating this explicit time integration procedure gives the evolution of the stress tensor, the velocity field, and the shape of all the boundaries $\bar{S}^{(l)}$.

After imposing the initial condition for the non-Newtonian stress and the interfaces and calculating the velocity field corresponding to this initial geometry and stress, the full algorithm can be summarized as follows:

1. update positions of the collocation points by integrating (2-17) over one time step to yield $\bar{S}^{(l)}(t+\Delta t),\ l=1,\dots,K$,
2. calculate the stress tensor at $t+\Delta t$ by solving (3-9) given $\bar{u}_\alpha$ at time t or by evaluating (3-20) using the new positions at time $t+\Delta t$
3. calculate the velocity field at $t+\Delta t$ given $\bar{\bar{\tau}}_{\beta\gamma}$ and $\bar{S}^{(l)}$ from step 1 and 2.

In the next four sections we discuss the representation of $S^{(l)}$ and $V^{(l)}$, the calculation of the velocity field, the evaluation of the periodic Green's functions, and the time integration of both the non-Newtonian stress tensor and the boundaries.

5.2 Geometry Description

The numerical evaluation of the integrals in (4-41) or (4-52) requires an accurate representation of the interfaces $\bar{S}^{(l)}$ by $N_b^{(l)}$ boundary elements and the subdivision of the internal domains $\bar{V}^{(l)}$ into $N_c^{(l)}$ internal cells. For convenience, we drop the superscript (l) whenever possible in this section.

Since the curvature of the interface is accurately required in order to calculate the surface force $\bar{\boldsymbol{q}}$, we use higher-order boundary elements to represent the interfaces. For the internal cells we adopt quadrilateral elements. In order to be able to use standard integration techniques for the calculation of the domain integral, we map these quadrilateral elements to a standard square element using a bilinear transformation (Farin [70]):

$$\bar{\boldsymbol{X}}(s_1,s_2)=\bar{\boldsymbol{A}}_1(1-s_1)(1-s_2)+\bar{\boldsymbol{A}}_2 s_1(1-s_2)+\bar{\boldsymbol{A}}_3 s_1 s_2+\bar{\boldsymbol{A}}_4(1-s_1)s_2, \tag{5-1}$$

where $\bar{\boldsymbol{A}}_1$, $\bar{\boldsymbol{A}}_2$, $\bar{\boldsymbol{A}}_3$ and $\bar{\boldsymbol{A}}_4$ are the vertices of the quadrilateral element and s_1 and s_2 are the local coordinates of the corresponding standard element. For the higher-order boundary elements we use piecewise C^2 cubic B-spline elements (DeBoor [71] and Farin [70]). The use of cubic B-spline elements

requires a suitable parameterization of the curve along the collocation points which is obtained with a chord length parameterization:

$$v[0] = 0$$
$$v[i] = v[i-1] + \|\bar{\boldsymbol{x}}_i - \bar{\boldsymbol{x}}_{i-1}\|, \quad i = 1, \ldots, N_p,$$

where $\bar{\boldsymbol{x}}_i$ is the i-th collocation point on the interface S. On this set of nodes, we introduce a cubic B-spline curve $\bar{\boldsymbol{s}}$ as (DeBoor [71]):

$$\bar{\boldsymbol{s}}(v) = \sum_{j=-3}^{N_p-1} \bar{\boldsymbol{d}}_j B_j(v), \tag{5-2}$$

where $B_j(v)$ is a cubic B-spline and $\left\{\bar{\boldsymbol{d}}_j\right\}$ are the control vertices of the B-spline curve such that $\bar{\boldsymbol{s}}(v[i]) = \bar{\boldsymbol{x}}_i$. It is noted that this interpolation problem can be fully specified if the (cyclic) symmetry of the drop is taken into account. The interpolation problem for $\bar{\boldsymbol{s}}(v)$ leads to a sparse matrix problem for $\left\{\bar{\boldsymbol{d}}_j\right\}$ which is solved using a band matrix solver.

From the control vertices $\left\{\bar{\boldsymbol{d}}_j\right\}$ we can calculate first and second order derivatives as well as points on the interface $\bar{S}$ using the DeBoor scheme (DeBoor [71]). The advantage of the DeBoor scheme is that we only use combinations of these control vertices, and do not have to evaluate the B-spline functions explicitly. From the first derivatives of the B-spline curve $\bar{\boldsymbol{s}}$ we can calculate the components of the normal vector using:

$$\bar{n}_1(v) = -\frac{1}{J}\partial_v \bar{s}_2, \quad \bar{n}_2(v) = \frac{1}{J}\partial_v \bar{s}_1,$$

where J is the differential arclength of the curve:

$$J(v) = \sqrt{(\partial_v \bar{s}_1)^2 + (\partial_v \bar{s}_2)^2} \tag{5-3}$$

The curvature $\bar{\partial}_\alpha \bar{n}_\alpha$ of the interface $\bar{S}$ of the drop is equal to the sum of the values of the curvatures in two arbitrary but mutually perpendicular directions. In case of an axisymmetric body described by cylindrical coordinates, it is most convenient to consider the curvatures in the meridional and azimuthal directions:

$$\bar{\partial}_\alpha \bar{n}_\alpha(v) = \frac{1}{(J)^2}\left\{\partial_{vv}\bar{s}_1 \bar{n}_1 - \partial_{vv}\bar{s}_2 \bar{n}_2\right\} + |\frac{\bar{n}_2}{\bar{s}_2}|,$$

where we have used a signed curvature [70] for the meridional direction. For two-dimensional drops, the last term on the right hand side of this expression is zero.

5.3 Calculation of the velocity

In this section, we discuss the numerical evaluation of the integral expressions introduced in chapter 4. In the first subsection, the evaluation of the integral expression for a compound non-Newtonian drop is discussed. The evaluation of the integral expression for a periodic dispersion of drops is described in subsection 5.3.2.

5.3.1 Axisymmetric compound drop

In order to calculate the velocity field we have to solve the integral equation (4-42) for the velocity at the collocation points. If viscosity ratios in the layers differ from unity we incorporate a part of the Newtonian stress in the non-Newtonian stress by redefining the non-Newtonian stress tensor as described in section 2.2. However, by this procedure the extra stress tensor becomes an explicit function of the velocity, which necessitates solving (4-42) iteratively at each time step. In this iteration, we assume a trial velocity field which is used to calculate the Newtonian part of the extra stress tensor. Application of (4-42) yields a new velocity field, which serves as the trial velocity field for the next iteration step. This iteration procedure is applied until the residual obtained after n iterations $\mathcal{R}^{(n)}$ is smaller than a pre-specified small number. The residual is defined as the discrete L_2 norm of the difference in the velocity at all collocation points in two successive iterations:

$$\mathcal{R}^{(n)} \equiv \left\{ \frac{1}{N_t} \sum_{i=1}^{N_t} |\bar{\boldsymbol{u}}_i^{(n)} - \bar{\boldsymbol{u}}_i^{(n-1)}|^2 \right\}^{1/2}, \tag{5-4}$$

where $\bar{\boldsymbol{u}}_i^{(n)}$ is the velocity after the n-th iteration level at the i-th collocation point. Computations show that the iteration process can safely be stopped if the residual is smaller than 10^{-6}: A further reduction of the residual does not affect the results. To reduce the required number of iterations, we set the initial trial velocity equal to the converged velocity obtained in the previous time step. When all viscosity ratios $\lambda^{(l)}$ are equal to unity the calculation reduces to a single step of this iteration procedure.

The velocity is computed at the collocation points, taken as the nodes of the B-spline curve for the interfaces and as the vertices of the internal cells, using the integral expression (4-42). With the discretization of the boundaries and internal domains described in the previous section, we can rewrite (4-42)

as:

$$\bar{u}_\alpha(\bar{\boldsymbol{x}}) \approx \bar{u}_\alpha^\infty(\bar{\boldsymbol{x}}) + \sum_{l=1}^{K}\sum_{m=1}^{N_b^{(l)}} \mathcal{I}_1(\bar{\boldsymbol{x}};\bar{S}_m^{(l)}) + \sum_{l=1}^{K}\sum_{m=1}^{N_c^{(l)}} \mathcal{I}_2(\bar{\boldsymbol{x}};\bar{V}_m^{(l)}) \tag{5-5}$$

where $\mathcal{I}_1(\bar{\boldsymbol{x}};\bar{S}_m^{(l)})$ and $\mathcal{I}_2(\bar{\boldsymbol{x}};\bar{V}_m^{(l)})$ are integrals over the m-th internal cell and the m-th boundary element corresponding to the l-th interface and layer respectively. Observe that $\mathcal{I}_2(\bar{\boldsymbol{x}};\bar{V}_m^{(l)}) = 0$ when the l-th layer consists of a Newtonian fluid and $\lambda^{(l)} = 1$. As the method to calculate the domain and interface integrals differ, we discuss both contributions separately, starting with the interface integral.

Using the spline curve $\bar{\boldsymbol{s}}^{(l)}$ representation of the interface $\bar{S}^{(l)}$, we can rewrite $\mathcal{I}_2(\bar{\boldsymbol{x}};\bar{S}_m^{(l)})$ as:

$$\begin{aligned}\mathcal{I}_1(\bar{\boldsymbol{x}};\bar{S}_m^{(l)}) &= \int_{\bar{S}_m^{(l)}} M^\beta{}_\alpha(\bar{\boldsymbol{r}})\bar{n}_\beta^{(l)}(\bar{\boldsymbol{y}})\bar{y}_2\, d\ell_y \\ &= \int_{v^{(l)}[m]}^{v^{(l)}[m+1]} M^\beta{}_\alpha(\bar{\boldsymbol{r}})\bar{n}_\beta^{(l)}(v)\bar{s}_2^{(l)}(v)J^{(l)}(v)\, dv.\end{aligned}$$

The Green's function $M^\beta{}_\alpha(\bar{\boldsymbol{r}})$ contains a logarithmic singularity as $\bar{\boldsymbol{r}}$ tends to zero. This implies that $\mathcal{I}_1(\bar{\boldsymbol{x}};\bar{S}_m^{(l)})$ involves a singular integrand if $\bar{\boldsymbol{x}}$ is located within the integration interval $\bar{S}_m^{(l)}$. A standard procedure used in literature is to distinguish between regular and singular contributions (Toose et al. [46]). For the regular part, a standard quadrature rule is used, whereas the singular contributions are treated in a special manner. In the approach adopted here we remove the singularity in the integrand in a uniform way which does not require a distinction between regular and singular contributions. By using the quadratic transformation (Telles [72]):

$$v(\omega) = a\omega^2 + b\omega + c. \tag{5-6}$$

The constants a, b and c in (5-6) are determined such that the following conditions are met:

$$v(-1) = v^{(l)}[m], \quad v(1) = v^{(l)}[m+1], \quad \left.\frac{\partial v}{\partial \omega}\right|_{\tilde{v}^{(l)}} = 0.$$

where $\tilde{v}^{(l)}$ is defined as the position at which $\|\bar{\boldsymbol{x}} - \bar{\boldsymbol{s}}^{(l)}(\tilde{v}^{(l)})\|$ is minimal. Applying the transformation (5-6) leads to:

$$\mathcal{I}_1(\bar{\boldsymbol{x}};\bar{S}_m^{(l)}) = \int_{-1}^{1} M^\beta{}_\alpha(\bar{\boldsymbol{r}})\bar{n}_\beta^{(l)}(v(\omega))\bar{s}_2^{(l)}(v(\omega))J^{(l)}(v(\omega))\partial_\omega v\, d\omega. \tag{5-7}$$

It is noted that the Jacobian $\partial_\omega v$ removes the singularity or quasi-singularity if $\bar{\boldsymbol{x}}$ is located either in or outside the integration interval. The removal of the quasi-singularity leads to a higher accuracy, which is especially useful for drops with very thin layers. The resulting transformed integral in (5-7) is evaluated numerically using the four-point Gauss quadrature (Evans [73]).

In the remainder of this section, we discuss the numerical evaluation of the domain integral. The domain integral $\mathcal{I}_2(\bar{\boldsymbol{x}}; \bar{V}_m^{(l)})$ can be written as:

$$\begin{aligned}\mathcal{I}_1(\bar{\boldsymbol{x}}; \bar{V}_m^{(l)}) &= \int_{\bar{V}_m^{(l)}} M^\beta_{\ \alpha}(\bar{\boldsymbol{r}}) \bar{\partial}_\gamma \bar{\bar{\tau}}^{(l)}_{\beta\gamma}(\bar{\boldsymbol{y}}) \bar{y}_2 \, d\bar{y}_2 d\bar{y}_1 \\ &= \int_0^1 \int_0^1 M^\beta_{\ \alpha}(\bar{\boldsymbol{r}}) \bar{\partial}_\gamma \bar{\bar{\tau}}^{(l)}_{\beta\gamma}(\bar{\boldsymbol{X}}(s_1, s_2)) \bar{X}_2(s_1, s_2) J_B^{(l)}(s_1, s_2) \, ds_2 ds_1,\end{aligned}$$

where we have used the bilinear representation (5-1) of the m-th quadrilateral element. The Jacobian $J_B^{(l)}$ is given by:

$$J_B^{(l)} = \det\left(\frac{\partial \bar{X}_\alpha(s_1, s_2)}{\partial s_\beta}\right).$$

Unlike the interface integrals, we now do distinguish between two cases; (a) the internal cell does not contain the point $\bar{\boldsymbol{x}}$, and (b) the internal cell does contain the point $\bar{\boldsymbol{x}}$. In case (a) the domain integrand is regular and a standard Gauss quadrature is used to evaluate the integral. In case (b) the integrand is singular and a special treatment of the singularities in the kernels is required. To remove the singularity, we use the same quadratic transformation as for the boundary integral for both integration variables s_1 and s_2. After the removal of the singularity, a standard Gauss quadrature is used in both integration directions to evaluate the integral numerically.

With the techniques described in this subsection, we are able to calculate the velocity field for a compound non-Newtonian drop. In the next subsection, we discuss the techniques used to evaluate the integral expressions for a dispersion of drops.

5.3.2 Periodic suspension of drops

In order to calculate the velocity field for a periodic suspension of drops, we need to solve the integral equation (4-52) at all collocation points. Analyzing the periodic Green's functions, we find that $J^P_{ik}(\boldsymbol{r})$ and $K^P_{ijk}(\boldsymbol{r})$ contain a logarithmic and a $1/|\boldsymbol{r}|$ singularity. As the latter singularity cannot be removed

using a Telles transformation we rewrite (4-52) as:

$$\frac{1}{2}(1+\lambda_m)u_k(\boldsymbol{x}) + \sum_{l=1}^{N}(1-\lambda_l)\int_{S_l^{[\mathbf{0}]}} K_{ijk}^P(\boldsymbol{r})\{u_i(\boldsymbol{y}) - u_i(\boldsymbol{x})\}n_j(\boldsymbol{y})\,dS_y +$$
$$\sum_{l=1}^{N}(1-\lambda_l)\int_{S_l^{[\mathbf{0}]}} K_{ijk}^P(\boldsymbol{r})u_i(\boldsymbol{x})n_j(\boldsymbol{y})\,dS_y =$$
$$u_k^{\infty}(\boldsymbol{x}) - \sum_{l=1}^{N}\int_{S_l^{[\mathbf{0}]}} J_{ik}^P(\boldsymbol{r})q_i(\boldsymbol{y})\,dS_y,$$

According to the integral identity (4-51), the second integral on the left-hand side of the expression above equals zero, which leads to the following expression for the velocity:

$$u_k(\boldsymbol{x}) + \sum_{l=1}^{N}(1-\lambda_l)\int_{S_l^{[\mathbf{0}]}} K_{ijk}^P(\boldsymbol{r})\left\{u_i(\boldsymbol{y}) - u_i(\boldsymbol{x})\right\}n_j(\boldsymbol{y})dS_y =$$
$$u_k^{\infty}(\boldsymbol{x}) - \sum_{l=1}^{N}\int_{S_l^{[\mathbf{0}]}} J_{ik}^P(\boldsymbol{r})q_i(\boldsymbol{y})dS_y. \tag{5-8}$$

It is noted that the term $\{u_i(\boldsymbol{y}) - u_i(\boldsymbol{x})\}$ removes the $1/|\boldsymbol{r}|$ singularity in the integrand. With the discretization of the boundaries described in section 5.2, we can rewrite (5-8) as:

$$u_k(\boldsymbol{x}) + \sum_{l=1}^{N}(1-\lambda_l)\sum_{m=1}^{N_b}\mathcal{I}_1(\boldsymbol{x},\boldsymbol{u};S_{lm}^{[\mathbf{0}]}) = u_k^{\infty}(\boldsymbol{x}) - \sum_{l=1}^{N}\sum_{m=1}^{N_b}\mathcal{I}_2(\boldsymbol{x};S_{lm}^{[\mathbf{0}]}) \tag{5-9}$$

where $\mathcal{I}_1(\boldsymbol{x},\boldsymbol{u};S_{lm})$ and $\mathcal{I}_2(\boldsymbol{x};S_{lm})$ are integrals over the m-th boundary element corresponding to the l-th drop within a periodic cluster:

$$\mathcal{I}_1(\boldsymbol{x},\boldsymbol{u};S_{lm}) = \int_{S_{lm}} K_{ijk}^P(\boldsymbol{r})\left\{u_i(\boldsymbol{y}) - u_i(\boldsymbol{x}\right\}n_j(\boldsymbol{y})dS_y \tag{5-10}$$

$$\mathcal{I}_2(\boldsymbol{x};S_{lm}) = \int_{S_{lm}} J_{ik}^P(\boldsymbol{r})q_i(\boldsymbol{y})dS_y. \tag{5-11}$$

Observe that only $\mathcal{I}_2(\boldsymbol{x};S_{lm})$ contributes to u_k in case $\lambda = 1$.

The integral $\mathcal{I}_2(\boldsymbol{x};S_{lm})$ contains a logarithmic singularity which is removed using a Telles transformation, as discussed in the previous subsection. The resulting transformed integral is evaluated numerically using Gauss quadrature

(Evans [73]). In order to evaluate the regular integral $\mathcal{I}_1(\boldsymbol{x}, \boldsymbol{u}; S_{lm})$, we assume that $\boldsymbol{u}$ varies linearly over a boundary element. Using these techniques we can rewrite (5-9) as a matrix equation:

$$A\boldsymbol{u} = \boldsymbol{f}, \tag{5-12}$$

where A contains the integration weights, $\boldsymbol{u}$ is the velocity in all the collocation points, and $\boldsymbol{f}$ is the right-hand side of (5-9). The matrix equation is solved using an iterative Gauss-Seidel solver. Since the method described above gave rise to large volume losses at $\lambda = 0$ and to instabilities at $\lambda = \infty$, we implemented a Wielandt eigenvalue deflation as described at the end of section 4.2.

With these numerical techniques we have available a method to calculate the velocity of the stationary problem (4-52) at all collocation points. Preliminary computations, however, indicate that we need excessive computation time for the calculation of the velocity if we use a direct evaluation of the Green's functions J_{ik}^P and K_{ijk}^P. Therefore, it was decided to use a tabulation technique for the Green's functions and evaluate them by interpolation (Loewenberg and Hinch [31], Li et al. [30]).

To improve the accuracy, we only tabulate the regular part of the Green's functions by first subtracting the singular part with respect to the nearest periodic point force. This is subsequently compensated after the interpolation by evaluating the singular part exactly in the specific point. From (4-55) it follows that the periodic Green's function depends on r and the lattice vectors $\boldsymbol{a}$ and $\boldsymbol{b}$. Since $\boldsymbol{a}$ and the x_2-component of $\boldsymbol{b}$ are constant throughout the simulation, it is sufficient to tabulate the regular parts of the Green's functions in three directions on an evenly spaced rectangular grid. Two of the tabulation directions are formed by the r_1- and r_2-components. Because of the periodicity of the functions, it is sufficient to tabulate over a region with the size of the area enclosed by the original lattice vectors $\boldsymbol{a}_0$ and $\boldsymbol{b}_0$ (see figure 5-2). The third tabulation direction is used to account for the distortion of the lattice vector $\boldsymbol{b}$ due to the imposed shear flow. As discussed in subsection 2.1.2, only the first component of the lattice vector $\boldsymbol{b}$ changes in time, implying that we only need one extra tabulation direction. Since the vector $\boldsymbol{b}$ is "switched" back to its original form regularly, we tabulate the region defined by $\boldsymbol{a}_0$ and $\boldsymbol{b}_0$ for a finite number of angles between $\boldsymbol{b}_t$ and $\boldsymbol{b}_0$ as depicted in figure 5-2. To generate the interpolation table at the beginning of a simulation, the functions J_{ik}^P and K_{ijk}^P are evaluated at all the grid points defined within the tabulated area, using the accelerated summation method described earlier in section 4.4. To increase the efficiency, the interpolation tables are stored on disk in order

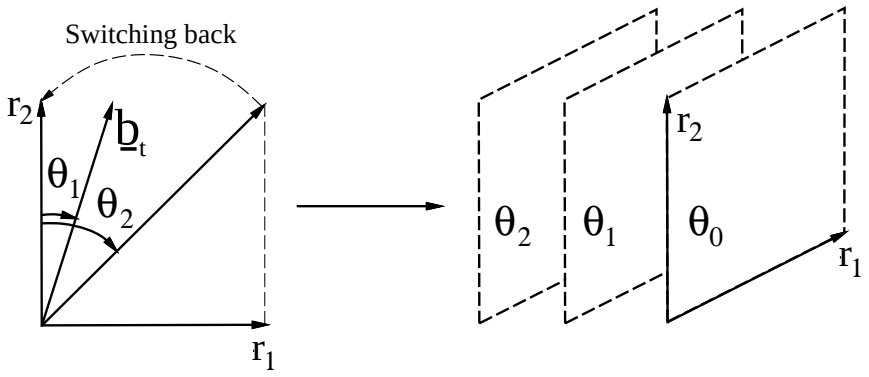

Figure 5-2: Schematic representation of the three dimensional table

to be able to re-use them.

Once the three dimensional table is filled, the functions J^P_{ik} and K^P_{ijk} can be evaluated in each arbitrary point by a linear interpolation in the three directions. Points outside the tabulation box are first associated with the corresponding point in the tabulation box. After that, the eight interpolation points needed to evaluate the Green's functions for arbitrary $\boldsymbol{r}$ and θ can simply be obtained from the tabulation box using the known tabulation intervals and coordinates of $\boldsymbol{r}$. Using these tabulation and interpolation processes, the computation time needed to evaluate a periodic suspension is reduced by more than a factor of one hundred compared to a simulation in which the periodic Green's functions are calculated directly wherever required.

With these numerical techniques, we have devised an overall second-order accurate method to calculate the velocity of the stationary problem (4-42) in all collocation points. In the next subsection, we discuss the coupling of this solution with the time-dependent problem.

5.4 Time integration

In this section, we describe the method to find the non-Newtonian stress tensor and the shape of the interfaces $\bar{S}^{(l)}$ at the new time level.

Updating the shape of the interface and the grid covering the l-th layer $\bar{V}^{(l)}$ requires the calculation of the position of all collocation points at the new time level. This calculation can be performed by time integration of (2-17),

e.g. with an Euler forward scheme:

$$\bar{\boldsymbol{x}}_i(t_{n+1}) = \bar{\boldsymbol{x}}_i(t_n) + \Delta t\, \bar{\boldsymbol{u}}_i, \tag{5-13}$$

with $t_n = n\Delta t$, where Δt is a constant time step and $\bar{\boldsymbol{u}}_i$ the velocity at the i-th collocation point $\bar{\boldsymbol{x}}_i$ at time t_n. Moving the grid points in this way, however, may lead to a clustering of both internal and boundary grid points in certain regions and hence a highly deformed grid develops, leading to inaccurate results. The clustering arises directly from the fact that the boundary condition (2-13) puts no restrictions on the stress tensor in the tangential direction implying that the points move along the interface in the direction of the external velocity field. To prevent the clustering of the collocation points we redistribute the boundary points every time step. To this end, we introduce an auxiliary set of collocation points $\bar{\boldsymbol{y}}_i$ at the interface by:

$$\bar{\boldsymbol{y}}_i(t_{n+1}) = \bar{\boldsymbol{y}}_i(t_n) + \Delta t\, (\bar{\boldsymbol{u}}_i + \bar{\boldsymbol{w}}_i^{(l)}), \quad \bar{\boldsymbol{y}}_i \in \bar{S}^{(l)}, \tag{5-14}$$

where $\boldsymbol{w}^{(l)}$ denotes an extra velocity field along the interface $\bar{S}^{(l)}$ which partly compensates for the tangential movement of the grid points. It is noted that the vector $\boldsymbol{w}^{(l)}$ should have no effect on the shape of the boundary, which implies that it should be parallel to the interface.

For an axisymmetric compound drop, $\bar{\boldsymbol{w}}_i$ is given by

$$\bar{\boldsymbol{w}}_i^{(l)} = \alpha_i^{(l)} \bar{\boldsymbol{t}}_i^{(l)}, \quad i = 0, \ldots, N_p^{(l)},$$

where $\bar{\boldsymbol{t}}_i^{(l)}$ is the unit tangent vector along the l-th interface (no summation over the index i). The coefficients $\alpha_i^{(l)}$ are determined such that:

$$|\bar{\boldsymbol{y}}_{i+1} - \bar{\boldsymbol{y}}_i| \left(\bar{\partial}_\gamma \bar{n}_\gamma(\bar{\boldsymbol{y}}_i) + \bar{\partial}_\gamma \bar{n}_\gamma(\bar{\boldsymbol{y}}_{i+1})\right), \quad \bar{\boldsymbol{y}}_i \in \bar{S}^{(l)}, \tag{5-15}$$

is constant for all i at the new time level. Note that the term between the parentheses is proportional to the local curvature, so that in regions of high curvature the distance between gridpoints is decreased. In order to ensure that the points lying on the x_1 axis initially remain on this axis during the entire simulation, we set $\alpha_0^{(l)}$ and $\alpha_{N_p}^{(l)}$ equal to zero. The unknowns $\alpha_i^{(l)}$ are found by taking the value of (5-15) of the previous timestep and subsequently calculate the corresponding $\alpha_i^{(l)}, i = 1, \ldots, N_p^{(l)}$ using (5-14) and (5-15). The correct value for (5-15) such that $\alpha_{N_p}^{(l)} = 0$ is found using a Newton iteration method. By using this grid movement scheme the points are redistributed in such a way that areas with high curvature have a higher concentration of grid

points than areas with low curvature (see figure 5-3). The interior collocation points are found subsequently by generating a new grid at each time step. This is done by interpolation between the new auxiliary interface points on the interfaces $\bar{S}^{(l)}$ and $\bar{S}^{(l+1)}$. For a layer consisting of a viscoelastic model we simply use the Euler scheme (5-13) since the non-fading elasticity of the stress tensor compensates the viscous stress in tangential direction which by itself prevents clustering of the collocation points.

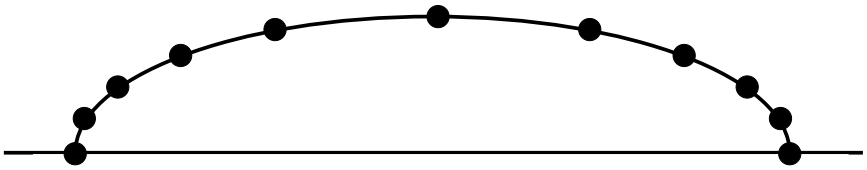

Figure 5-3: Effects of the redistribution scheme.

Although the scheme presented above works fine, it is computationally costly. To circumvent this problem, we adopted a cheaper but less robust scheme for a periodic suspension of drops. In this scheme, the coefficients $\alpha_i^{(l)}$ are defined by the following rule (Loewenberg and Hinch [31] and Van der Klis and Toose [49]):

$$\alpha_i^{(l)} = \frac{4}{1+\lambda} \sum_{j=-1}^{j=1} \left[1 + 2(k(\boldsymbol{x}_i) + k(\boldsymbol{x}_{i+j}))|v[i] - v[i+2j]|\right] (v[i] - v[i+j])$$

where $k(\boldsymbol{x}_i) = |\partial_j n_j(\boldsymbol{x}_i)|$ denotes the absolute value of the curvature and $v[i]$ is the chord length parametrisation as defined in section 5.2. It is noted that this expression is actually a weighted balance between the curvature on the left and right of the point $\boldsymbol{x}_i$. In this respect, the formulation presented above is quite similar to (5-15). The constant in front of the summation ensures that the grid points are not displaced too much when the viscosity ratios are large. By using this grid movement scheme, the points are redistributed in such a way that a higher density of grid points arises in regions with high curvature as illustrated in figure 5-3. Having discussed the grid movement, we finally turn to the evolution of the stress tensor.

The new non-Newtonian stress tensor in the numerical algorithm is obtained either by explicitly evaluating the stress (3-20) at the new time level, or by integration of the differential constitutive equation, depending on the chosen model. In order to calculate the stress for the viscoelastic model, we need to evaluate the Cauchy-Green tensor (3-19) which requires the derivatives of the deformed grid with respect to a reference grid. For the reference grid we use the grid at the initial time level, and the partial derivatives are evaluated using a second-order accurate finite-difference scheme. Details concerning finite-difference methods in curvilinear coordinates can be found in Thompson et al. [74]. When the non-Newtonian stress tensor is prescribed by a differential constitutive equation, we integrate the stress in time. To perform this integration for a differential model, we have to evaluate the upper convected time derivative using a partial or a material time derivative. The use of the partial time derivative, however, leads to a convective term which is difficult to calculate. It is then more convenient to use the material time derivative which does not require an explicit calculation of the convective term. This implies that the new non-Newtonian stress tensor $\bar{\bar{\tau}}_{\beta\gamma}$ will be defined on the grid which is convected according to (5-13). Integration of the differential constitutive equation with an Euler forward scheme leads to:

$$\bar{\bar{\tau}}_{\beta\gamma}(t_{n+1}) = \bar{\bar{\tau}}_{\beta\gamma}(t_n) + \Delta t \left(g^{\nu\mu} \left[\bar{\partial}_\nu \bar{u}_\beta(t_n) \bar{\bar{\tau}}_{\mu\gamma}(t_n) + \bar{\bar{\tau}}_{\beta\nu}(t_n) \bar{\partial}_\mu \bar{u}_\gamma(t_n) \right] + \bar{R}_{\beta\gamma}(t_n) \right). \quad (5\text{-}16)$$

with $g^{\nu\mu}$ the contravariant metric tensor of the transformation(4-24), and $\bar{R}_{\beta\gamma}$ specifies the specific differential model used. The covariant derivative $\bar{\partial}_\beta$ in (5-16) is defined as (Bird [34]):

$$\bar{\partial}_\beta \bar{u}_\gamma = \frac{\partial \bar{u}_\gamma}{\partial \bar{x}^\beta} - \left\{ \begin{matrix} \xi \\ \gamma \ \beta \end{matrix} \right\} \bar{u}_\xi, \quad (5\text{-}17)$$

As an alternative to the first order Euler scheme a second- or higher-order Runge-Kutta scheme can be used.

Due to the Lagrangian approach, i.e. using a material time derivative, the new stress tensor $\bar{\bar{\tau}}_{\beta\gamma}(t_{n+1})$ resulting from (5-16) is defined on the grid whose positions are given by (5-13). In order to find it on the new grid $\bar{\boldsymbol{y}}_i$, the stress tensor is interpolated using:

$$\bar{\bar{\tau}}_{\beta\gamma}(\bar{\boldsymbol{y}}_i) \approx \frac{1}{\sum_{j\in J} 1/(D_{ij})^2} \sum_{j\in J} \frac{\bar{\bar{\tau}}_{\beta\gamma}(\bar{\boldsymbol{x}}_j)}{(D_{ij})^2}, \quad (5\text{-}18)$$

with $D_{ij} = |\bar{\boldsymbol{y}}_i - \bar{\boldsymbol{x}}_j|$ and the summation $j \in J$ involves all the indices of the nearest neighbors of the grid point $\bar{\boldsymbol{y}}_i$. To ensure that this interpolation is sufficiently accurate, we introduce a time step restriction:

$$\Delta t = \epsilon \min_n \left\{ \frac{\Delta \bar{x}_n}{\bar{u}_n} \right\}, \tag{5-19}$$

where $\Delta \bar{x}_n$ is the shortest side of the n-th internal cell, $\bar{u}_n$ is the mean velocity over this element, and ϵ is on the order of 0.1.

Chapter 6

Non-Newtonian drops

In this chapter, we present the results of numerical calculations which validate the numerical method, and study the effects of the non-Newtonian character on the deformation of a simple drop. For the validation of the numerical method, we perform a grid refinement study and compare the numerical results with available analytical results known from literature (section 6.1). In section 6.2, we study the effects related to the non-Newtonian character by considering the steady state of the drops. Finally, in 6.3 we present some conclusions. Since we are considering only simple drops in this chapter, we will drop the superscript indicating the domain of definition.

6.1 Validation

In this section, we study the response of an axisymmetric drop containing an Oldroyd-B fluid or a viscoelastic material to an elongational flow. Before we are concerned with the validation of the method, we first show a typical example of a deformed drop and the corresponding velocity field.

In figure 6-1, a vector plot of the steady-state velocity field of a fluid-like drop (i.e. viscous or Oldroyd-B drop) at $C = 0.1$ is drawn. In the velocity field, we can distinguish two recirculation zones, drawn schematically in the lower part of the figure. For the viscoelastic drops no such vortices exist since the velocity becomes zero in the steady state due to the non fading elasticity of the viscoelastic material (chapter 3).

We investigate the order of accuracy of the numerical method with a grid refinement study (Toose [45]). Suppose we have numerically obtained the solution at a certain time t_0 on a given grid. The deformation $D(t_0)$ should asymptotically converge to its exact value at a certain rate as the grid is

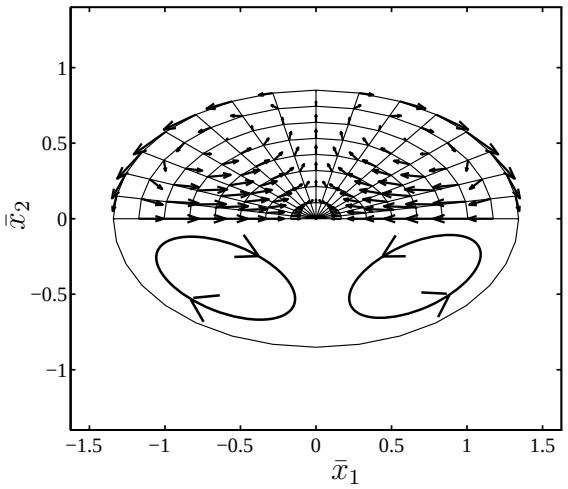

Figure 6-1: The velocity profile and grid of a viscous drop with $\lambda = 1$ at $C = 0.1$. In the lower part of the figure the vortices which are present in the velocity profile are drawn schematically.

refined. The order of accuracy of the method can be obtained from the values of $D(t_0)$ on subsequent refinement levels. The values of the convergence rate ρ_i, defined by:

$$\rho_i = \frac{D_{(i+1)} - D_{(i)}}{D_{(i+2)} - D_{(i+1)}} \text{ , for } i \geq 0, \tag{6-1}$$

on the set of grids is of importance in this respect. Here $D_{(i)}$ is the deformation of the drop on the i-th refinement level at time t_0. The grid is usually refined with a Romberg sequence, in which the grid spacing is halved at each refinement. It is, however, more efficient to use a Bulirsch-sequence consisting of two intertwined Romberg sequences (Stöer [75]):

$$h_1 = h_0/2 \text{ , } \quad h_2 = h_0/3 \text{ , } \quad h_{i+1} = h_{i-1}/2 \text{ , for } i \geq 2, \tag{6-2}$$

where h_0 is an initial grid spacing and h_i is the grid spacing of the Bulirsch sequence. Note that h_0 is not used in the calculation of the converge rate. The values of ρ_i corresponding to an order $\gamma = 1, 2, 3$ for both Romberg and Bulirsch sequences are given in table 6-1 (Toose [76]). In this table, it is observed that the Bulirsch row has two convergence rates. Refinements of time-step intervals can be performed analogously. In table 6.1, we present typical grid refinement results for an Oldroyd-B drop with $\lambda_p = 5$ and $De =$

γ	ρ_i Romberg row	ρ_i Bulirsch row	
		i is even	i is odd
1	2	1	2
2	4	1.4	2.857
3	8	1.947	4.108

Table 6-1: Convergence rates Romberg and Bulirsch row

1 using the deformation at $t_0 = 1$ at two different values of the capillary number. Note that the time step is kept constant in this grid refinement study. Analyzing the convergence behavior of the deformation, we find that

Grid		Deformation ($t = 1$)	
N_b	N_c	$C = 0.01$	$C = 0.1$
16	80	0.016311	0.15152
24	168	0.016504	0.15262
32	288	0.016569	0.15299
48	624	0.016611	0.15323
64	1088	0.016625	0.15330

Table 6-2: Grid refinement results of the deformation of an Oldroyd-B drop ($\lambda_p = 5$ and $De = 1$) at $t_0 = 1$ for two different capillary numbers ($C = 0.01$ and $C = 0.1$).

the method is second-order accurate in space for this specific case. Besides a rapid convergence, the method also gives very good results for relatively coarse grids. Using a similar refinement study for the timestep, we find that the accuracy in time is first-order for the Euler scheme and second-order for the compact storage four stage Runge-Kutta scheme (Jameson [77]). To provide a way to validate the correctness of the numerical method, we next compare our numerical results with theoretical results from literature and investigate several limiting cases of the non-Newtonian stress tensor.

The Oldroyd-B model contains three independent parameters, the viscosity ratios λ and λ_p and the Deborah number De. If either λ_p or De approaches zero, an essentially Newtonian behavior results (Toose et al. [46]). This will be used in the sequel to establish the correctness of the boundary-integral method for the simulation of non-Newtonian drops. In the first case considered here,

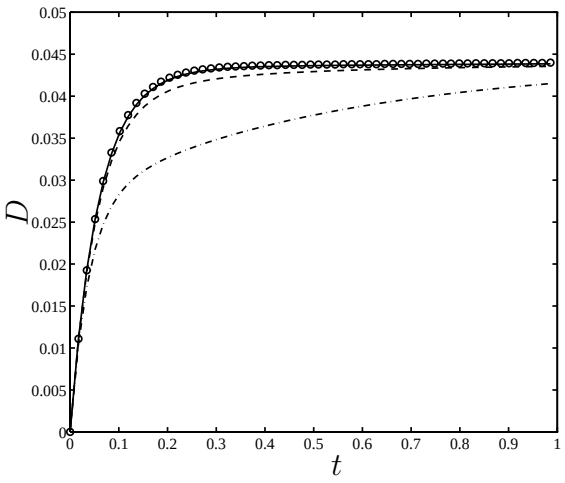

Figure 6-2: Deformation of an Oldroyd-B drop at $C = 0.025$ for a fixed Deborah number $De = 0.33$. The dash-dotted, dashed and solid lines are the responses of a non-Newtonian drop with $\lambda_p = 6.7$, 0.89 and 0.12 respectively. The circles show the response of the Newtonian drop at $\lambda = 1$.

λ_p approaches zero and the equation for the non-Newtonian stress tensor (2-7) reduces to:

$$De\mathcal{D}_t\tilde{\tau}_{ij} + \tilde{\tau}_{ij} = 0.$$

This equation implies that $\tilde{\tau}_{ij}$ remains zero in time since we use $\tilde{\tau}_{ij} = 0$ at $t = 0$. Hence the deformation should approach the Newtonian results as λ_p tends to zero, which is demonstrated in figure 6-2. Here the deformation of a Oldroyd-B drop for several values of λ_p and constant $De = 0.33$ is plotted. The numerical results were obtained on a 32×9 grid using a time step of 0.001.

In the second case, we let De approach zero, so that (2-7) reduces to:

$$\tilde{\tau_{ij}} = \lambda_p\dot{\gamma}_{ij},$$

i.e. a Newtonian stress tensor. This implies that for $De = 0$ the non-Newtonian drop reduces to a Newtonian drop with a viscosity ratio $\lambda = 1 + \lambda_p$. In figure 6-3 the deformation of a drop for several values of De and constant $\lambda_p = 0.33$ is plotted. The numerical results were obtained using the same grid and time step as above. It is observed that for small De the deformation of the non-Newtonian drop approaches the deformation of the Newtonian drop

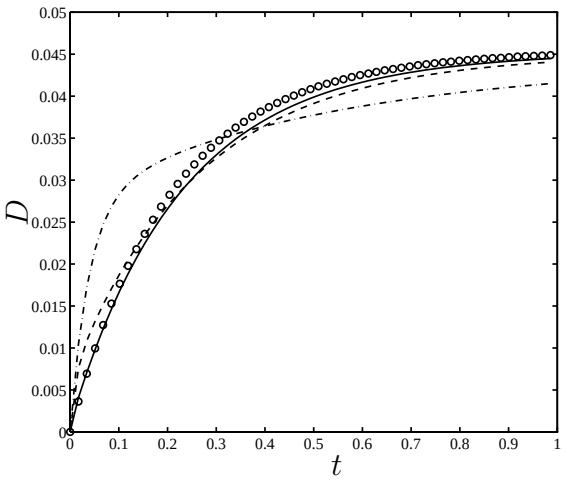

Figure 6-3: Deformation of an Oldroyd-B drop at $C = 0.025$ for a fixed viscosity ratio $\lambda_p = 0.33$. The dash-dotted, dashed and solid lines represent the response of a non-Newtonian drop with $De = 6.7$, 0.89 and 0.12 respectively. The circles show the response of the Newtonian drop at $\lambda = 1 + \lambda_p$.

with $\lambda = 1 + \lambda_p$. From this we can conclude that the limiting behavior of the Newtonian drop is correctly recovered. The behavior of the non-Newtonian drop for moderate values of λ_p and De is surveyed next.

To validate the results for moderate values of λ_p and De, we use theoretical results obtained by Delaby et al. [16]. The theoretical background for these results is based on the linear theory for viscous emulsions of Oldroyd [78, 79], which has recently been extended to viscoelastic emulsions by Palierne [80]. This linear theory starts with the solution to the Stokes equation in terms of an expansion in spherical harmonics (Lamb [22]). By approximating the shape of the interface in terms of spherical harmonics, one can use the boundary conditions of the problem to find the leading-order correction to a spherical shape. The amplitude of this correction for the radial displacement of the interface is given by:

$$A(\omega) = \frac{5G_o^*(19G_d^* + 16G_o^*)}{(2G_d^* + 3G_o^*)(19G_d^* + 16G_o^*) + 40C(G_d^* + G_o^*)}, \qquad (6\text{-}3)$$

where G_d^* and G_o^* are the complex moduli of the drop fluid and outer fluid, respectively. In case of an Oldroyd-B drop placed in a viscous fluid, the

complex moduli G_d^* and G_o^* are given by:

$$G_d^* = i\omega\lambda + \frac{i\omega\lambda_p}{1 + i\omega De}, \quad G_o^* = i\omega,$$

with i the imaginary unit and ω the frequency of the oscillations of the external flow. The amplitude $A(\omega)$ can also be written in the form:

$$A(\omega) = A_\infty \left(1 - \sum_j \frac{B_j}{1 + i\omega\mu_j} \right).$$

where the coefficients B_j, relaxation times μ_j of the deformation process, and A_∞ are evaluated numerically for particular values of the parameters. The response of the deformation to an elongational flow is then given by:

$$D(t) = \frac{3A_\infty C}{4} \left\{ (1 - \sum_j B_j)t + \sum_j B_j\mu_j \left(1 - e^{-t/\mu_j} \right) \right\}. \qquad (6\text{-}4)$$

For an Oldroyd-B drop we found three relaxation times which were all real, and observed that the sum of the coefficients B_j equals one. In figure 6-4, we plot expression (6-4) for three values of the Deborah number De and $\lambda_p = 5$ of the Oldroyd-B fluid and some corresponding numerical results. The numerical results were generated using a grid with 48 boundary elements and 624 cells in the internal domain. For small values of the relaxation time of the Oldroyd-B model, the analytical and numerical results are in good agreement. The steady-state deformation of the analytical solution for small relaxation times of the Oldroyd-B model lies somewhat below the numerically obtained values. Comparison with a second-order theory for viscous drops (Barthès-Biesel [11]) reveals that the numerically obtained steady state deformation is correct and that the linear theory slightly underpredicts this deformation. For higher values of De there are some discrepancies between the analytical and numerical results which cannot be explained by shortcomings in the first order theory. In this case the differences are caused by the nonlinear character of the upperconvected time derivative in the constitutive equation for the Maxwell model. Analyzing this equation we observe that the nonlinearity increases with increasing relaxation time of the model. This could explain the increased discrepancies with increasing relaxation time. In order to establish this we performed a simulation where the upper-convected time derivative is replaced with a material time derivative, i.e. $\mathcal{D}_t = d_t$. From a simulation performed with

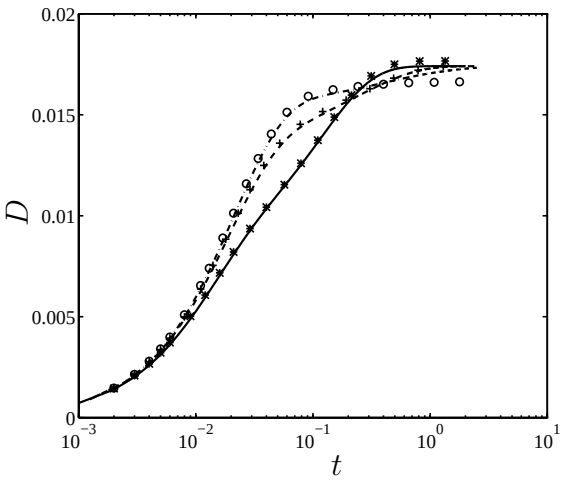

Figure 6-4: The deformation of an Oldroyd-B drop with $\lambda = 1$ at $C = 0.025$ for three values of the relaxation time De. The viscosity ratio λ_p is kept constant at 5. The dash-dotted, dashed and solid lines represent the analytical results for $De = 1$, 0.25 and 0.0625 respectively. The circles, pluses and asterisks display the corresponding numerical results.

such a derivative, it was observed that the numerical and analytical results were in better agreement. In this case, the steady state deformation equals that of a Newtonian drop for all De as predicted by the linear model.

The viscoelastic model given in (3-20) contains two independent parameters, c_1 and c_2. For the validation, we consider two cases; the viscoelastic I and the viscoelastic II model (subsection 3.2). To validate our results we use theoretical predictions obtained by Roscoe [59] for viscoelastic spheres. Assuming that the shape of the drop remains ellipsoidal in time, the longest axis r_{max} of the drop follows from the following nonlinear equations [59]:

$$\begin{cases} \dfrac{5}{4} g_2(r_{max})\{r_{max}^2 - r_{max}^{-1}\} = \dfrac{5\eta G}{2c_1} & \text{if} \quad c_2 = 0 \\ \dfrac{5}{4} g_2(r_{max})\{r_{max} - r_{max}^{-2}\} = \dfrac{5\eta G}{2c_2} & \text{if} \quad c_1 = 0, \end{cases} \tag{6-5}$$

where the function $g_2(y)$ is defined as (Jeffery [81]):

$$g_2(y) = \int_0^\infty \frac{z\, dz}{(y^2 + z)^{3/2}(y^{-1} + z)^2}.$$

By evaluating $g_2(y)$ numerically for several r_{max} we obtain the relation between the deformation D and the constants c_1 or c_2 since D can be calculated

from r_{max} under the assumption that the shape remains ellipsoidal and the incompressibility of the fluid. In figure 6-5, we have plotted the numerical

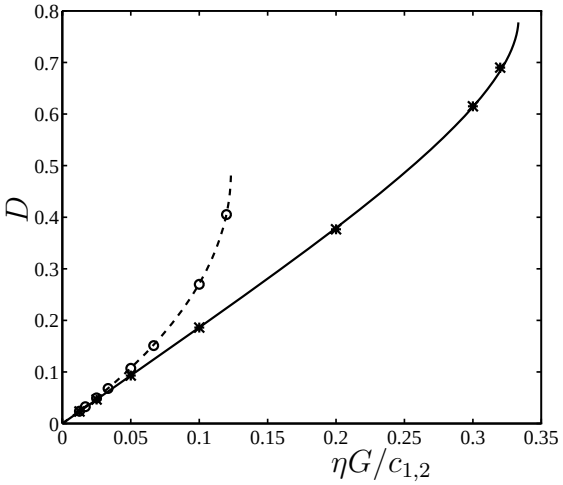

Figure 6-5: Steady-state deformation of a viscoelastic drop with $\lambda = 1$ for a constant value of either c_1 or c_2. The solid and dashed lines represent the analytical results for $c_2 = 0$ and $c_1 = 0$ respectively. The asterisks and circles display the corresponding numerical results.

and analytical results for the steady-state deformation of a drop consisting of a viscoelastic I or II material. For the numerical calculations we used a grid with 16 boundary elements and 128 cells in the internal domain. For all values of c_1 and c_2 the analytical and numerical results are in very good agreement. The models exhibit the same behavior for small deformations, (i.e. large values of c_1 or c_2) and differ strongly for large deformations. The viscoelastic II drop shows strong nonlinear behavior for larger deformations, which is well captured by the numerical method. From this we can conclude that the method gives correct results for a drop consisting of an Oldroyd-B fluid or a viscoelastic material. We also find that the method is capable of dealing with large deformations and strongly nonlinear behavior of the non-Newtonian stress tensor.

6.2 General exploratory results

In this section we give a brief overview of the steady-state behavior of a simple drop containing a dilute polymer solution. To study the steady state behavior,

we considered a drop at a constant viscosity ratio and varied the capillary number. In the simulations we used either an Oldroyd-B or a CR model since these models have a constant viscosity (see section 3.3).

In table 6.2, we have displayed the deformation of an Oldroyd-B drop with $\lambda(1+c) = 10$ for several values of the polymer concentration. The numerical

	Deformation			
C	$c = 0$	$c = 0.1$	$c = 1$	$c = 10$
0.2	0.0361	0.0363	0.0356	0.0352
0.4	0.0770	0.0775	0.0761	0.0755
0.6	0.125	0.126	0.124	0.123
0.8	0.188	0.189	0.185	0.183

Table 6-3: Deformation of an Oldroyd-B drop ($De = 0.5$) for different values of the polymer concentration. The viscosity ratio $\lambda(1+c)$ is equal to 10 in all cases.

results were generated using a grid with 32 boundary elements and 544 cells in the internal domain. From the numerical results we observe that the steady-state deformation of the Oldroyd-B model is somewhat lower $(1 - 2\%)$ than the corresponding value of a Newtonian drop for the two higher viscosity ratios. Calculations at viscosity ratios of 0.1 and 1 showed similar results for all capillary numbers. At $\lambda(1 + c) = 0.1$ instabilities arose at higher capillary numbers leading to a breakdown of the numerical scheme. The instabilities were probably caused by large gradients in the non-Newtonian stress tensor due to the singular behavior of the Oldroyd-B model at $De = 0.5$. Grid refinement removed these instabilities. Preliminary computations using a CR model with a maximum spring length $L = 10$ indicated that the steady state deformation is similar to an Oldroyd-B drop. With this model, however, no instabilities at $De = 0.5$ were found.

6.3 Conclusions

In the first section of this chapter, the method for a simple drop was numerically and physically validated. The numerical validation was performed by grid refinement and a study of convergence, whereas the physical validation involved the comparison of numerically obtained results with analytical results from literature. The simulations performed for the numerical validation

show that the numerical method is second-order accurate in space. Besides a rapid convergence, the method also gives very good results on relatively coarse grids. From the physical validation process, it followed that the time-dependent behavior of a simple Oldroyd-B drop is in good agreement with analytical results for small values of the Deborah number (Delaby et al. [16]). For a drop containing an elastic material, we examined the steady state behavior. It was found that the numerical and analytical results are in excellent agreement with each other and that strongly nonlinear behavior of the drop is well captured by the method.

From the results presented in section 6.2 we can conclude that the steady-state deformation of a simple drop subjected to a elongational flow is hardly influenced by the non-Newtonian character of the polymeric solution composing the drop. This outcome is in agreement with experiments performed with viscoelastic drops subjected to a planar elongational flow (Milliken and Leal [82]).

Chapter 7

Compound drops

In the preceding chapter we focused on the steady state and transient behavior of simple non-Newtonian drops subjected to an elongational flow. In this chapter, we consider a compound drop consisting of a viscous Newtonian core encapsulated by a layer consisting of a certain non-Newtonian material. Since the implementation of the boundary integral method differs from that for a simple drop, we start this chapter with an explicit validation of the numerical method. In section 7.2 the breakup mechanism of a compound drop with a viscoelastic outer layer is studied. Finally, in section 7.3 we formulate some conclusions.

7.1 Validation

In this section, we present some simulation results for a drop consisting of two types of material. The internal core $V^{(2)}$ consists of a viscous fluid with $\lambda^{(2)} = 1$ and the outer layer $V^{(1)}$ consists of a (non-)Newtonian material. Analytical results are only known for a drop where $V^{(1)}$ consists of a viscous or a viscoelastic material. For this reason, we restrict ourselves to these two situations and do not discuss a drop where $V^{(1)}$ contains an Oldroyd-B fluid, although the method is perfectly suitable for this situation as well. Since we are considering compound drops with only a single layer of non-Newtonian material, we will drop the superscripts whenever possible.

As for the simple drop we first turn our attention to a typical example. In figure 7-1(a) the steady state velocity field and grid of a viscous drop with $C^{(1)} = C^{(2)} = 0.025$ and $\lambda^{(1)} = 1$ is plotted. In the second layer two toroidal recirculation zones are present which are also drawn schematically in the lower part of the figure. It is seen that these zones deform the inner interface in

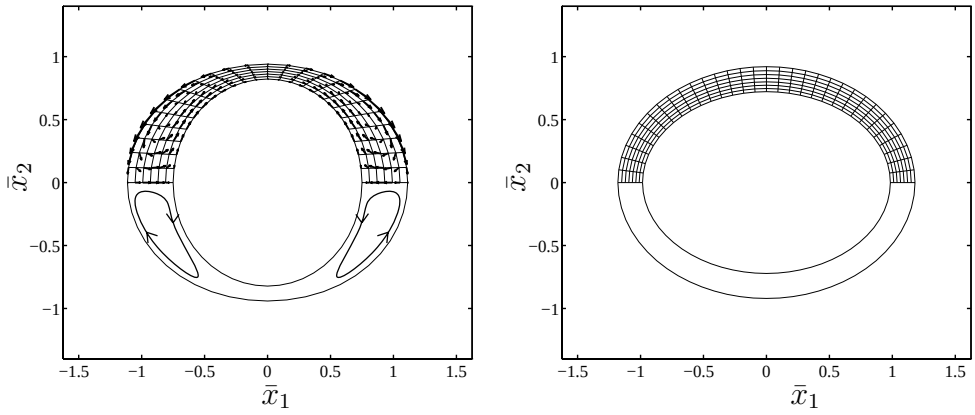

(a) Viscous layer (b) Viscoelastic layer

Figure 7-1: The velocity profile and grid of a viscous drop encapsulated by (a) a viscous layer ($C^{(1)} = C^{(2)} = 0.1$) and (b) a viscoelastic layer ($c_1 = 80,\ c_2 = 0$). In both cases the viscosity ratios are equal to one and the initial thickness of the outer interface is 0.2. In the lower part of 7-1(a) the vortices which are present in the outer viscous layer are drawn schematically.

a direction opposite to the deformation of the outer interface. Due to this mechanism the layer $V^{(1)}$ is thicker at the tops of the drop ($\bar{x}_2 = 0$) and thinner in the middle part of the drop ($\bar{x}_1 = 0$). The steady-state deformation of a drop where $V^{(1)}$ consist of a viscoelastic I material with $c_1 = 80$ differs substantially from a viscous drop as can been seen in figure 7-1(b). In this figure the velocity field is not plotted as it is zero in the steady state situation. Due to the elastic nature of the material, there is almost no variation of the thickness of the layer $V^{(1)}$.

Using grid refinement we established that the order of accuracy for the two layer drop is the same as for the simple drop, i.e. second-order in space and first-or second-order in time, depending on the time integration method used. To validate the results for a drop consisting of two viscous layers we use small deformation results obtained by Stone and Leal [13]. The theory leading to these results is based on the work of Taylor [8] for simple drops and shows strong resemblance with the theories discussed in the previous chapter (section 6.1). In this case, we obtain expressions for the amplitude of the radial displacement of both interfaces from which the deformation can be derived. In figure 7-2, we plot the analytical and numerical steady-state deformation

of both interfaces as a function of the initial shell thickness $\kappa^{(1)}$ at $C = 0.025$. The numerical results were generated with 32 boundary elements along both interfaces and no internal cells since a domain integral is not present in this particular case. In the figure we also plot the steady-state shapes of the drop

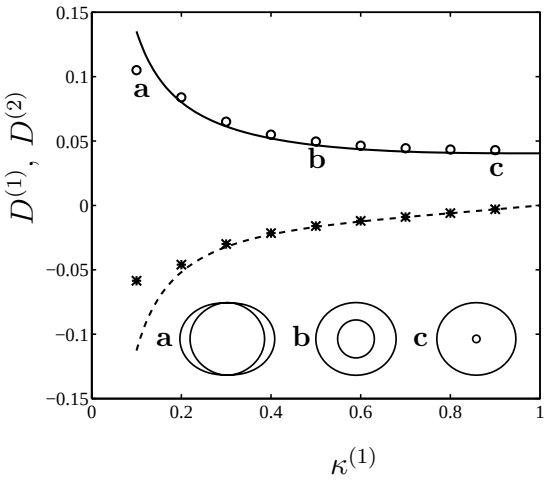

Figure 7-2: Steady-state deformation of a two layer viscous drop with $\lambda^{(1)} = \lambda^{(2)} = 1$ at $C^{(1)} = 0.025$ versus the initial interface thickness $\kappa^{(1)}$. The circles and crosses represent the numerically obtained deformations of the inner and outer interface respectively. The solid and dashed lines display the corresponding analytical results. The steady-state configurations for $\kappa^{(1)} = 0.1$, $\kappa^{(1)} = 0.5$ and $\kappa^{(1)} = 0.9$ are also contained in the plot.

for three different values of the thickness $\kappa^{(1)}$. The numerical and analytical results are in excellent agreement for small deformations. For larger deformations, i.e. smaller $\kappa^{(1)}$, there are some differences which can be attributed to the limited validity of the linear theory.

The results for a compound drop consisting of a viscous inner layer and a viscoelastic I outer layer are validated using analytical first-order results by Brunn [12]. In this theory the Navier-Stokes and Navier equations are used to describe the displacement fields of the viscous and elastic layer respectively. The derivation of the amplitude of the radial displacement of both interfaces is analogous to the theories mentioned above. In figure 7-3 we plot the analytical and numerical results for the steady-state deformation as a function of the initial thickness of the viscoelastic I layer with $c_1/\eta G = 80$. In order to keep the aspect ratio of the internal cells limited, we used different grids for

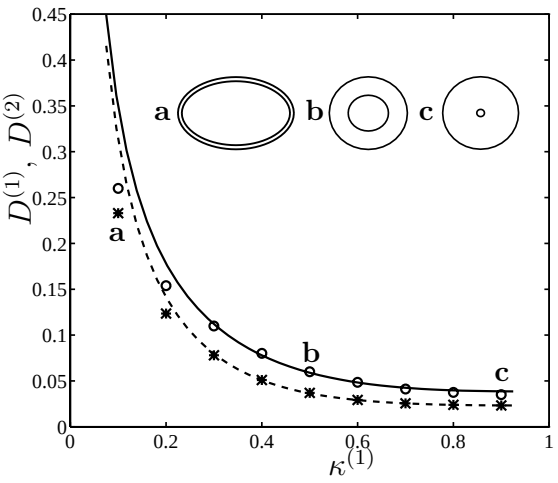

Figure 7-3: Steady-state deformation of a two-layer drop with a viscous interior $\lambda^{(2)} = 1$ and a viscoelastic ($\lambda^{(1)} = 1$, $c_1/\eta G = 80$ and $c_2/\eta G = 0$) outer layer versus the initial thickness $\kappa^{(1)}$ of the viscoelastic layer. The circles and crosses represent the numerically obtained deformations of the inner and outer interface respectively. The solid and dashed lines display the corresponding analytical results. The steady-state configurations for $\kappa^{(1)} = 0.1$, $\kappa^{(1)} = 0.5$ and $\kappa^{(1)} = 0.9$ are shown at the inset.

different values of $\kappa^{(1)}$ (e.g $N_b^{(1)} = N_b^{(2)} = 32,\ N_c^{(1)} = 160$ for $\kappa^{(1)} = 0.1$ and $N_b^{(1)} = N_b^{(2)} = 16,\ N_c^{(1)} = 256$ for $\kappa^{(1)} = 0.9$). It is seen that, similar to a completely viscous two-layer drop, the numerical and analytical results are in good agreement for small deformations. Additional computations performed for higher values of c_1 (i.e. smaller deformations) lead to smaller differences at $\kappa^{(1)} = 0.1$ indicating that the discrepancies are due to the limited validity of the linear theory. In figure 7-3 we also plotted the shapes of the drop for several values of $\kappa^{(1)}$. From these plots, it is seen that the interfaces deform uniformly for all $\kappa^{(1)}$.

We can conclude that the numerical method gives correct results for a two-layer (non-)Newtonian drop. In the next section, we discuss several breakup mechanisms for compound non-Newtonian drops.

7.2 Breakup mechanisms

In this section, we survey the applicability of several different breakup mechanisms for compound drops. Before turning towards compound drops we first

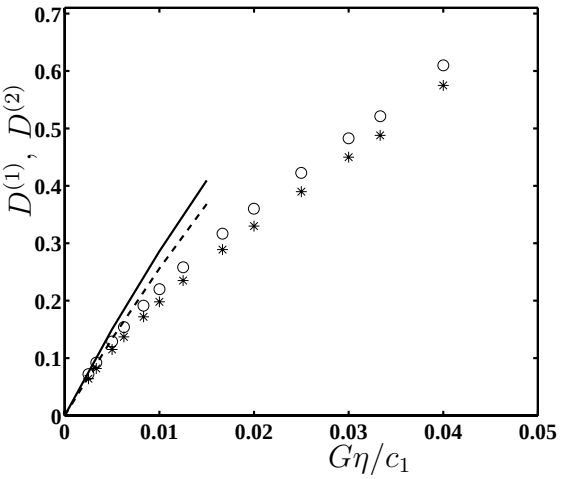

Figure 7-4: Steady-state deformation of a two layer drop with a viscous interior $\lambda^{(2)} = 1$ and a viscoelastic-I outer layer ($\lambda^{(1)} = 1$, $\kappa^{(1)} = 0.1$) versus the ratio between the viscous and elastic forces. The circles and asterisks represent the numerically obtained deformations of the inner and outer interface, respectively. The solid and dashed lines display the corresponding analytical results.

discuss the definition of the breakup mechanism used in the literature.

If an initially spherical simple viscous drop is placed in a steady flow, the drop deforms and reaches a steady-state if the capillary number is small enough. In this steady-state situation, the viscous and pressure forces exerted by the flow are compensated by the interfacial tension. In case of a viscoelastic-I or II drop, the viscous forces are compensated by the elasticity of the inner material. Beyond a certain critical capillary number, the drop begins a transient elongation and thus will not attain a steady state. The term "breakup" often refers to this condition, although the actual fragmentation is rarely discussed in literature (Stone [6]). For a simple viscoelastic drop a similar critical ratio of the viscous and elastic forces can be identified (see also figure 6-5).

In case of a compound drop, several breakup mechanisms can be identified. The first mechanism is similar to the one discussed above and states

that there exists a critical ratio of the viscous and interfacial tensions or a critical ratio of the viscous and elastic tensions beyond which no steady-state exists. The second and third mechanisms include breakup due to an excessive thinning of the outer layer or the presence of an excessive stress in the outer layer (Pozrikidis [40]). The second mechanism is dominant for viscous com-

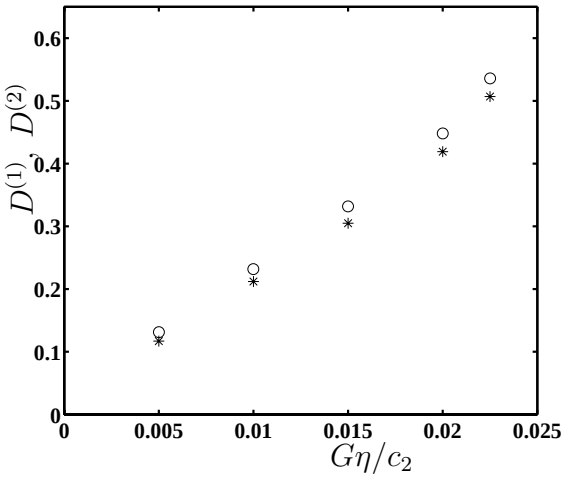

Figure 7-5: Steady-state deformation of a two layer drop with a viscous interior $\lambda^{(2)} = 1$ and a viscoelastic-II outer layer ($\lambda^{(1)} = 1$, $\kappa^{(1)} = 0.1$) versus the ratio between the viscous and elastic forces. The circles and asterisks represent the numerically obtained deformations of the inner and outer interface respectively.

pound drops where the thickness of the outer layer can vary strongly along the interface as is seen in figures 7-1(a) and 7-2 of the previous section. The shapes in figure 7-2 clearly show that breakup can already occur for very small deformations of the outer interface, as was also remarked by Stone and Leal [13]. This implies that breakup can occur at a capillary number which is significantly lower than the corresponding critical capillary number. The third mechanism, excessive tension is especially relevant when the outer layer of the drop has a lipid bi-layer structure such as a vesicle or red blood cell (Lacell et al. [42]). For a compound drop having a viscoelastic outer layer the breakup mechanism due to contact of the interfaces is not relevant since the thickness of this layer remains essentially constant throughout the deformation process (see figure 7-3). In the remaining part, we discuss which breakup mechanism is most applicable for viscoelastic compound drops.

To study whether a breakup mechanism based on a critical ratio of the

viscous and elastic forces is relevant, we consider a two-layer drop with a viscous inner core and a viscoelastic-I outer layer. The relative thickness κ of this outer layer is chosen to be 0.1. In figure 7-4 we have plotted both the numerical and analytical steady-state deformation as a function of the ratio $G\eta/c_1$. The numerical results were generated using 32 boundary elements along both interfaces and 160 internal cells. It is seen that, similar to the results found in section 7.1, the numerical and analytical results are in good agreement for small deformations. For larger deformations the compound drop is deforming almost linearly with $G\eta/c_1$. From figure 7-4 no critical ratio $G\eta/c_1$ can be identified, although it is expected that such a critical ratio exists as was the case for a simple viscoelastic-I drop (section 6.1). For a two-layer drop consisting of a viscous inner core and viscoelastic-II outer layer, we can identify a critical ratio $G\eta/c_2$ as is seen in figure 7-5. Further computations indicate that the compound drop does not adopt a steady shape if $G\eta/c_2$ is larger than about 0.023.

In order to study the breakup due to the presence of an excessive stress in the outer layer we introduce the Mises yield condition (Malvern [83]):

$$f(\pi_{ij}) \equiv II_{\pi'_{ij}} - k^2 = 0, \tag{7-1}$$

where k is an adjustable parameter and $II_{\pi'_{ij}}$ is the second invariant of the traceless total stress π'_{ij}:

$$II_{\pi'_{ij}} = \frac{1}{6}\left\{(\pi_{11}-\pi_{22})^2 + (\pi_{22}-\pi_{33})^2 + (\pi_{33}-\pi_{11})^2\right\} + \tau_{12}^2 + \tau_{13}^2 + \tau_{23}^2. \tag{7-2}$$

To use (7-1) as a breakup mechanism we postulate that the material fails if $f(\pi_{ij}) = 0$ in any point. Since we do not know the value of k we cannot predict the exact breakup process in our situation. We can, however, identify areas in the material where the material is most likely to break by considering the distribution of $f(\pi_{ij})$ in the compound drop. In figure 7-6 we have plotted the distribution of the function $f(\pi_{ij})$ for several values of the ratio $G\eta/c_1$ within a viscoelastic-I layer which has reached its steady state shape. The distribution of this function indicates that breakup is likely to occur at the middle of the drop ($\bar{x}_1 = 0$). Observe that the value of $II_{\pi'_{ij}}$ is somewhat higher at the inside of the layer than at the outside of the layer. This implies that the viscoelastic-I layer will burst from the inside, if breakup is due to excessive stress.

In order to compare our numerical results with experiments, we consider the work by Chang and Olbright [84] who studied the deformation of a two-

layer compound drop subjected to a planar elongational flow. The compound drop they considered consists of a viscous Newtonian core encapsulated by a layer of crosslinked polymer. For small strains the rheological behavior of this polymer is adequately described by a rubber like material. For deformations smaller than 0.3, the results presented in figure 7-4 are qualitively in agreement with experiments performed by Chang and Olbright [84]. However, when $G\eta/c_1$ is increased further, they found only little additional deformation. Since there is no fluid motion in the membrane if the steady-state is reached, this behavior is probably caused by strain hardening of the polymeric material. This strain hardening behavior indicates that a breakup mechanism based on (7-1) is the most appropriate mechanism for compound viscoelastic drops. In order to incorporate strain hardening into our numerical method, more sophisticated rheological models have to be introduced.

7.3 Conclusions

The method for simulating a two-layer drop was numerically and physically validated in the first section of this chapter. The simulations performed for the numerical validation show that the numerical method used is second-order accurate in space. From the validation process it followed that the numerical results for the steady state behavior of a two-layer drop consisting of a viscous inner layer and a viscous or viscoelastic outer layer is in good agreement with analytical results available for small deformations. The thickness of a viscous outer layer varies strongly along the interface whereas the thickness of a viscoelastic layer remains almost uniform.

In the second part of this chapter, we studied three possible breakup mechanisms for a compound drop with a viscoelastic outer layer: a critical ratio of viscous and elastic forces, excessive thinning of the outer layer and a mechanism based on a critical stress. As the thickness of a viscoelastic layer remains almost uniform during the deformation process, a breakup mechanism due to excessive thinning is not relevant for viscoelastic layers. For a compound drop with a viscoelastic-II layer, we found that no steady shape exist beyond $G\eta/c_2 = 0.023$. However, if a compound drop exhibits strain hardening behavior, this mechanism is not valid. From the breakup mechanism based on the presence of a critical stress in the viscoelastic layer, it appeared that drops fail at the inside of the layer. Although the latter mechanism does not predict a specific critical value for $G\eta/c_1$ or $G\eta/c_2$, it remains valid for strain hardening materials.

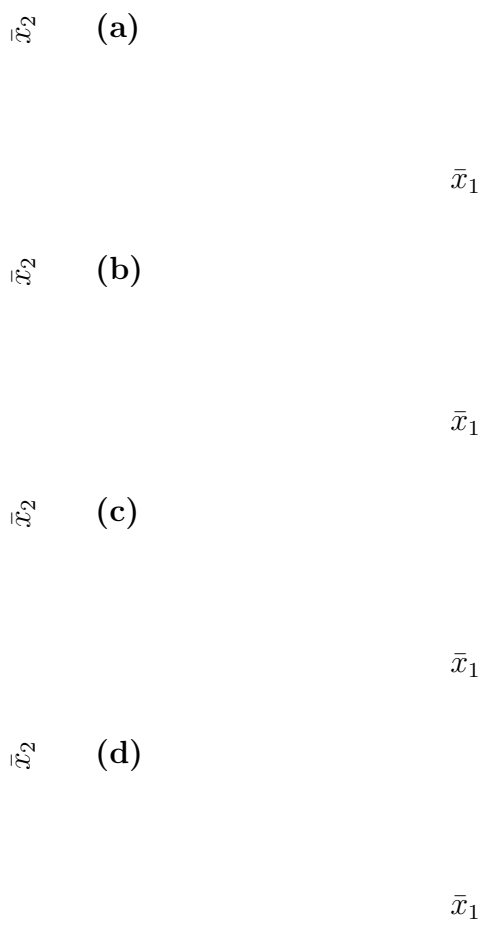

Figure 7-6: Distribution of $II_{\pi'_{ij}}$ within the viscoelastic-I outer layer ($\lambda^{(1)} = 1$, $\kappa^{(1)} = 0.1$) of a two-layer drop with a viscous interior $\lambda^{(2)} = 1$. The ratio $G\eta/c_1$ is 0.01, 0.02, 0.03 and 0.04 for the figures 7-6(a), 7-6(b), 7-6(c) and 7-6(d) respectively. The colorbar on the right-hand side indicates the values of the stress levels in the different figures.

Chapter 8

Dispersions

In the previous two chapters we observed that the boundary-integral method developed in this thesis is well suited for simple and compound non-Newtonian drops. In section 4.4, we showed that the boundary-integral method can readily be extended to a dispersion of drops through the introduction of periodic Green's functions. In this chapter we consider a dispersion of two dimensional Newtonian drops as a first step towards studying a dispersion of non-Newtonian drops. In the first section of this chapter we discuss the calculations performed to validate the numerical method for a periodic dispersion of drops. In section 8.2, we show some typical examples of dispersions of drops at different capillary numbers and perform a study of the effect of the number of drops on the macroscopic properties of the dispersion. In particular, we establish essential non-Newtonian behavior in a dispersion containing only Newtonian fluids. In this last part of section 8.2 we focus on the determination of the minimum number of drops needed for a reliable simulation. The effect of the volume fraction on the steady-state behavior which was found in section 8.2 is discussed in more detail in section 8.3. Finally in 8.4, we summarize our findings and formulate some conclusions.

8.1 Validation

In this section, we present a mathematical validation of the implementation of the numerical method as described in chapter 5. As the calculation of the Green's functions is the basis for our method, we validated the interpolation process separately from the rest of the method. Besides checking whether the calculated properties converge to their exact values when refining the grid or reducing the time-step, we will also check the order of accuracy.

The mathematical validation of the interpolation process is based on a comparison of the interpolated functions with the exact values. The residual

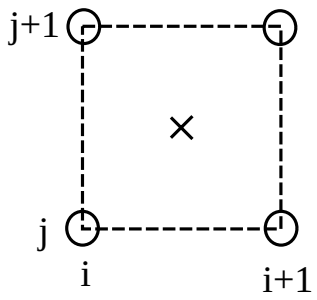

Figure 8-1: Schematic representation of the points used for the calculation of the residual in (8-1) for $n_{tab} = 1$. The interpolation grid is indicated by the circles, whereas the staggered grid is represented by the cross.

should converge to zero when the table size is increased. This residual is defined as the deviation between the exact and interpolated Green's functions in all the "staggered" nodes, i.e. $(i + 1/2, j + 1/2, k + 1/2)$. In figure 8-1 a schematic representation of the points used in the calculation is drawn. For clarity, we have only represented two interpolation directions. The residual $\mathcal{R}_{n_{tab}}$ is defined as the discrete L_2-norm:

$$\mathcal{R}_{(n_{tab})} = \left\{ \frac{1}{N_s} \sum_{i,j,k} |J(\boldsymbol{x}_{i+1/2,j+1/2,k+1/2}) - \hat{J}(\boldsymbol{x}_{i+1/2,j+1/2,k+1/2})|^2 \right\}^{1/2} \tag{8-1}$$

where n_{tab} is the number of intervals per tabulation direction, J is the interpolated Green's function and $\hat{J}$ the exact value. Furthermore, N_s denotes the number of points of the staggered grid. The residuals for tabulation boxes refined with a Romberg sequence are listed in table 8-1. From the convergence rates $\rho_{(i)}$, also shown in table 8-1, we can conclude that the interpolation process is second-order accurate in the tabulation refinement (see section 6.1). These results hold for J_{11} as well as for the other components of the periodic Green's function. In the numerical simulation presented in this chapter we use $n_{tab} = 32$, since a further increase of the number of intervals per tabulation direction has no significant effect on the results.

i	n_{tab}	$\mathcal{R}_{(n_{tab})}$	$\rho_{(i)}$
1	4	0.03140671	3.8
2	8	0.00818378	4.0
3	16	0.00206570	-
4	32	0.00051811	-

Table 8-1: Results of refinement in tabulation spacing for J_{11}

For the mathematical validation of the overall numerical method we performed grid and time-step refinement studies. To that end, we focussed on the numerically obtained values of the deformation $D(t_0)$ of one drop in a periodic system at a certain time t_0. In table 8-2, typical grid refinement results using a Bulirsch sequence are listed for a suspension containing two drops per periodic cluster with $C = 0.1$, a constant (Euler forward) time-step $\Delta t = 10^{-4}$ and $n_{tab} = 32$. In order to minimize the effects of the time stepping scheme, we considered the deformation at $t = 0.005$ at two different values of λ. The values of the convergence rate $\rho_{(i)}$, also listed in table 8-2, imply a third order accurate method in space for this specific case.

i	n	$D(t_0); \lambda = 1.0$	$\rho_{(i)}$	$D(t_0); \lambda = 0.5$	$\rho_{(i)}$
1	16	1.0024763	3.9	1.00288795	3.7
2	24	1.00248155	1.9	1.00289671	1.9
3	32	1.00248288	4.1	1.00289910	4.1
4	48	1.00248356	-	1.00290035	-
5	64	1.00248373	-	1.00290067	-

Table 8-2: Grid refinement results: $N = 2, C = 0.1, \Delta t = 10^{-4}$ (Euler), $n_{tab} = 32, t = 0.005$

Table 8-3 shows typical time-step refinement results, using a Romberg refinement, for a forward Euler time-integration scheme. The results correspond to a suspension of two drops per cluster with $C = 0.1$ and the same tabulation box as above. In order to incorporate the effect of the grid redistribution scheme we consider the deformation at $t_0 = 0.1$, again at two values of λ. At each refinement the time-step was kept constant. The values of ρ_i imply a first-order accurate method in time for this specific case when using an Euler forward time integration scheme. Under the same conditions, a time-

i	$\triangle t$	$D(t_0); \lambda = 1.0$	$\rho_{(i)}$	$D(t_0); \lambda = 0.5$	$\rho_{(i)}$
1	0.02	1.04413493	2.0	1.04880050	2.5
2	0.01	1.04408596	2.0	1.04881264	2.3
3	0.005	1.04406117	2.0	1.04881751	2.1
4	0.0025	1.04404874	-	1.04881967	-
5	0.00125	1.04404251	-	1.04882072	-

Table 8-3: Time-step refinement results (Euler): $N = 2, C = 0.1, n_{tab} =$ 32, 32 grid points per drop, $t_0 = 0.1$

step refinement study has been performed for the compact storage four stage Runge-Kutta scheme. The results imply a second order accuracy in time using this time integration scheme.

Although the total volume A_{tot} of all drops in one periodic cell is analytically conserved, it is not a conserved quantity in our numerical method. Therefore, the change in A_{tot} is also an indication of the accuracy of the numerical method. In case of the Euler forward time integration, we found that the change in the total drop volume stays 1% over a time period of 10 only for very small time steps, say $\Delta t < 0.0001$. In the case of the compact-storage four-stage Runge-Kutta scheme timesteps of 0.05 still give very good results (i.e. less than 1% over a time period of 10).

8.2 Transient behavior and macroscopic properties

In this section, we show some typical examples of a dispersion of drops at different capillary numbers. The viscosity ratio of all drops in the dispersion is equal to one. In figure 8-2 we have plotted the initial configuration of a dispersion of 24 drops with a volume fraction $\phi = 0.2$. In this figure nine periodic cells are drawn in order to emphasize the effect of the periodicity. The periodic cell is indicated by the dashed box in the middle of the figure. As soon as we apply an external velocity field to this dispersion, the drops deform and move in the direction of the flow while sensing their mutual hydrodynamic interaction. In figure 8-3(a), we have plotted the configuration at $t = 6$ of the same dispersion as described above at a capillary number of $C = 0.2$. It is seen that the drops are slightly deformed due to the external velocity field. At higher capillary numbers the drops, deform further as is seen in figure 8-3(b) where we plotted the configuration at $t = 6$ at a capillary number of 0.75. It

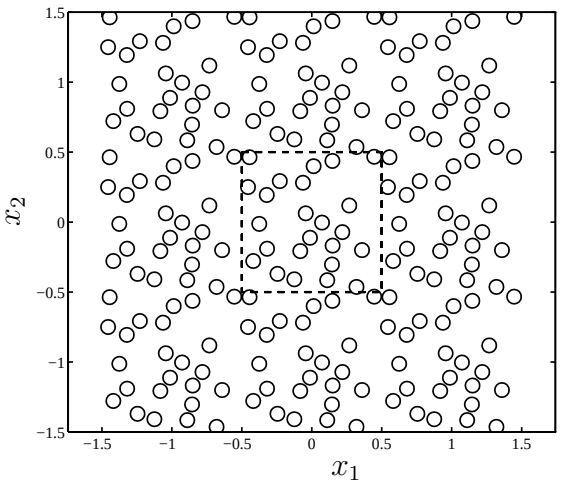

Figure 8-2: The initial configuration of a dispersion of 24 drops ($\lambda = 1$) with a volume fraction of 0.2.

is noted that, although the majority of the drops are more deformed at higher capillary numbers, there also remain several nearly spherical drops in this dispersion. The existence of a wide variation in the morphology and deformation of the drops is caused by interactions between drops in the dispersion. From this and further simulations, we may also conclude that the diversity in the deformation and orientation of the drops increases with an increasing volume fraction of the drops.

For the dispersions discussed above, several macroscopic properties can be calculated during the simulation (see subsection 2.3.2 for details on the calculation). In figure 8-4(a) we have plotted the effective viscosity of a dispersion with a volume fraction 0.2 at a capillary number of 0.2 and 0.75. One of the first things noted in figure 8-4(a) is the relatively strong fluctuation in the viscosity as a function of time. These fluctuations are due to the temporal evolution of the shape and orientation which is caused by interactions between the drops in the dispersion. It is further noted that the viscosity at $C = 0.75$ is much lower than the viscosity at $C = 0.2$. The reason for this phenomenon is that the drops at $C = 0.75$ are more aligned in the direction of the flow compared to the situation at $C = 0.2$ (see figures 8-3(a) and 8-3(b)). This implies that the drops can move more freely past each other at $C = 0.75$ leading to a lower viscosity and less fluctuations. Due to the stretching of the drops in one direction, energy is stored into the system giving rise to normal stresses in the

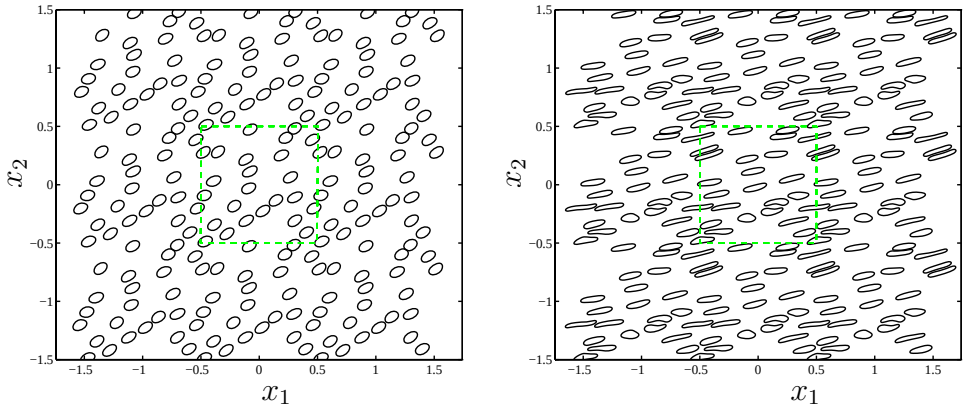

(a) C=0.2 (b) C=0.75

Figure 8-3: Snapshot of the configuration of a dispersion of 24 drops at $t = 6$. The volume fraction of the dispersion is 0.2 and $\lambda = 1$

dispersion. As the drops are further elongated at larger capillary numbers, the normal stress increases with C as is seen in figure 8-4(b). In the next section we perform a more systematic study of these phenomena.

As can be inferred from figure 8-4, the macroscopic properties vary quite rapidly in time and appear to converge to a statistically stationary value as $t \to \infty$. In order to find the mean value corresponding to this signal, we determine the time-averaged value:

$$\hat{f} = \lim_{t_1 \to \infty} \frac{1}{t_1} \int_{t_s}^{t_s+t_1} f(t')dt' \approx \frac{1}{T} \int_{t_s}^{t_s+T} f(t')dt',$$

where $f(t)$ is a certain macroscopic property and $\hat{f}$ its average value. Moreover, T is a sufficiently large time interval, much longer than the characteristic time-scale of the fluctuations in the signal. In practice we found $T = 15$ appropriate and used $t_s \approx 15$ in order not to include transient behavior. Note that the total simulation time in this situation is equal to 30. Li et al. [30] used a total simulation time of 60, whereas T is chosen equal to 4. The relative low value of T used is appropriate for low and intermediate values of C ($C < 0.3$). For higher values of the capillary number larger values are needed as is seen in figure 8-4.

Although the averaging method described above gives reliable results for each periodic system considered, certain questions concerning the finite system

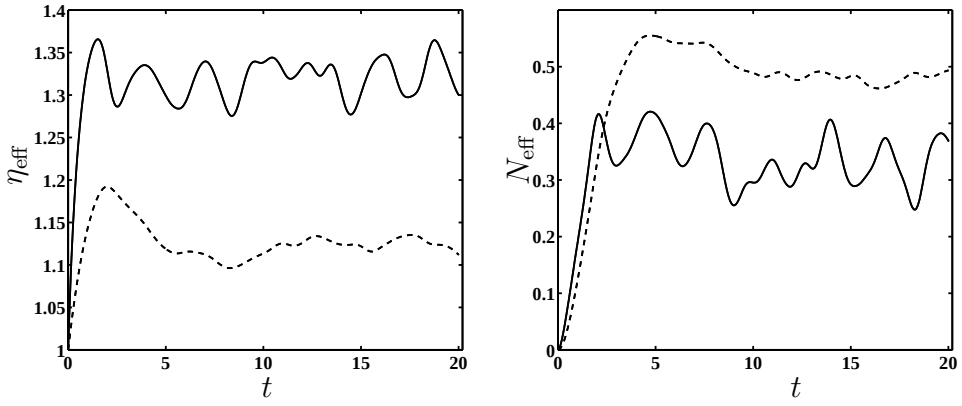

(a) Viscosity (b) Normal stress

Figure 8-4: Effective shear viscosity and normal stress of a dispersion of 24 drops with $\phi = 0.2$. The solid and dashed line represent the specific property at $C = 0.2$ and $C = 0.75$ respectively.

size are raised. First of all there, is the question what is the effect of the periodicity and secondly what is the effect of the number of drops within one periodic box on the predicted rheological properties.

These questions are closely related, but we try to answer them separately by considering two different situations. To study the first question we consider a single drop placed in a periodic box. The periodic box is chosen as a square with a side of length L_b in all simulations. By varying the ratio between the size of the drop and the box size L_b, the effect of the periodicity can be studied. This effect is measured by considering the relative deviation of the effective viscosity $\Delta\eta_{\text{eff}}$ compared to the infinite dilution limit:

$$\Delta\eta_{\text{eff}} = \eta_{\text{eff}}/\eta^*_{\text{eff}} - 1,$$

where η^*_{eff} is the effective viscosity as computed with (2-28). In figure 8-5(a) we have plotted the time-averaged $\Delta\eta_{\text{eff}}$ versus a/L_b. In this figure we observe that the effective viscosity converges towards its value of the infinitely diluted system. At higher values of a/L_b the drop is more influenced by its nearby periodic replica, which gives rise to deviations. For the effective normal stress, similar results were obtained, although the deviation was significantly larger (about 15% at $a/L_b = 0.25$). The reason for this larger deviation is the fact that the normal stress is very sensitive to variations in the elongation of the drop, and thus strongly influenced by its nearby periodic replica.

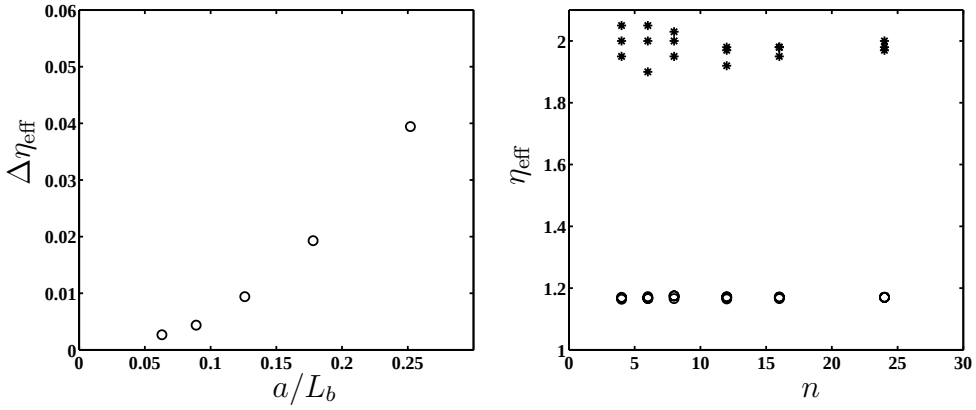

(a) Constant n (b) Constant ϕ

Figure 8-5: Effects of the finite system size on the effective viscosity. In 8-5(a) a single drop is considered, whereas in 8-5(b) a dispersion with $\phi = 0.1$ ($\circ$) and $\phi = 0.4$ ($*$) is considered.

The second question is studied by considering a situation where we increase the number of drops in the box. To minimize the effects of the periodicity, the drops are chosen sufficiently small compared to the box size. In figure 8-5(b) we have plotted the time-averaged effective viscosity of two dispersions with $\phi = 0.1$ and $\phi = 0.4$ respectively at $C = 0.1$ and used n drops in the periodic box. To study the effect of the initial distribution of the drops we performed each simulation with three different initial configurations. In this figure it is seen that the rheological properties for a dispersion with $\phi = 0.1$ remain nearly constant if the periodic box contains at least four drops. For $\phi = 0.4$ about 8 drops are needed to obtain reliable results. We observe that if the concentration increases the variations in η_{eff} increase as well due to the increased hydrodynamic interactions. Moreover, as the length of a drop increases with the capillary number, more drops are needed if one wishes to address higher capillary numbers. In order to be on the safe side, we choose the number of drops equal to 24 in the next section.

8.3 Steady-state results

In this section we consider the effect of the volume fraction on the steady-state macroscopic properties of a dispersion of drops with a viscosity ratio of

one. The numerical results presented in this section were generated with a dispersion of 24 drops. The number of boundary elements along the boundary of one drop varies for the different capillary numbers and concentrations. The simulations for the curve $\phi = 0.4$ were performed with 24 elements along the boundary. For the other curves we used 24 elements at very high or low capillary numbers (i.e. $C < 0.05$ and $C > 0.5$ respectively) and 16 elements for moderate values of C.

In figure 8-6 we have plotted the effective shear viscosity of a dispersion of drops as a function of the capillary number for four different concentrations. In this figure we have also plotted numerical results by Li et al. [30], which are

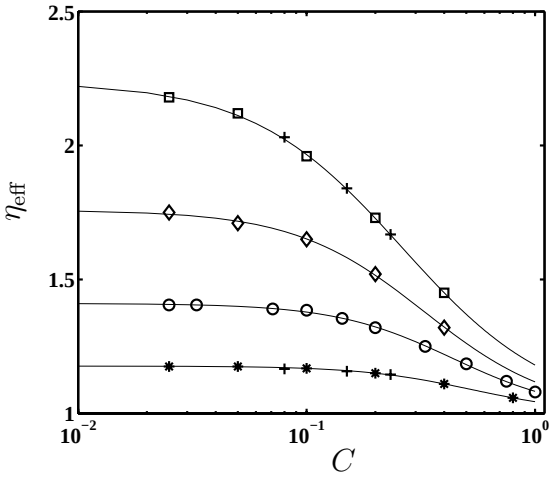

Figure 8-6: Effective viscosity of a dispersion of drops with $\lambda = 1$ at different concentrations. The concentrations $\phi = 0.1$, $\phi = 0.2$, $\phi = 0.3$ and $\phi = 0.4$ are indicated by the symbols $*$, $\circ$, $\diamond$ and $\square$ respectively. The solid lines give the corresponding function (8-2). The pluses are numerical results by Li et al. [30].

in good agreement with our results. In figure 8-6, we clearly see a Newtonian plateau at low capillary numbers. As the effective viscosity cannot be lower than that of the suspending fluid ($\lambda = 1$), another plateau must be present at high capillary numbers. Between these plateaus a strong shear-thinning region is visible. This clearly demonstrates the occurrence of non-Newtonian behavior in a dispersion composed of Newtonian fluids only. In order to get an estimate for the value of the Newtonian plateau at $C = 0$, we fit the data

in figure 8-6 with the function (Sugiura [85]):

$$\eta_{\text{eff}} = 1 + \frac{\eta_0 - 1}{1 + \beta C^{\alpha}}, \tag{8-2}$$

where η_0 is the zero-shear-rate viscosity, i.e. the viscosity at $C = 0$, and α and β are fit parameters. Equation (8-2) is merely used to find the zero-shear-rate viscosity and has no physical meaning in the context of this section. Using a somewhat different function for (8-2) we found very small deviations of the zero-shear-rate viscosity at the higher volume fraction only (less than 1%). In figure 8-6 the least-squares fitted functions at the different concentrations are indicated by the solid lines. Repeating this, rather time consuming, procedure could provides the zero-shear-rate viscosity at different viscosity ratios.

In case $\lambda = \infty$ the zero-shear-rate viscosity can be approximated relatively simply. In this situation, the drops can be seen as solid particles. As the drops are solid, the interface will not deform, implying that the integral on the right hand side of (4-52) is zero, even if C approaches zero. By assuming that an initially homogeneous distribution of drops remains homogeneous throughout the simulation, the viscosity calculated at $t = 0$ coincides with the zero-shear-rate viscosity. In the calculation of the zero-shear-rate viscosity, we used $\lambda = 1000$ as a very good approximation for solid particles. Besides this numerical approximation we can also obtain an analytical estimate for the zero-shear-rate viscosity. In the analytical approach two approaching solid drops, as shown in

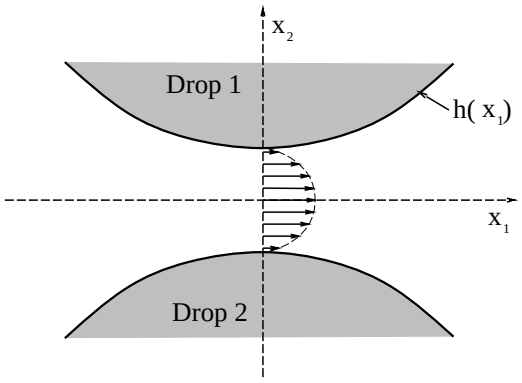

Figure 8-7: Schematic representation of two approaching drops and the squeezing flow between them. The shape of the drops is approximated by the function $h(x_1)$ as indicated in the figure.

figure 8-7, are considered and the contribution of the squeezing flow between

the drops to the dimensionless viscosity is calculated using lubrication theory (Van den Ende [86], Frankel and Acrivos [87]):

$$\eta_{\rm sq} = \frac{N_{nn}\phi_m}{8\pi} F_{sq} \left\{ \left(\frac{\phi_m}{\phi} \right)^{1/2} - 1 \right\}^{-3/2}, \tag{8-3}$$

with N_{nn} the number of nearest neighbors and ϕ_m the maximum concentration. For a system of randomly distributed non-overlapping circular disks ϕ_m is equal to 0.82 (Kausch et al. [88]). The number of nearest neighbors is taken equal to 5.5 in the evaluation of (8-3). In (8-3) $F_{\rm sq}$ is the dimensionless force needed to move the drops to each other:

$$F_{\rm sq} = \int_0^\infty x_1 \left\{ \frac{3x_1}{h^3} + \frac{\epsilon}{h^3} \left[-\frac{3}{10}(2\partial_1 h + x_1 \partial_{11} h) + \frac{42}{10} x_1 (\partial_1 h)^2 \right] \right\} dx_1,$$

where $h(x_1)$ is a function describing the shape of the drop in the gap and $\epsilon = h_0/a$, with h_0 half the nearest distance between the drops (see figure 8-7). The resulting squeezing viscosity $\eta_{\rm sq}$ is first order accurate with respect to ϵ. This implies that $\eta_{\rm sq}$ is a reasonable approximation for high concentrations only. In order to get the viscosity right, we consider the stream function $\mathcal{S}$ for a single solid drop placed in a shear flow (Van den Ende [86]):

$$\mathcal{S} = \frac{1}{4} G a^2 \left\{ s^2 - \frac{x_1^2 - x_2^2}{x_1^2 + x_2^2} \left(s^2 - 2 + s^{-2} \right) \right\}$$

with $s^2 = (x_1^2 + x_2^2)/a^2$. By calculating the velocity and pressure fields from this expression and using (2-23), we obtain $1+2\phi$ as a first order approximation for the viscosity at low concentrations. Adding this to the squeezing viscosity we obtain:

$$\hat{\eta}_0 = 1 + 2\phi + \eta_{\rm sq}, \tag{8-4}$$

where $\hat{\eta}_0$ denotes the analytical estimate for the zero-shear-rate viscosity. This expression is most accurate at low ϕ values and at ϕ values near the maximum concentration ϕ_m. In between, we have an order of magnitude estimate as can be observed from the difference between the zero order and first order calculation of the squeezing viscosity.

The values of the zero-shear-rate viscosity of a dispersion of drops with $\lambda = 1$ and $\lambda = 1000$ are plotted in figure 8-8. In this figure we observe that numerical and analytical results for the zero-shear-rate viscosity of a dispersion of drops at $\lambda = 1000$ are in good agreement with each other. From (8-4) we

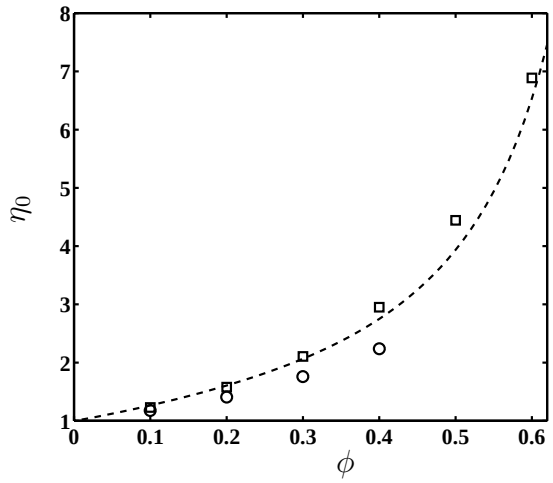

Figure 8-8: Zero-shear-rate viscosity of a dispersion of drops with $\lambda = 1$ ($\circ$) and $\lambda = 1000$ ($\square$). The dashed line represents the viscosity of a dispersion of drops at $\lambda = \infty$ as calculated with (8-4).

find that the zero-shear-rate viscosity becomes unbounded at the critical ϕ_m. For a dispersion with $\lambda = 1$ it is not yet clear if the zero-shear-rate viscosity diverges at ϕ_m since the drops can deform which could lead to a bounded viscosity. Unfortunately the data presented in figure 8-8 are not sufficient to establish whether the zero-shear-rate viscosity remains bounded up to ϕ_m.

Besides the effective viscosity, one can also consider the effect of the concentration of the drops on the effective normal stress. In figure 8-9 we have plotted the effective normal stress of a dispersion of drops as a function of the capillary number for four different concentrations. In this figure we see that the normal stress is increasing with increasing capillary number, which is caused by the elongation of the drops in the direction of the flow. As the amount of elastic energy is increasing with increasing concentration, the normal stress is also increasing as a function of ϕ. In figure 8-9 it is seen that our numerical results at $\phi = 0.4$ differ substantially from those by Li et al. [30]. This difference is probably caused by the relatively short averaging time used in our simulation.

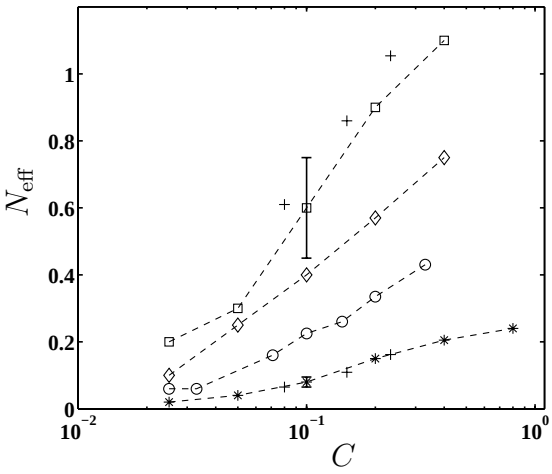

Figure 8-9: Effective normal stress of a dispersion of drops with $\lambda = 1$ at different concentrations. The concentrations $\phi = 0.1$, $\phi = 0.2$, $\phi = 0.3$ and $\phi = 0.4$ are indicated by the symbols $*$, $\circ$, $\diamond$ and $\square$ respectively. The dashed lines in the figure are merely used as visual guide-lines. The pluses are numerical results by Li et al. [30].

8.4 Conclusions

In the first section of this chapter the tabulation of the periodic Green's functions and the general numerical scheme for a periodic dispersion of two-dimensional Newtonian drops was validated numerically. This numerical validation showed a second-order accuracy of the interpolation process as a function of the tabulation refinement. Full numerical simulations of a dispersion of drops indicated that the method is third-order accurate in space and first-or-second order accurate in time, depending on the time integration scheme used. These accurate results give the opportunity to perform various experiments on the properties of concentrated dispersions of drops.

General exploratory results for a dispersion of drops were presented in section 8.2. The presented snapshots at $C = 0.2$ and $C = 0.75$ indicate a strong alignment and elongation of the drops in the direction of the flow which leads to large normal stresses in the dispersion. The dispersion exhibits besides the strong increase in normal stress, also a strong shear thinning behavior. This behavior is caused by the fact that the drops are more aligned at higher capillary number than at low capillary numbers. As the signal of the macroscopic properties is strongly fluctuating, a time-averaging method was used to find

the average value of a specific quantity. To study the influence of the finite system size on the macroscopic properties several tests were performed. It appeared that simulations with only 4 drops already can give quite good results, provided that the drops are small compared to the box size. This result is very promising with respect to the computational costs if one wishes to simulate a dispersion of non-Newtonian drops, or extend the method to three dimensions.

In section 8.3 the effect of the volume fraction on the mean rheological properties of a dispersion of drops with $\lambda = 1$ is studied. It appeared that the effective viscosity has two Newtonian plateaus at high and low capillary numbers respectively. In between there is a shear thinning region. By fitting these curves with an appropriate function the values for the zero-shear-rate viscosity were found. This viscosity is increasing more than linearly with the volume fraction, although the values found are lower than similar results for a dispersion of solid drops. The analytical and numerical results for the zero-shear-rate viscosity are in good agreement with each other. Finally, the normal stress was studied which showed a strong increase with an increase of either capillary number or concentration.

Chapter 9

Overview and perspectives

In section 1.3 the main goals of this thesis were formulated: to develop a boundary integral method for the simulation of non-Newtonian drops or vesicles subjected to a slow viscous flow and to study the effects of the non-Newtonian material on the deformation processes.

To develop a boundary integral method we noted that the Reynolds number at particle scale is very small for the situations we are considering (chapter 1). At low Reynolds number the velocity fields inside and outside the drop can be described by the so-called Stokes equations (chapter 2). In order to incorporate the non-Newtonian behavior of the drop a non-Newtonian stress tensor is introduced into the Stokes equations. In chapter 3 several constitutive equations were introduced which describe the time evolution of the non-Newtonian part of the stress tensor of dilute and concentrated polymer solutions. The models selected from literature are: the Oldroyd-B, FENE-P, CR a Mooney model. For the latter model we focussed on two specific sets of parameter setting, denoted with viscoelastic-I and II. Analyzing these models in an elongational flow we observed an unphysical behavior of the Oldroyd-B model for higher values of the Deborah number. Despite this shortcoming the Oldroyd-B model was used extensively in the numerical simulations since a large amount of analytical work has been done for this model (chapter 1).

To derive a boundary integral formulation for the velocity field we treated the non-Newtonian contribution as a source term, leading to a domain integral in the boundary integral representation of the velocity (chapter 4). To obtain a better connection with the matching conditions at the interface this domain integral was reformulated by applying Gauss' divergence theorem. Transforming the integral representation for the velocity to cylindrical coordinates and performing the integral over the azimuthal angle analytically we may re-

duce the dimension of the computational problem. The integral equation for the velocity remains of the same form and the Green's functions were explicitly transformed to cylindrical coordinates. To study the applicability of the method to multiple drops, we considered a two dimensional periodic dispersion of drops. It turned out that the periodicity of the problem could be simply included in the Green's functions, whereas the boundary integral formulation remained of the same form as for compound non-Newtonian drops. In chapter 5 the general numerical scheme used in the simulations was discussed. Due to the generality of the integral expression, the numerical schemes for the different problems also showed considerable similarities.

In chapters 6 and 7 the numerical method was validated and applied to simple and compound drops respectively. The validation showed that the numerical method which was developed is second order accurate in space and first or second order accurate in time depending on the time integration scheme used. The computational times for a non-Newtonian drop, however, are much longer compared to the Newtonian case due to the extra domain integral which appears in the formulation. From the physical validation process it was found that the numerical results for both simple and compound drops are in excellent agreement with analytical results known from literature and that strong nonlinear behavior is well captured by the method. The exploratory results presented in section 6.2 indicate that the steady state deformation of a simple drop subjected to a elongational flow is hardly influenced by the non-Newtonian character of the polymeric solution composing the drop. This outcome is in agreement with experiments performed with viscoelastic drops subjected to a planar elongational flow (Milliken and Leal [82]). In 7.3 we studied three possible breakup mechanisms for a compound drop with a viscoelastic outer layer: a critical ratio of viscous and elastic forces, excessive thinning of the outer layer and a mechanism based on a critical stress. As the thickness of a viscoelastic layer remains almost uniform during the deformation process a breakup mechanism due to excessive thinning is not relevant for viscoelastic layers. For a compound drop with a viscoelastic-II layer we found that no steady shape exist beyond $G\eta/c_2 = 0.023$. However, if a compound drop which exhibits strain harding behavior this mechanism is not valid. From the breakup mechanism based on the presence of a critical stress in the viscoelastic layer it appeared the drops fails at the inside of the layer. Although the latter mechanism does not predict a specific critical value $G\eta/c_1$ or $G\eta/c_2$, it remains valid for compound drops composed of strain harding materials.

Finally in chapter 8 we addressed a two-dimensional dispersion of Newtonian drops subjected to a shear flow. In this chapter the tabulation method

to calculate the periodic Green's function and the general numerical scheme were thoroughly validated. From this validation it was found that the method is third order accurate in space. Besides numerical tests, we also studied the influence of the finite system size on the macroscopic properties. From this study it appeared that, if the drops are small compared to the box size, only a few drops (e.g 4 to 8 drops at $\phi = 0.1$ to 0.4 respectively) are needed in the simulations. This result is very promising with respect to the computational costs if one wishes to simulate a dispersion of non-Newtonian drops. Snapshots of the dispersion with $\lambda = 1$ indicate that the drops are strongly aligned and elongated in the direction of the flow which leads to large normal stresses. The effective viscosity of this dispersion has two Newtonian plateaus at high and low capillary numbers respectively. In between there is a shear thinning region which is caused by the fact that the drops are more aligned at higher capillary numbers than at low capillary numbers. The value of the zero-shear-rate viscosity is strongly increasing with the volume fraction. The normal stresses of a dispersion also show a strong increase with an increase of either capillary number or concentration.

Concluding, we can remark that the boundary integral method developed in this thesis is well suited for simple and compound non-Newtonian drops although computational times are much longer than in the Newtonian case due to the domain integral that appears in the formulation. The advantage of the method over a more direct (finite difference) discretization of the Stokes equations lies in the fact that only the non-Newtonian layers of the drop have to be discretized and that calculations using relatively few points already give very accurate results. The boundary integral method is also more flexible and accurate with respect to modelling the boundary geometries. In case of thin layers the advantages of the method can be fully exploited since only a small part of the total flow domain has to be discretized. Conversely, the present method is not expected to be very efficient in case large regions of the flow-domain contain non-Newtonian material or if nonlinear terms cannot be neglected and the Navier-Stokes equations should be used. In such cases a finite difference or finite element method may be computationally cheaper. The application of the method to a dispersion of non-Newtonian drops looks very promising as only a small number of drops is needed in a simulation.

Although the method works fine for the cases presented in this thesis several recommendations for future research are to be made. First of all if the deformation of non-Newtonian drops becomes extreme special attention should be paid to retaining the grid sufficiently smooth and properly clustered. During extreme deformations the grid may become too skewed or stretched which

has a negative influence on the accuracy. In these cases the interpolation scheme used to find the non-Newtonian stress tensor on a new grid might also fail, implying the use of characteristic direction techniques. To improve the efficiency of the method we might use more efficient integration techniques or incorporate a dual reciprocity method which removes the need to evaluate the domain integrals with a cell-by-cell integration.

Apart from these improvements the present method can already be extended to many other interesting research areas such as the study of a dispersion of non-Newtonian drops and the inclusion of surfactants along the interface of the drop. The inclusion of Brownian motion and the simulation of a non-Newtonian drop in a fully three-dimensional (shear) flow, however, remain challenging problems for the near future.

Appendix A

Green's Functions

In this appendix we give the components of the transformed Green's functions in the expression for the integral representation of the velocity (4-41).

The non-zero components of the function $\bar{M}^{\beta}_{\alpha}(\bar{\boldsymbol{x}};\bar{y}_1)$ are given by:

$$\begin{aligned}
\bar{M}^1_{\ 1} &= E_{10} + \hat{x}_1^2 E_{30} \\
\bar{M}^1_{\ 2} &= \hat{x}_1 \bar{x}_2 E_{30} - \hat{x}_1 \bar{y}_2 E_{31} \\
\bar{M}^2_{\ 1} &= -\hat{x}_1 \bar{y}_2 E_{30} + \hat{x} \bar{x}_2 E_{31} \\
\bar{M}^2_{\ 2} &= E11 - \bar{x}_2 r_y E_{30} + (\bar{y}_2^2 + \bar{x}_2^2) E_{31} - \bar{x}_2 \bar{y}_2 E_{32} \\
\bar{M}^3_{\ 3} &= \frac{\bar{y}_2 E_{11} + \bar{x}_2 \bar{y}_2^2 E_{30} - \bar{x}_2 \bar{y}_2^2 E_{32}}{\bar{x}_2},
\end{aligned}$$

where $\hat{x}_1 = \bar{x}_1 - \bar{y}_1$ and E_{mn} given by:

$$E_{mn}(\hat{x}_1, \bar{x}_2, \bar{y}_2) = \frac{4k^m}{(4\bar{x}_2\bar{y}_2)^{m/2}} \int_0^{\pi/2} \frac{(2\cos^2\phi - 1)^n}{(1 - k^2\cos^2\phi)^{m/2}}\, d\phi,$$

with

$$k = 4\bar{x}_2\bar{y}_2/(\hat{x}^2 + (\bar{x}_2 + \bar{y}_2)^2).$$

The non-zero components of $\bar{W}^{\gamma\beta}{}_{\alpha}(\bar{\boldsymbol{x}};\bar{y}_1,\bar{y}_2)$ are given by:

$$
\begin{aligned}
W^{11}{}_{1} &= -\bar{x_1}E_{30} + 3\bar{x_1}^3E_{50} \\
W^{12}{}_{1} &= -\bar{x}_2E_{31} + 3\bar{x_1}^2\bar{x}_2E_{51} - 3\bar{x_1}^2\bar{y}_2E_{50} + \bar{y}_2E_{30} \\
W^{21}{}_{1} &= \bar{x}_2E_{31} + 3\hat{x}_1^2\bar{x}_2E_{51} - 3\hat{x}_1^2\bar{y}_2E_{50} - \bar{y}_2E_{30} \\
W^{22}{}_{1} &= -6\hat{x}_1\bar{x}_2\bar{y}_2E_{51} + 3\hat{x}_1\bar{x}_2^2E_{52} + 3\hat{x}_1\bar{y}_2^2E_{50} - \hat{x}_1E_{30} \\
W^{33}{}_{1} &= \left(-3\hat{x}_1\bar{x}_2^2E_{52} + 3\hat{x}_1\bar{x}_2^2E_{50} - \hat{x}_1E_{30}\right)\bar{y}_2^2 \\
W^{11}{}_{2} &= \bar{y}_2E_{31} - \bar{x}_2E_{30} - 3\hat{x}_1^2\bar{y}_2E_{51} + 3\hat{x}_1^2\bar{x}_2E_{50} \\
W^{12}{}_{2} &= \hat{x}_1E_{31} + 3\hat{x}_1(\bar{x}_2^2 + \bar{y}_2^2)E_{51} - 3\hat{x}_1\bar{x}_2\bar{y}_2E_{50} - 3\hat{x}_1\rho x\bar{y}_2E_{52} \\
W^{21}{}_{2} &= -\hat{x}_1E_{31} + 3\hat{x}_1(\bar{x}_2^2 + \bar{y}_2^2)E_{51} - 3\hat{x}_1\bar{x}_2\bar{y}_2E_{50} - 3\hat{x}_1\bar{x}_2\bar{y}_2E_{52} \\
W^{22}{}_{2} &= \bar{y}_2E_{31} - \bar{x}_2E_{30} - (3\bar{y}_2^3 + 6\bar{y}_2\bar{x}_2^2)E_{51} + 3\bar{x}_2\bar{y}_2^2E_{50} + \\
&\quad (3\bar{x}_2^3 + 6\bar{x}_2\bar{y}_2^2)E_{52} - 3\bar{x}_2^2\bar{y}_2E_{53} \\
W^{33}{}_{2} &= \left(\bar{y}_2E_{31} - \bar{x}_2E_{30} - 3\bar{x}_2^2\bar{y}_2E_{51} + 3\bar{x}_2^3E_{50} - 3\bar{x}_2^3E_{52} + 3\bar{x}_2^2\bar{y}_2E_{53}\right)/\bar{y}_2^2 \\
W^{13}{}_{3} &= \left(\hat{x}_1\bar{x}_2E_{31} - 3\hat{x}_1\bar{x}_2^2\bar{y}_2E_{52} + 3\hat{x}_1\bar{x}_2^2\bar{y}_2E_{50}\right)/\bar{y}_2 \\
W^{23}{}_{3} &= \left(-\bar{x}_2\bar{y}_2E_{31} + 3\bar{x}_2^2\bar{y}_2^2(E_{52} - E_{50})\bar{x}_2^2E_{30} + 3\bar{x}_2^3\bar{y}_2(E_{51} - E_{53})\right)/\bar{y}_2 \\
W^{32}{}_{3} &= \left(-\hat{x}_1\bar{x}_2E_{31} - 3\hat{x}_1\bar{x}_2^2\bar{y}_2E_{52} + 3\hat{x}_1\bar{x}_2^2\bar{y}_2E_{50}\right)/\bar{y}_2 \\
W^{33}{}_{3} &= \left(\bar{x}_2\bar{y}_2E_{31} + 3\bar{x}_2^2\bar{y}_2^2(E_{52} - E_{50})\bar{x}_2^2E_{30} + 3\bar{x}_2^3\bar{y}_2(E_{51} - E_{53})\right)/\bar{y}_2
\end{aligned}
$$

References

[1] P. Sherman, *Industrial rheology : with particular reference to foods, pharmaceuticals, and cosmetics.* Academic Press, London, 1970.

[2] H.A. Barnes, *Dispersion rheology 1980 : a survey of industrial problems and academic progress.* Unilever Research, 1981.

[3] H. Brenner, Suspension rheology. *Prog. Heat and Mass Transfer* 5 (1972) 104-122.

[4] W.B. Russel, D.A. Saville and W.R. Schowalter, *Colloidal Dispersions.* Cambridge University Press, Cambridge, 1989.

[5] J.M. Rallison, The deformation of small viscous drops and bubbles in shear flow. *Annu. Rev. Fluid Mech.* 16 (1984) 45-66.

[6] H.A. Stone, Dynamics of drop deformation and breakup in viscous fluids. *Annu. Rev. Fluid Mech.* 26 (1994) 65-102.

[7] Lord Rayleigh, On the capillary phenonema of jets. *Proc. Roy. Soc. (London)* 29 (1879) 71-97.

[8] G.I. Taylor, The viscosity of a fluid containing small drops of another fluid. *Proc. R. Soc. A.* 138 (1932) 41-48.

[9] G.I. Taylor, The formation of emulsions in definable fields of flow. *Proc. R. Soc. A.* 146 (1934) 501-523.

[10] R.G. Cox, The deformation of a drop in a general time-dependent fluid flow. *J. Fluid Mech.* 37 (1969) 601-623.

[11] D. Barthès-Biesel, Deformation and burst of a liquid droplet freely suspended in a linear shear field. *J. Fluid Mech.* 61 (1973) 1-21.

[12] P.O. Brunn, The deformation of a viscous particle surrounded by an elastic shell in a general time-dependent linear flow field. *J. Fluid Mech.* 126 (1983) 533-544.

[13] H.A. Stone and L.G. Leal, Breakup on concentric double emulsion droplets in linear flows. *J. Fluid Mech.* 211 (1990) 123-156.

[14] K. de Haas, *Rheology and deformation of dispersed lipid bilayer vesicles.* Ph. D. Thesis, University of Twente at Enschede, (1997).

[15] B.J. Bentley, *Drop deformation and burst in two-dimenional flows.* Ph. D. Thesis, California Institute of Technology, (1985)

[16] I. Delaby, B. Ernst and R. Muller, Drop deformation during elongational flow in blends of viscoelastic fluids; Small deformation theory and comparison with experimental results. *Rheol. Acta* 34 (1995) 525-533.

[17] H. Gramespacher and J. Meissner, Melt elongation and recovery of polymer blends, morphology, and influence of interfacial tension. *J. Rheol.* 41 (1997) 27-44.

[18] O. Reynolds, An experimental investigation of the circumstances which determine whether the motion of water shall be direct or sineous, and the law of resistance in parallel channels. *Phil. Trans. Roy. Soc.* (1883) 51-105.

[19] R.S. Rogallo and P. Moin, Numerical simulation of turbulent flows. *Annu. Rev. Fluid Mech.* 16 (1984) 99-137.

[20] L. Kleiser and T.A. Zang, Numerical simulation of transition in wall-bounded shear flows. *Annu. Rev. Fluid Mech.* 23 (1991) 495-538.

[21] K.S. Sheth and C. Pozrikidis, Effects of inertia on the deformation of liquid drops in simple shear flow. *Computers and Fluids* 24 (1995) 101-119.

[22] H. Lamb, *Hydrodynamics.* Dover, (1932).

[23] H.A. Lorentz, Eene algemeene stelling omtrent de beweging eener vloeistof met wrijving en eenige daaruit afgeleide gevolgen. *Versl. K. Akad. W. Amsterdam* 5 (1896) 168-175.

[24] N.J. Nersessian and H.F. Cohen, Selected works of H.A. Lorentz. Palm publications, Nieuwerkerk a/d IJssel, (1987).

[25] G.K. Youngren, A. Acrivos, Stokes flow past a particle of arbitrary shape: a numerical method of solution. *J. Fluid Mech.* 69 (1975) 377-403.

[26] M. Tjahjadi, H.A. Stone, J.M. Ottino, Satellite and subsatellite formation in capillary breakup. *J. Fluid Mech.* 243 (1992) 297-317.

[27] H.A. Stone and L.G. Leal, The effects of surfactants on drop deformation and breakup. *J. Fluid Mech.* 220 (1990) 161-186.

[28] X. Li and C. Pozrikidis, The effect of surfactants on drop deformation and on the rheology of dilute emulsions in Stokes flow. *J. Fluid Mech.* 341 (1997) 165-194

[29] X.Z. Li, D. Barthès-Biesel and A. Helmy, Large deformations and burst of a capsule freely suspended in an elongational flow. *J. Fluid Mech.* 187 (1988) 179-196.

[30] X. Li, R. Charles and C. Pozrikidis, Simple shear flow of suspensions of liquid drops. *J. Fluid Mech.* 320 (1996) 395-416.

[31] M. Loewenberg and E.J. Hinch, Numerical simulation of a concentrated emulsion in shear flow. *J. Fluid Mech.* 321 (1996) 395-419.

[32] M.B. Bush, J.F. Milthorpe and R.I. Tanner, Finite element and boundary element methods for extrusion computations. *J. Non Newt. Fluid Mech.* 16 (1984) 37-51.

[33] M.B. Bush, R.I. Tanner and P. Phan-Thien, A boundary element investigation of extrude swell. *J. Non-Newt. Fluid Mech.* 18 (1985) 143-162.

[34] R.B. Bird, R.C. Amstrong, O. Hassager, *Dynamics of polymeric liquids: Volume 1 fluid mechanics*. Wiley-Interscience, New-York, (1987).

[35] L.E. Scriven, Dynamics of a fluid interface, *Chem. Eng. Science* 12 (1960) 98-108.

[36] D. Barthès-Biesel, Role of interfacial properties on the motion and deformation of capsules in shear flow. *Physica A* 172 (1991) 103-124.

[37] V.G. Levich and V.S. Krylov, Surface-tension-driven phenonema. *Annu. Rev. Fluid Mech.* 1 (1958) 293-316.

[38] L.D. Landau and E.M. Lifshitz, *Theory of elasticity*. 2nd ed., Pergamon Press, 1970.

[39] D. Barthès-Biesel and J.M. Rallison, The time dependent deformation of a capsule freely suspended in a linear shear flow. *J. Fluid Mech.* 113 (1973) 251-267.

[40] C. Pozrikidis, Finite deformation of liquid capsules enclosed by elastic membranes in simple shear flow. *J. Fluid Mech.* 297 (1995) 123-152.

[41] W. Helfrich, Elastic properties of lipid bilayers: Theory and possible experiments. Z. Naturforsch. C, 28 (1973) 693-703.

[42] P.L. Lacell, E.A. Evans and R.M. Hochmutt, Erythocyte membrane elasticity, fragmentation and lysis. *Blood cells* 3 (1977) 335-350.

[43] J.F. Brady, Stokesian Dynamics. *Annu. Rev. Fluid Mech.* 20 (1988) 111-157.

[44] C. Pozrikidis, *Boundary integral and singularity methods for linearized viscous flow*. Cambridge University Press, New-York, (1992).

[45] E.M. Toose, B.J. Geurts, J.M.G. Kuerten, A boundary element method for two-dimensional (non)-Newtonian drops in slow viscous flow. *J. Non Newt. Fluid Mech.* , 60 (1995) 129-154.

[46] E.M. Toose, D. van den Ende, B.J. Geurts, J.G.M. Kuerten and P.J. Zandbergen, Axisymmetric non-Newtonian drops treated with a boundary integral method. *J. Engg. math.* 30, (1996), 131-150.

[47] H. Goldstein, *Classical Mechanics*. Addison-Wesley, (1980).

[48] M.R. Kennedy, *A numerical study of three dimensional viscous drops*. Ph. D. Thesis, University of California, San Diego, (1991).

[49] H. van der Klis and E.M. Toose, A boundary integral method for a periodic suspension of viscous drops. *Memorandum No. 1378*, University of Twente, The Netherlands, (1997).

[50] G.K. Batchelor, The stress system in a suspension of force-free particles, *J. Fluid Mech.* , 41 (1970) 545-570.

[51] R.B. Bird, R.C. Amstrong, O. Hassager, *Dynamics of polymeric liquids: Volume 2 kinetic theory*. Wiley-Interscience, New-York, (1987).

[52] H.A. Kramers, Het gedrag van macromoleculen in een stroomende vloeistof. *Physica* 11 (1944) 1-19.

[53] H. Giesekus, Elasto-viskose flüssigkeiten, für die in stationären schichtströmungen sämtliche normalspannungskomponenten verschieden groß sind. *Rheol. Acta* 2 (1962) 50-62.

[54] A. Peterlin, Einfluß der endlichen moleküllänge auf die gradientabhängigkeit des staudinger-index. *Makr. Chem.* 44 (1961) 338-346.

[55] R. Keunings, On the Peterlin approximation for finitely extensible dumbbells. *J. Non Newt. Fluid Mech.* 68 (1997) 85-100.

[56] M.D. Chilcott and J.M. Rallison, Creeping flow of dilute polymer solutions past cylinders and spheres. *J. Non Newt. Fluid Mech.* , 29 (1988) 381-432.

[57] M. Mooney, A theory of large elastic deformation. *J. Appl. Phys.* 11 (1940) 582-592.

[58] J.M. Rallison and E.J. Hinch, Do we understand the physics in the constitutive equation? J. Non Newt. Fluid Mech. , 29 (1988) 37-55.

[59] R. Roscoe, On the rheology of a suspension of viscoelastic spheres in a viscous liquid. *J. Fluid Mech.* 28 (1967) 273-293.

[60] O.A. Ladyzhenskaya, *The mathematical theory of viscous incompressible flow*. Gordon and Breach, New-York, (1969).

[61] R.A. De Bruijn, *Deformation and breakup of drops in simple shear flow*, Ph. D. Thesis, University of Eindhoven, (1989)

[62] M. Manga and H.A. Stone, Buoyancy-driven interactions between two deformable viscous drops, *J. Fluid Mech.*, **256** (1993) 647-683.

[63] J.G.M. Kuerten, *Unpublished notes* (1996)

[64] P.F. Byrd & M.D. Friedman, *Handbook of elliptic integrals for engineers and physicists*. Springer-Verlag, Berlin, (1954).

[65] W.R. Schowalter, *Mechanics of non-Newtonian fluids*, Pergamon Press, Oxford, 1978.

[66] P.W. Patridge, C.A. Brebbia, L.C. Wrobel, *The dual reciprocity boundary element method.* Computational Mechanics Publications, Boston, (1992).

[67] E.M. Toose, B.J. Geurts, J.M.G. Kuerten, A boundary element method for compound non-Newtonian drops. *submitted to Int. J. Num. Meth. Fluids* (1997).

[68] H. Hasimoto, On the periodic fundamental solutions of the Stokes equations and their application to viscous flow past a cubic array of spheres. *J. Fluid Mech.* 5 (1959) 317-28.

[69] G.A.L. van de Vorst, Integral formulation to simulate the viscous sintering of a two-dimensional lattice of periodic unit cells. *J. Engg. math.* , 30 (1996) 97-118.

[70] G. Farin, *Curves and surfaces for computer aided geometric design; a practical guide*, Academic Press, San Diego (1990).

[71] C. DeBoor, *A practical guide to splines*, New-York: Springer-Verlag (1978) 392.

[72] J.C.F. Telles, A self-adaptive co-ordinate transformation for efficient numerical evaluation of general boundary element integrals, *Int. J. Numer. meth. Eng.* 24, (1987), 959-973.

[73] G. Evans, *Practical numerical integration*. Wiley, Guildford, (1993).

[74] J.F. Thompson, Z.U.A. Warsi and W.C. Mastin, *Numerical grid generation : foundations and applications.* North-Holland, New York (1985).

[75] J. Stoér, *Einführung in die numerische mathematick I.* Springer-Verlag, Berlin, 1976.

[76] E.M. Toose, R.M.J. van Damme, H.T.M. van den Ende, B.J. Geurts, J.M.G. Kuerten, A boundary element method for two-dimensional non-Newtonian drops in slow viscous flow. *Memorandum No. 1221*, University of Twente, The Netherlands, (1994).

[77] A. Jameson, Transonic flow calculations. *MAE-report 1651*, Princeton University, (1983).

[78] J.G. Oldroyd, The elastic and viscous properties of emulsions and suspensions. *Proc. Roy. Soc. A* 218 (1953) 122-132.

[79] J.G. Oldroyd, The effects of interfacial stabilizing films on the elastic and viscous properties of emulsions. *Proc. Roy. Soc. A* 232 (1955) 567-577

[80] J.F. Palierne, Linear rheology of viscoelastic emulsions with interfacial tension. *Rheol. Acta* 29 (1990) 204-214; Erratum 30 (1991) 497.

[81] G.B. Jeffery, The motion of ellipsoidal particles immersed in a viscous fluid. *Proc. Roy. Soc. A* 102 (1922) 161-179.

[82] W.J. Milliken and L.G. Leal, Deformation and breakup of viscoelastic drops in planar extensional flows. J. non Newt. HFluid Mech. 40 (1991) 355-379.

[83] L.E. Malvern, *Introduction to the mechanics of a continious medium.* Prentice-Hall, London, (1969).

[84] K.S. Chang and W.L. Olbricht, Experimental studies of the deformation of a synthetic capsule in extensional flow. *J. Fluid Mech.* 250 (1993) 587-608.

[85] Y. Sugiura, A method for analyzing non-Newtonian blood viscosity data in low shear rates. *Biorheology* 25 (1988) 107-112.

[86] D. van den Ende, The hard disk viscosity as a function of the area fraction. *Unpublished notes* (1997)

[87] N.A. Frankel and A. Acrivos, On the viscosity of a concentrated dispersion of solid spheres. *Chem. Engng. Sci.* 22 (1967) 847-853.

[88] H.H. Kausch, D.G. Fesko and N.W. Tschoegl, The random packing of circles in a plane. *J. Colloid Interface Sci.* 37 (1971) 603-611.

Summary

In this thesis we describe the development of a boundary integral method for the simulation of non-Newtonian drops and vesicles subjected to a viscous flow. A vesicle consists of a viscous drop encapsulated by a lipid bilayer and is modelled as a two-layer drop, of which the outer layer is viscoelastic.

As the typical Reynolds number of the flow problem considered is very low, we can describe flow fields inside and outside the drop by the Stokes equations. In order to account for the non-Newtonian character of the fluids in the drop, we incorporate a non-Newtonian stress tensor in the Stokes equations. The time evolution of this stress tensor is describe by a characteristic non-Newtonian model, such as the Oldroyd-B model. By treating the contribution of the non-Newtonian stress tensor to the flow field as a source term, we can derive an integral formulation for the velocity field. However, a disadvantage of this approach is that the source term leads to a domain integral which increases the computational effort substantially compared to Newtonian fluids. The advantage of the method over a more direct (finite difference) discretization of the Stokes equations lies in the fact that only the relatively small non-Newtonian domains of the drop have to be discretized. Other advantages are the flexible and accurate modelling of the boundary shapes including the behavior at infinity and the fact that the incompressibility of the fluids is guaranteed.

Besides the development of a general integral expression for the velocity field, we also considered two specific situations: a single drop in an axisymmetric flow field, and a periodic dispersion of Newtonian drops. In the first case we can transform the integral equation to cylindrical coordinates. By performing the integration over the azimuthal angle analytically we may reduce the dimension of the computational problem. For the second problem it turns out that the periodicity of the problem can be simply included in the Green's functions, whereas the boundary integral formulation remained of the same form as for single non-Newtonian drops.

In this thesis numerical simulations of (non-)Newtonian drops and vesicles subjected to an axisymmetrical flow and of a two-dimensional periodic dispersion of Newtonian drops are described and analyzed. For the actual simulation several numerical techniques are used which are described in detail. The developed methods were tested thoroughly using a numerical and physical validation procedure. This validation showed that most of the numerical methods are at least second order accurate and require only a small amount of points to yield accurate results. From the validation process for a periodic

dispersion of drops it was also found that only a few drops are needed for the generation of reliable macroscopic properties. This result is very promising with respect to the computational costs if one wishes to simulate a dispersion of non-Newtonian drops. The simulation results of non-Newtonian drops indicate that a fluid-like non-Newtonian material mainly influences the deformation process, and to a smaller extent the final shape of the drop. For a solid rubber-like material, however, the final shape of the drop is mainly determined by the elasticity of the material. For vesicles we concentrated on the identification of a characteristic breakup mechanism of the outer layer. From the simulations it appeared that a breakup criterion based on a critical stress in the outer rubber-like layer of the vesicle, is related to the most likely mechanism. Besides in non-Newtonian drops and vesicles, we also found strong non-Newtonian behavior in a dispersion of Newtonian drops. This behavior expresses itself in an effective viscosity which depends on the applied velocity field.

Samenvatting

In dit proefschrift wordt de ontwikkeling van een randintegraalmethode voor de simulatie van niet-Newtonse druppels of vesicles, die onderworpen worden aan een viskeuze kruipstroming, beschreven. Een vesicle bestaat uit een viskeuze druppel die omringd wordt door een lipide dubbellaag en wordt gemodelleerd als een twee-laags druppel waarvan de buitenste laag viscoelastisch is.

Omdat het typische Reynoldsgetal van de door ons beschouwde stroming zeer laag is, kan de stroming in en rondom een druppel adequaat met de Stokesvergelijkingen beschreven worden. Om het niet-Newtonse karakter van de vloeistof in de druppel mee te nemen, introduceerden we een niet-Newtonse spanningstensor in de Stokesvergelijkingen. De tijdsevolutie van deze spanningstensor wordt beschreven door een kenmerkend reologisch model, zoals bijvoorbeeld het Oldroyd-B model. Door de bijdrage van de niet-Newtonse spanningstensor als bronterm te beschouwen, is het mogelijk een integraalvergelijking voor het snelheidsveld op te stellen. Het nadeel van deze aanpak is echter dat de bronterm een domeinintegraal tot gevolg heeft, waarmee de benodigde rekentijd flink toeneemt ten opzichte van Newtonse vloeistoffen. Het voordeel van de methode ten opzichte van andere methoden, zoals eindige differenties, is dat we voor de domeinintegraal alleen een rekenrooster in de relatief kleine niet-Newtonse gebieden van de druppel nodig hebben. Andere voordelen zijn de precieze en gemakkelijke randbehandeling inclusief het gedrag op oneindig en het feit dat de onsamendrukbaarheid van de betrokken vloeistoffen gegarandeerd is.

Naast de ontwikkeling van een algemene integraaluitdrukking voor het snelheidsveld, hebben we ook twee specifieke situaties beschouwd, namelijk een enkele druppel in een axisymmetrische kruipstroming en een periodieke dispersie van Newtonse druppels. In de eerste situatie kunnen we de integraalvergelijkingen transformeren naar cilindercoördinaten, waarna we de dimensie van het probleem met één kunnen reduceren door de integratie over de omwentelingshoek analytisch uit te voeren. De invoering van periodiciteit in het tweede probleem blijkt eenvoudig opgenomen te kunnen worden in de Greense functies. De vorm van de integraalvergelijking blijft daarbij hetzelfde.

In dit proefschrift worden simulaties beschreven en geanalyseerd die verricht zijn voor axisymmetrische Newtonse druppels, niet-Newtonse druppels, vesicles en voor tweedimensionale periodieke dispersies van Newtonse druppels. Voor de eigenlijke simulatie van een niet-Newtonse druppel of vesicle zijn tal van numerieke technieken gebruikt die in detail beschreven worden. De ontwikkelde programmatuur is uitvoerig getest door middel van een nu-

merieke en fysische validatieprocedure. Uit deze procedure bleek dat de meeste methoden minimaal tweede orde nauwkeurig zijn en dat er slechts vrij weinig punten nodig zijn voor nauwkeurige resultaten. Uit het validatieproces bleek tevens dat een beperkt aantal druppels in de periodieke dispersie al betrouwbare macroscopische resultaten genereert. Dit laatste is, speciaal met het oog op de toekomstige simulatie van een dispersie van niet-Newtonse druppels, zeer positief. De simulatieresultaten van niet-Newtonse druppels geven aan dat een niet-Newtons vloeibaar materiaal vooral invloed heeft op het deformatieproces en niet op de uiteindelijke vorm van de druppel. Bij een vast rubberachtig model daarentegen, wordt de uiteindelijke vorm van de druppel vooral bepaald door de mate van elasticiteit van het niet-Newtonse materiaal. Voor vesicles hebben we ons geconcentreerd op de identificatie van een relevant opbreekmechanisme. Uit de simulaties bleek dat een mechanisme gebaseerd is op een kritische spanning in de buitenste rubberachtige laag van het vesicle het meest realistisch is. Naast niet-Newtonse druppels en vesicles blijkt ook een dispersie van Newtonse druppels sterk niet-Newtons gedrag te vertonen. Dit uit zich onder andere in een effectieve viscositeit die afhankelijk is van het opgelegde snelheidsveld.

Dankwoord

Dit proefschrift is het resultaat van vier jaar onderzoek waaraan velen, direct of indirect, hun medewerking hebben verleend. Via deze weg wil ik iedereen die een bijdrage heeft geleverd aan het tot stand komen van dit proefschrift bedanken.

Allereerst wil ik de promotoren J. Mellema en P.J. Zandbergen bedanken voor de gelegenheid die zij mij hebben geboden om dit onderzoek te kunnen doen en hun supervisie daarbij. De directe begeleiding werd gegeven door Bernard Geurts, Hans Kuerten en Dirk van den Ende. Hun begeleiding was niet alleen 'to the point', maar ook enthousiast en vriendschappelijk. Bernard en Hans, ik zal het vrijdagmiddag biljart en het vele blauw niet snel vergeten.

Verder wil ik Hanneke van der Klis bedanken voor het uitstekende afstudeerwerk dat zij heeft geleverd. Haar enthousiasme heb ik als zeer positief ervaren. Ook de hulp van Frans Kuijt en Klaas de Haas heb ik zeer gewaardeerd. Als laatste, maar zeker niet als minste wil ik mijn vriendin Suzanne bedanken voor haar steun gedurende vier jaar van mijn onderzoek. Tenslotte wens ik alle AIO's en OIO's veel succes toe met het vervolg van hun promotie.

Over de Schrijver

De schrijver van dit proefschrift werd op 24 april 1969 geboren te Rotterdam. Hij bezocht vanaf 1981 de Scholengemeenschap Roncalli in Bergen op Zoom en deed eindexamen Atheneum in 1987. Vanaf 1987 tot 1993 studeerde hij technische natuurkunde aan de Universiteit Twente. Het afstudeerwerk werd verricht in de vakgroep Reologie van prof. dr. J. Mellema. Dit theoretische werk is uitgevoerd van april 1993 tot en met oktober 1993. Het onderwerp betrof de uitbreiding van een Rouse keten naar een netwerkachtige struktuur om zodoende het reologisch gedrag van een latex dispersie te kunnen beschrijven. Vanaf november 1993 is hij Assistent in Opleiding bij zowel de leerstoel Reologie van de vakgroep Vloeistoffysica als bij de leerstoel Mathematische Fysica van de vakgroep Toegepaste Analyse. Hij heeft zich bezig gehouden met de ontwikkeling van numerieke methoden voor de simulatie van de vervorming van niet-Newtonse druppels in een kruipstroming. Tijdens zijn aanstelling heeft hij gedeeltes van zijn werk gepresenteerd op internationale conferenties in Engeland, Canada, Frankrijk en Australië.